Computing Adsorption, Diffusion and Separation of Noble Gas Mixtures in MOFs Using Molecular Simulations and Theoretical Correlations

by

Yeliz Gürdal

A Thesis Submitted to the
Graduate School of Engineering
in Partial Fulfillment of the Requirements for
the Degree of

Master of Science
in
Chemical and Biological Engineering

Koc University

July 2013

Koc University

Graduate School of Sciences and Engineering

This is to certify that I have examined this copy of a master's thesis by

Yeliz Gürdal

and have found that it is complete and satisfactory in all respects,
and that any and all revisions required by the final
examining committee have been made.

Committee Members:

_____

Seda Keskin Avcı, Ph. D. (Advisor)

_____

Burak Erman, Ph. D.

_____

Attila Gürsoy, Ph. D.

Date: _____

ABSTRACT

Atomically detailed simulations have been widely used to assess gas storage and gas separation properties of nanoporous materials. Metal organic frameworks (MOFs) are new potential candidates for gas separation applications due to their well defined pore structures, large surface areas and porosities.

In the first part of this thesis, grand canonical Monte Carlo (GCMC) and equilibrium molecular dynamics (EMD) simulations were used to compute adsorption and diffusion of noble gases, Xe, Kr, Ar and their binary mixtures in several MOFs. Ten representative MOFs having different metal sites, organic linkers, topologies and pore sizes were chosen to examine the effects of structural properties of MOFs on their noble gas separation performances. Several properties of MOFs such as adsorption selectivity, working capacity, diffusion selectivity, permeation selectivity, and gas permeability were evaluated and compared with those of traditional nanoporous materials. Results showed that several MOFs exhibit higher selectivities than traditional zeolites in adsorption-based separation of Xe/Kr and Xe/Ar mixtures. According to simulation results, MOFs are promising candidates for Xe/Kr and Xe/Ar separations due to their high Xe selectivity and permeability.

In the second part, Krishna-Paschek (KP) correlations and Ideal Adsorbed Solution Theory (IAST) were applied to predict self-diffusivities and adsorption isotherms of Xe/Kr and Xe/Ar mixtures at various compositions, respectively. These predictions were then compared with the results of molecular simulations obtained in the first part. Gas permeabilities and selectivities of MOFs obtained from theoretical correlations were compared with the ones obtained from simulations and reasons for deviations were discussed. Our results suggested that theoretical correlations can make accurate predictions

and can be used instead of detailed molecular simulations for initial screening of MOFs in noble gas separation applications.

ÖZET

Atomik simülasyonlar nano gözenekli malzemelerin gaz depolama ve ayırma işlemlerindeki performanslarını tahmin etmek için sıkça kullanılmaktadır. Nano gözenekli malzemelerin yeni bir sınıfı olan metal-organik yapılar (MOF); kristal yapıları, geniş yüzey alanları ve geniş gözenekleri ile gaz ayırma işlemlerinde kullanılabilecek malzemelerdir.

Tezin ilk bölümünde, soygazlardan, Xe, Kr ve Ar'nin ve ikili karışımlarının (Xe/Kr ve Xe/Ar) çeşitli MOF'lardaki adsorpsiyon ve difüzyon değerleri sırasıyla grand kanonik Monte Carlo (GCMC) ve denge moleküler dinamik (EMD) simülasyonları kullanılarak hesaplanmıştır. Farklı metallere, organik bağlayıcılara, topolojiye ve gözenek boyutlarına sahip on tane MOF seçilmiş ve bu MOF'ların yapısal özelliklerindeki değişikliklerin soy gaz ayırma performanslarına olan etkileri incelenmiştir. İncelenen MOF'ların adsorpsiyon seçicilikleri, çalışma kapasiteleri, difüzyon seçicilikleri, geçirgenlik seçicilikleri ve geçirgenlikleri gibi çeşitli özellikleri hesaplanmış ve geleneksel nano gözenekli malzemelerin gaz ayırma performanslarıyla karşılaştırılmıştır. Elde edilen verilere göre; Xe/Kr ve Xe/Ar gaz karışımları için çalışılan bir çok MOF, zeolitlere göre daha yüksek adsorpsiyon seçiciliği göstermiştir. Yapılan simülasyonlara göre, yüksek Xe seçicilik ve geçirgenliğe sahip olmalarından dolayı MOF'lar Xe/Kr ve Xe/Ar ayırımı için ümit verici malzemelerdir.

İkinci kısımda, çeşitli kompozisyonlardaki Xe/Kr ve Xe/Ar karışımlarının difüzyon ve adsorpsiyon izotermleri sırasıyla Krishna-Paschek (KP) korelasyonu ve İdeal Adsorpsiyon Teorisi (IAST) kullanılarak tahmin edilmeye çalışılmıştır. Elde edilen tahminler daha sonra birinci kısımdaki moleküler simülasyonlardan elde edilen sonuçlarla karşılaştırılmıştır. Teorik korelasyonlardan elde edilen gaz geçirgenlikleri ve gaz seçicilikleri simülasyon sonuçlarıyla karşılaştırılmış ve sapmaların olası sebepleri tartışılmıştır. Sonuçlarımıza göre teorik korelasyonlar, MOF'ların soy gaz ayırma performansları tahmin etmede ayrıntılı

simülasyonlar yerine kullanılabilir ve bu korelasyonlar kullanılarak doğru tahminler yapılabilir.

ACKNOWLEDGEMENTS

I have completely finished writing this thesis right now, at 4 a.m in the morning of the submission day. There is a guest in my office, a butterfly, but unfortunately she is sleeping. I think I am alone in the whole faculty, cause it have absolute silence. With this peaceful silence, amazement and joy of being completed my master thesis, I think people who are irreplaceable in my life and help me a lot during my master of science period. I learned a lot from them about life and science and I spent very happy days with them. I know this part that I am writing for them surely is not enough to express my feelings, but I will try to do my best.

I am very lucky to study with Assoc. Prof. Dr. Seda Keskin because of her constant support and guidance as an advisor. Her desire for research admires me a lot and I know that without her patient and indulgent nature, this thesis would not be such productive. I want to thank to Prof. Dr. Burak Erman who answered all of my questions in his limited time and accepted to be involved in my dissertation committee. Changing the research field is not hard but interesting and enjoyable for me by the agency of him. I want to thank to Prof. Dr. Ersin Yurtsever who gave me special support through my doctorate programme acceptance term. I am really thankful to him due to his encouragement and appreciation for my academic skills. I am grateful to Prof. Dr. Attila Gürsoy for being my dissertation committee member. I want to express my deep gratitude to Assoc. Dr. Erol Seker who admires me with his skeptical approach to science.

I want to thank to Group NEMO for their sincere friendship, willingness to help me, always smiling faces, desire for research and so on. I am sure that my master could not be more funny and informative than it is right now. Among my group members; my special thanks for İlknur Eruçar especially for her patience, motivation to teach and study and

keeping eye on us like an older sister. Aydın Özcan who always surprised me with his knowledge and discussions deserves great appreciation. He has a brilliant and skeptical mind that allows me to see different aspects of the problems. I want to thank to Tuğba Öztürk because of her original character and surprising personality that shows itself within her every word, in her thoughts, her haircut. Her creative words in daily speech and even the way of joking will be unforgettable for me. I will miss this group.

My childhood friends Zeynep Tekpınar and Ayça Gürler have not still tired of being involved in with me and my disasters. I am thankful to them for their endless and unconditional support. I always feel like in my home when I am with them. I am grateful to Ayşe Dilan Çelebi, for her completely naive personality, for her never giving up friendship. Her humanity and unconditional friendship admire me a lot. I am also thankful to Endam Özkayam who is miles away from me but always deep inside of my heart.

My lovely family Ziya-Şükran-Cengiz-Gülsüm deserves greatest thanks because of always believing in me. I love just 3-years old Kerem Gürdal since his being makes believe miracles and unbearable lightness of thsese miracles. I have been living away from my family for 7 long years, but I have never felt alone. If I had a chance to change my family, I would decisively choose them again.

I want to dedicate this thesis to beloved mathematician Dr. Yılmaz Durğun who is a symbol of freedom, justice, truth and resistance to me. His character and intelligence are beyond my imagination. He has been much more than a friend to me for 6 years. Thank you Yılmaz, for always believing in me. You are not near me right now, but I can imagine the happiness in your eyes when you heard that I completed this thesis.

I gratefully acknowledge the financial support provided by TUBITAK-BIDEB 2228 scholarship program during my master of science.

The sun is raising right now. I hope, these precious people are at least as lucky as I am. Without them it would be very difficult to carry on this research and complete this thesis. I hope, I was able to express my thoughts enough. Now, it is time to sleep…

Yeliz Gürdal

08.07.2013, İstanbul

TABLE OF CONTENTS

LIST OF TABLES

LIST OF FIGURES

NOMENCLATURE

c	concentration
∇c	concentration gradient
d_o	space dimension
D_o	corrected diffusivity
D_{self}	self diffusivity
D	transport diffusivity
$Đ_i$	single component corrected diffusivity of specie i
$Đ_{ii}^{corr}$	self exchange diffusivity of specie i
$Đ_{ij}^{corr}$	binary exchange diffusivity
EMD	equilibrium molecular dynamics
f	fugacity
F	force
GCMC	grand canonical monte carlo
IAST	Ideal Adsorbed Solution Theory
j	molecular flux
J	mass flux
k_B	Boltzmann constant
KP	Krishna-Paschek theoretical correlations
l	membrane thickness
L_{ij}	Onsager's phenomenological coefficient
m	mass of a particle
n	gas uptake

p_i	probability of a system in an i^{th} state
p	momenta of particles
P	permeability
q	molecular partition function
Q	canonical partition function
r	coordination of particles
$\ddot{r}$	second derivative of coordinate
$S_{permeation}$	permeation selectivity
$S_{adsorption}$	adsorption selectivity
$S_{diffusion}$	diffusion selectivity
t	time
T	temperature
U	total potential energy
V	simulation volume
v	velocity
WC	working capacity
y	bulk gas composition
$\langle \ldots \rangle$	ensemble average
δ	time step
σ	entropy production
$\nabla\mu$	chemical potential gradient
Γ	thermodynamic correction factor
ϕ	porosity
Θ	adsorb loading

Θ_{sat}	saturation loading
θ	fractional loading

Chapter 1

INTRODUCTION

Separation is a mass transfer process that converts a mixture of substances into two or more different product mixtures, at least one of which is enriched in one or more of the mixture's constituents [1]. Separation process are carried out based on the differences in chemical properties of species and often classified according to the particular differences used to achieve separation. For example, distillation separates mixtures according to the boiling point differences of species, membrane-based separation is achieved due to the shape, size and chemical affinity differences of species, solubility differences enable separation based on precipitation technique [2].

In the industry, gas mixtures are separated by several processes such as membrane based separation, cryogenic distillation and adsorption [3]. Process intensification which describes the strategy of making dramatic reductions in the physical size of a chemical plant while achieving a given production objective gains importance when choosing the method of gas separation [4]. Considering process intensification leads to reduce the investment and operation costs in an environmentally responsible manner. In this regard, membrane-based gas separation method is recognized as a powerful tool in industry since it is a pressure driven process which is much more efficient and environmentally friendly than the other separation processes [5].

Permeability and selectivity are the two basic parameters that describe the performance a membrane for a gas separation process among other parameters such as durability and

mechanical integrity at the operating conditions [6-7]. Permeability is the rate at which a gas species permeates through the membrane and selectivity is the ability of a membrane to achieve the given separation. Selectivity is described by the relative permeability of the feed species trough the membrane [5]. A promising membrane should exhibit both high permeability and high selectivity, since high permeability decreases the amount of membrane area which leads to lower capital cost of membrane units and higher selectivity results in a higher product purity [8]. Although high permeability and high selectivity are important criteria while choosing membranes, studies have shown that membranes generally undergo a trade-off between gas permeability and selectivity which means more permeable membranes are generally less selective and vice versa [9-10].

There are several materials that can be used to make membranes. Polymer membranes have been used in 90% of the total installed membrane separation units [6]. Glass transition temperature which is the region of transition between glassy and liquid state of polymers, affects the structure of the polymers [11]. An amorphous polymer above its glass transition temperature is called rubbery polymer, which shows relatively large free-volume. The permeability and selectivity of amorphous polymers is higher than the other polymeric membranes, however their separation performance is highly affected by the condensibility of gases [12]. Polymers behave as rigid glass when the operating temperature is below their glass transition temperatures [13] in which case the fractional free-volume decreases and mechanical properties enhance [14-16]. When they are subjected to strong deformations, glassy polymers show tough mechanical response instead of failing abruptly [17-19].

Although polymers are widely used in industry, they can not withstand aggressive chemical environments and high temperatures and due to their low free volume, they show low gas permeability compared to other porous membrane materials. Additionally,

exposure to hydrocarbons or CO_2 at high partial pressure can lead to swelling or plasticization of the polymers [5].

In 1990's, Robeson et al. [18] screened over 300 polymeric membrane is selectivity and permeability for several gas mixtures and showed that there is a trade-off between selectivity and permeability. After few years, Moaddeb et al. [20] showed that molecular sieve inorganic membranes can be better candidates than polymeric membranes since their performances are above Robeson's upper limit for O_2/N_2 separation [9]. Inorganic membranes attracted researchers not only due to their high temperature and wear resistance, well defined stable pore structure and chemically inertness features but also due to their higher permeability and selectivity compared to polymeric membranes [21].

Based on their structure, inorganic membranes are divided into two major groups: porous and dense (non-porous) inorganic membranes. Metals (palladium, silver and their alloys) and solid electrolytes (zirconia) are examples of dense polymers. Primary application areas of these dense polymers include hydrogen and oxygen separation [22]. Oxides (Alumina, Titania, Zirconia), carbon, glass (silica) and zeolites are commercially used as porous inorganic membranes [23]. Silica-based inorganic membranes can be good candidates for separating molecules that have different sizes; however for similar sized molecules like O_2 and N_2, these membranes are insufficient [24]. Zeolites are also good candidates for gas separation because of their size and shape selectivity, chemical durability and stability at high temperatures [25]. However, making a defect free zeolite membrane is challenging [21]. Carbon molecular sieves are used especially for nitrogen separation from air, hydrogen from syn-gas, separation of methane and several light alkenes/alkanes [26]. However, carbon membranes are very brittle and fragile [27] and they show high permeability only for molecules that have kinetic diameters smaller than 4.0-4.5 Å [28]. All the drawbacks of these membranes lead to intensive research to find new promising membrane materials for gas separation.

Research on finding promising membrane materials has increased dramatically [29]. Metal-organic frameworks (MOFs) are a new class of nanoporous materials; they are composed of metals ions connected with organic ligands. They have well defined pore structures, large porosities and surface areas [30]. Several studies pointed out that through the wide choice of metal and organic ligands, a broad range of structural properties that can give better gas separation performance might be rationally designed [31-34].

Metal organic frameworks are highly crystalline materials due to the strong coordination bonds between metal ions and organic linkers. Having organic linkers gives MOFs the advantage of structural flexibility, which distinguishes MOFs from zeolites which do not have synthetic flexibility [35]. MOFs have extremely high surface areas (500-6000 m^2/g) [36] which increase van der Waals interactions with gases, high porosities, thermal and mechanical stabilities and low densities (0.2-1 g/cm^3) which make them potential candidates for gas storage and gas separation processes [37]. Figure 1.1 shows the structure of one the most widely studied MOFs, CUBTC (HKUST-1).

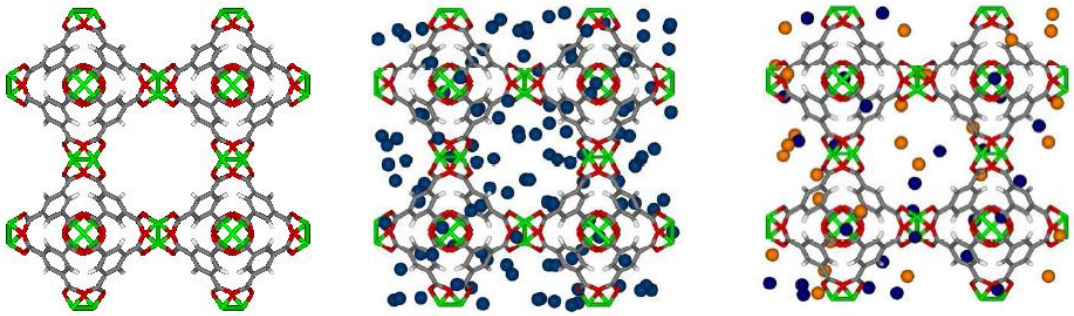

Figure 1.1: Unit cell representation of CuBTC. The atoms in CuBTC structure are copper (green), oxygen (red), carbon (grey) and hydrogen (white). From left to right: Empty CuBTC, CH_4 molecules (blue spheres) in the CuBTC pores, CH_4 and H_2 (orange spheres) molecules in CuBTC pores [37].

Metal organic frameworks have been widely used for adsorption of CO_2, CH_4, H_2 and N_2 in addition to separation of several gas mixtures including CO_2/CH_4, CH_4/H_2, CO_2/N_2 and CO_2/H_2 [38-40]. Very little experimental and computational study exists in the literature for separation of noble gas mixtures. To fill this gap in the literature, atomically detailed simulations were used to examine performances of several MOFs for noble gas separations in this thesis.

There are a large number of application areas for noble gases. For example Argon (Ar) and Krypton (Kr) are used in electric light bulbs and fluorescent lamps. Indeed, Kr is better candidate for light bulbs than Ar, because the denser the gas, the greater the slowing effect on the rate of evaporation of the metallic filament, which increases efficiency [41]. However, since separation of Kr from air is energy intensive, Ar is also used in lasers and emits discrete frequencies of light in the visible and ultraviolet regions of the spectrum [42].

Krypton is the most common noble gas used in excimer lasers [42]. It can be used to test for leaks in sealed containers [41]. If even small quantities of Kr get through the walls of such a container, leaks can be detected through the radiation it gives off; the presence of a leak is then known. Xenon (Xe) is about twice as expensive as Kr for traditional separations. In general, elements absorb X-rays with increasing efficiency as the atomic number increases. Consequently, Xe, with an atomic number of 54, is quite efficient as an X-ray absorber. Among the noble gases, the greater the atomic number, the more soluble the gas in water and in body fluids. Generally substances that dissolve in body fluids often display anesthetic effects. Since Xe is the most soluble, it is the most efficient anesthetic [41]. Xe-filled arc lamps are particularly intense and are used to project motion pictures. Liquid Xe can be also used in bubble chambers to study the production and properties of subatomic particles. Xe gas is used in neutron counters, ionization chambers for cosmic rays [42].

Another use for noble gases is thermal insulation. Ar is generally used for this purpose because of its low thermal conductivity. Thermal conductivity depends directly on the specific heat capacity of the gas and inversely related with the mass and size of the atoms or molecules. If a molecule has low specific heat capacity and large mass and diameter, then its thermal conductivity will be low. Noble gases are good candidates as thermal insulators. The reason is that molecules, with their vibrational and rotational states, are able to absorb energy in more ways than atoms, therefore monatomic gases (noble gases) have a lower specific heat capacity than molecular gases [41].

All of these applications require economical and practical separation methods for noble gases. For example, after cryogenic distillation of air, a mixture of 80% Kr and 20% Xe is obtained and this has to be purified further with low cost [43]. Instead of energy intensive cryogenic distillation, Xe/Ar and Xe/Kr mixtures can be separated by using promising adsorbents and/or membranes. Metal organic frameworks (MOFs), as a new class of nanoporous materials, should be examined for separation of Xe, Kr and Ar which would be a valuable input to the literature.

In this thesis, adsorption-based and diffusion-based separation of Xe/Ar and Xe/Kr mixtures were examined by using Grand Canonical Monte Carlo (GCMC) and Equilibrium Molecular Dynamics (EMD) simulations. Theoretical predictions were validated by comparing the results with the experimental data. After validations, permeability, permeation selectivity, adsorption selectivity and working capacity of several MOFs were calculated by approximate methods and the most promising MOFs for noble gas separation were identified. Effects of pore size and shape, free volume, loading, composition of the adsorbate on adsorption and diffusion of noble gases in MOFs were also discussed. Ideal Adsorbed Solution Theory (IAST) [44] and Krishna-Paschek (KP) correlations [45], were used to predict adsorption and diffusion of gas mixtures in MOFs and predictions of these theories were compared with the results of the full atomic simulations. The differences

between theoretical predictions and computationally demanding simulations were discussed.

Chapter 2 reviews the literature for the experimental and computational studies on noble gas separation by metal organic frameworks (MOFs). Theoretical background of statistical mechanics, GCMC and EMD simulations was briefly explained in Chapter 3. Computational and theoretical methods used to predict noble gas separation performances of MOFs were presented in Chapter 4. The results of were discussed in Chapter 5 and conclusions were presented in Chapter 6.

Chapter 2

LITERATURE REVIEW

This chapter reviews experimental and computational studies on gas separation with nanoporous materials, basically metal organic frameworks (MOFs). Although, high number of studies in the literature has focused on CO_2, H_2, N_2 and CH_4 separation, only a few studies addressed separation of noble gas mixtures using nanoporous materials [46-48]. Since noble gases play a significant role in industry, examining noble gas separation performance of MOFs is worthwhile.

2.1. Studies on Gas Separation with MOFs

This section reviews the recently published studies on gas separation with MOFs. Gas separation with other porous adsorbents and membranes like zeolites can be found elsewhere [49-52].

Theodorou et al. [53] compared three different simulation techniques, equilibrium molecular dynamics (EMD), non-equilibrium molecular dynamics (NEMD) and Darken model to examine CH_4 diffusion in silicate zeolites. This study showed that CH_4 diffusivity decreases with loading in all simulations, however diffusivities obtained by EMD are lower than the ones obtained from NEMD and Darken model because of the non-linear effects caused by large concentration gradients. They concluded that EMD gives similar results with the other two methods only if the system is in the linear response regime.

Düren et al. [54] studied surface area, free volume, strength of the energetic interaction and pore size distribution effects on CH_4 adsorption by computational screening of several nanoporous materials including MOFs, zeolites and carbon nanotubes. They concluded that materials that have large surface area, high free volume, low framework density and strong CH_4-adsorbent interactions can be promising candidates for CH_4 storage. Snurr et al. [55] modeled CH_4 adsorption in several isoretical MOFs (IRMOF-1, -8, -10, -14, -16) and investigated the effects of the length of organic linkers on adsorption capacity. According to their study, as the length of the organic linker increases, pore size and pore volume of the IRMOFs increases which leads to increasing CH_4 adsorption for the pressures up to 40 bar. Jung et al. [56] studied GCMC simulation of H_2 adsorption in catenated MOFs, where two separate frameworks self assemble within each other, to see the effects of catenation on adsorption capacity. Their results showed that H_2 adsorption capacity of catenated IRMOFs is higher than the one for noncatenated ones since small pores generated by catenated IRMOFs confine H_2 more densely than the larger pores created by noncatenated IRMOFs. Han et al. [57] studied H_2 adsorption in MOFs and zeolite imidazolate frameworks (ZIFs), which are a subclass of MOFs, at 300 K and 77 K, pressures up to 100 bar. They investigated the effects of functional groups on H_2 storage. Their study showed that at 77 K and low pressures, since H_2 binding energy increases, including functional group in ZIFs enhances H_2 adsorption. At higher pressures, H_2 adsorption decreases as a result of decreasing surface area. They have concluded that for high H_2 adsorption, ZIFs should have both high surface area and small pore apertures similar to H_2 kinetic diameter.

Krishna et al. [58] investigated the performance of MgMOF-74 for separating CO_2/H_2, CO_2/CH_4 and CH_4/H_2 mixtures using Configurational-Biased Monte Carlo (CBMC) simulations. According to their results, as gas specie concentration within the pores increases, correlations effects between molecules also increase which lead to increase in separation performance of MgMOF-74. They also compared their simulation results of CO_2

isotherms at 300 K and 313 K with experimental studies and deviations from experimental results below 0.1 MPa were attributed to the force field used in simulations which does not account for orbital interactions and polarization.

van Baten et al. [59] screened several MOFs and ZIFs for separating variety of mixtures such as CO_2/CH_4, CH_4/H_2, CO_2/N_2, CO_2/H_2, alkanes/alkenes and hydrocarbons. MgMOF-74 membranes were found to be promising for CO_2/H_2 and CO_2/N_2 separation, ZnMOF-74 membranes were found to be promising for CH_4/H_2 separation and Co(BDP) membranes were promising candidates for separation of hexane isomers among the considered MOFs. In their another study [60], they showed that for CO_2/H_2 separation ZIF-8 shows promising separation performance over many zeolites due to its narrow windows. Yang and co-workers [61] investigated separation of CO_2 from flue gases (mixtures of $CO_2/N_2/O_2$) using CuBTC. Their results showed that not only the bulk pressure but also temperature and gas composition are important factors that affect separation performance of CuBTC. Guo et al. [62] used molecular simulations for adsorption and separation of CH_4/H_2 mixtures in ZIFs. Their study showed that due to higher isosteric heat of adsorption of CH_4, both mixture and single component CH_4 adsorption isotherms are always stronger than H_2 adsorption isotherms in all MOFs.

Jiang et al. [63] chose several MOFs that have different topologies, pore sizes and chemical characteristics and studied the influence of framework charges on CO_2 uptake. According to their research, at low pressures, framework charge contribution to CO_2 uptake can not be ignored however at moderate pressures this contribution can be neglected. Babarao et al. [64] studied adsorption and separation of CO_2/CH_4 mixture in several MOFs with different characteristics such as exposed metals, catenation and extra framework ions. They showed that the selectivity of CO_2 over CH_4 in MOFs is enhanced slightly by catenation, exposed metals and significantly by extra framework ions. Babarao and Jiang [65] studied separation of CO_2/H_2, CO_2/CH_4, and CO_2/N_2 in *rho* zeolite-like metal organic

frameworks (*rho*-ZMOF) which contains a wide-open anionic framework and charge-balancing extraframework Na^+ ions. They concluded that *rho*-ZMOF exhibits high adsorption for CO_2 over other species. This is attributed to the highly charged framework and the large density of extraframework Na^+ ions which exert strong electrostatic interactions on the quadrapolar CO_2 molecules.

Atci et al. [66] studied CH_4/H_2, CO_2/CH_4, and CO_2/H_2 mixture separation in bio-metal organic framework (bio-MOF). They showed that Bio-MOF-11 exhibits significantly higher adsorption selectivity for CO_2 over CH_4 and H_2. In their another study [67]; atomic models for single component CH_4, CO_2, H_2, and N_2 and mixture H_2/CO_2, H_2/N_2, H_2/CH_4 gases in several ZIFs and ZIF/polymer composite membranes were examined. They got good agreement between their theoretical predictions and experimental measurements. Keskin [68] studied the separation performance of isostructural MOFs having different metal sites, CPO-27-M (M= Ni, Co), for separation of CH_4/H_2 mixtures. Results showed that CPO materials exhibit higher adsorption selectivity and membrane selectivity than IRMOFs. Keskin [69] also studied CH_4/H_2, CO_2/CH_4, and CO_2/H_2 separation in several ZIFs. Results showed that ZIF-3 and ZIF-10 exhibit significantly higher adsorption and permeation selectivities for separation of all gas mixtures as compared to widely studied MOF membranes. Further studies on gas separations using MOFs by molecular simulations can found elsewhere [70-73].

2.2. Noble Gas Separation Using MOFs

Computational studies on noble gas separation are limited in the literature. Ryan et al. [74] investigated adsorption of Xe/Kr mixtures in IRMOF-1, HKUST-1, UMCM-1, ZIF-8, MOF-505, NOTT-101, NOTT-108, Pd-MOF and concluded that large pore materials are not desirable for efficient adsorption-based separation of Xe/Kr. Greathouse et al. [75]

reported adsorption isotherms of Xe/Ar and Xe/Kr mixtures in IRMOF-1 using GCMC, computed the adsorption selectivity of IRMOF-1 and concluded that IRMOF-1 is a good adsorbent for Xe separation. Skoulidas et al. [76] used GCMC simulations to report adsorption of Ar in MOF-2, MOF-3, MOF-5, CuBTC and performed MD simulations to compute the self-diffusivity (corrected diffusivity) of Ar in MOF-2, MOF-3, MOF-5, CuBTC (MOF-5) at room temperature. Van Heest and coworkers [77] screened a large number of MOFs for Ar/Kr, Kr/Xe, Xe/Rn separations using molecular simulations. They chose 70 materials for further analysis and showed that GUPJEG01 (Mn(dcbp)) is the most promising MOF for Kr/Xe separations due to its extremely high adsorption selectivity. They also showed that the Ideal Adsorbed Solution Theory (IAST) shows good agreement with the GCMC simulations except for materials in which pore blocking effects are important. Sikora et al. [78] recently generated 137,000 hypothetical MOFs and screened them for adsorption-based separation of Xe/Kr mixtures using GCMC simulations at 273 K. They concluded that MOFs having pores just large enough to fit a single Xe atom and those having morphologies resembling tubes of uniform width are ideal for Xe/Kr separation.

Similar to the simulation studies, the number of experimental studies for noble gas separation is also limited. Mueller et al. [79] measured Xe, Kr and Ar uptake of IRMOF-1. Liu et al. [80] measured adsorption of pure Xe, pure Kr, Xe/Kr mixture and $O_2/N_2/Ar/CO_2/Xe/Kr$ mixture in CuBTC (also known as HKUST-1), Ni/DOBDC (also known as CPO-Ni) and activated carbon. They showed that Ni/DOBDC exhibits higher selectivity for pure Xe compared to pure Kr and it is Xe selective in adsorption-based Xe/Kr separations. For a low concentration of Xe and Kr in air, Xe has the longest effluent time over Kr, CO_2, N_2 and O_2. This study showed that MOFs can be promising candidates for separation of Xe from air, however Xe concentration in air is much lower than Kr concentration in reality and this was not the case of their experimental set-up. Thallapally

et al. [81] measured Xe adsorption capacity of Ni/DOBDC, IRMOF-1 and activated carbon. Their results showed that Ni/DOBDC has a higher Xe adsorption capacity compared to IRMOF-1 and activated carbon. Dorcheh et al. [82] investigated single component Xe, Kr adsorption and desorption in HKUST-1, MFU-4l, COF-102 and ZIF-8 and concluded that MFU-4l can be a good candidate for noble gas separation. Fernandez et al. [83] investigated Xe and Kr adsorption in FMOFCu and FMOFZn and observed an inversion in adsorption selectivity toward Kr on FMOFCu at temperatures below 0^{o}C. This result was attributed to the decreasing pore flexibility of FMOFCu below 0^{o}C which prevents Xe diffusion inside the channels.

There are a few studies on diffusion behaviors of noble gases. June et al. [84] studied calculating Xe self diffusivity by EMD in silicate at 200 K, 300 K and 400 K and various loadings. Skoulidas et al. [85] studied Ar self diffusivity in MOF-5, MOF-2, MOF-3, Cu-BTC and silicate and corrected diffusivity in MOF-5 at room temperature by using EMD simulations. Jost et al. [86] studied Xe self diffusivity in silicate using both experiments and EMD simulation.

Two studies examined the polarizability effects on adsorption of noble gases. Do et al. [87] investigated the intermolecular interactions between two fluid molecules in the presence of a solid surface. They stated that the greater the polarizability between framework-adsorbate atoms, the greater the reduction in the intermolecular molecular energy calculated if adsorbate atoms were in the bulk. Therefore they proposed a new model for calculating two fluid molecules interaction close to surface atoms and tested this approach with noble gases such as Ne, Ar, and Xe. The polarizability of Ne, Ar, and Xe are found as 0.395, 1.64, and 4.04×10^{-24} cm^3, respectively which means Xe should have the greatest reduction among these three adsorbates. According to their results, Ar adsorption isotherms obtained by modified potential GCMC simulations match perfectly with the experimental data, whereas overestimation is obtained with classical 12-6 LJ potential

simulations. This also holds for Xe and Ne, where modified potential captures the experimental data. Meek et al. [88] also studied polarizability effects on the adsorption of noble gases by both experimental studies and GCMC simulations. They changed one hydrogen linker of IRMOF-2 with –F, –Cl, –Br and –I halogens showed that increasing linker polarizability results in increasing gas uptake. This was also observed for Kr/N_2, Xe/N_2, and Xe/Kr selectivity and isosteric heats of adsorption.

These recent studies showed that MOFs can be used as promising adsorbents for noble gas separation, alternative to energetically intensive cryogenic distillation of air. For that reason, noble gas adsorption behaviors and diffusion characteristics of morphologically different MOFs should be investigated. In this thesis, gas adsorption and diffusion of noble gases in various MOFs structures were examined. The separation performances of MOFs were evaluated and the effect of pore structures on the separation performance was discussed.

Chapter 3

THEORY

In this thesis, adsorption of noble gases in MOFs and their corresponding diffusivities were modeled using grand canonical monte carlo (GCMC) and equilibrium molecular dynamics (EMD) simulations, respectively. This chapter gives brief information on theoretical background of statistical mechanics, GCMC and EMD simulations. Mass fluxes in nanoporus materials, types of diffusivities, Onsager's linear response theory and parameters that are used in promising membrane selection are also briefly explained in this chapter.

3.1. Grand Canonical Monte Carlo (GCMC) Simulations for Adsorption

The properties of a system can be described at two levels: macroscopic in which case thermodynamic properties, i.e. pressure, volume, enthalpy, Gibb's free energy or Helmholtz's free energy are considered and microscopic level which specifies the states of each molecules. Statistical mechanics, a bridge between macroscopic and microscopic levels, describes macroscopic thermodynamic properties in terms of microscopic atomic and molecular properties. In microscopic description, classical or quantum mechanics can be used, however in a macroscopic assembly of atoms each energy eigenstate of a single atom splits into more than 10^{23} eigenstates of the energy and one needs to update them every 10^{-15} seconds or so. The solution of this impractical situation is statistical mechanics

which explains macroscopic mechanics in statistical terms, i.e. in terms of average or most probable results. Using Boltzmann distribution, the probability of a system in an i^{th} state with energy ε_i at temperature T is shown below:

$$p_i = \frac{e^{-\varepsilon_i / k_B T}}{\sum_{i=1}^{N} e^{-\varepsilon_i / k_B T}} \tag{3.1}$$

The probability of a whole system or assembly of molecules, in a particular system state i, with energy E_i is given as follows:

$$p_i = \frac{e^{-E_i / k_B T}}{\sum_{i=1}^{N} e^{-E_i / k_B T}} \tag{3.2}$$

In Equation 3.1 and Equation 3.2, $\sum_{i=1}^{N} e^{-\varepsilon_i / k_B T}$ and $\sum_{i=1}^{N} e^{-E_i / k_B T}$ are the molecular partition function (q) and canonical partition function (Q), respectively. They measure how probabilities are partitioned among different available energy levels. Also, canonical partition function can be written as integration over molecular position and momenta;

$$Q = \int dp^N dr^N e^{-E\left(p^N, r^N\right) / k_B T} \tag{3.3}$$

where r^N stands for coordination of all N particles and p^N is the corresponding momenta.

If we consider any function A, $\langle A \rangle$ which describes how the instantaneous A values are distributed about their average can be computed by summing over all values of A, with each weighted by its probability of occurrence as shown below:

$$\langle A \rangle = \int A.p(A).dA \tag{3.4}$$

which is also equivalent to

$$\langle A \rangle = \frac{\int dp^N dr^N A\left(p^N, r^N\right) e^{-E\left(p^N, r^N\right)/k_B T}}{\int dp^N dr^N e^{-E\left(p^N, r^N\right)/k_B T}} \tag{3.5}$$

Computation of average of function A is very difficult using Equation 3.5. One simple numerical method for finding averages is Monte Carlo importance sampling algorithm introduced by Metropolis et al. [89] The principle idea of importing sampling is to use Monte Carlo procedure to generate random walk in the phase space that have important contribution to the ensemble averages [90]. The details of Monte Carlo procedure can be found elsewhere [91].

Monte Carlo procedure can be applied to several ensembles including canonical (constant temperature, volume and number of particles), microcanonical (constant energy, volume and number of particles), isobaric-isothermal ensemble (constant temperature, pressure and number of molecules) and grand canonical ensemble (constant chemical potential, volume and temperature).

Adsorption is an equilibrium process. In an experiment, adsorbed gas will be in equilibrium with the bulk gas in the reservoir which means that chemical potential and

temperature of the gas inside and outside of the reservoir should be equal. For mimicking adsorption experiment, using grand canonical ensemble is the most appropriate since it is desired to determine average number of particles in a system as a function of external conditions (such as temperature and pressure). Also, keeping number of particles constant in other ensembles leads to use of grand canonical ensemble for adsorption process. By GCMC simulations, temperature and chemical potential are imposed and the number of particles is allowed to fluctuate during the simulation. Particle fluctuation can be done with random movements in the simulation which are particle addition, deletion and displacement. These movements are rejected or accepted according to Boltzmann-type weighting. By GCMC, equilibrium concentration of the adsorbed molecules can be determined by knowing temperature and chemical potential gradient and adsorption isotherms can be predicted by changing the pressure. The statistical basis of GCMC simulations, progress and outlook in Monte Carlo simulations can be found elsewhere [90, 92].

3.2. Molecular Dynamics for Determining Diffusion Coefficients

Molecular dynamics (MD) is a simulation technique used for computing equilibrium and transport properties of a classical many-body system in time in the absence of any thermodynamic driving forces that can lead to fluxes within the system. In molecular dynamics a system consisting of N particles is chosen and initial positions and velocities are assigned (initialization). Forces on each particle are computed. Then Newton's equation of motion for this system is integrated until the properties of the system no longer change with time (equilibration). After equilibration actual measurements are performed and this step is called production. Here ergodicity plays key role which is the case when ensemble average is equal to the time average of any function A as [93] shown below:

$$\langle A \rangle = \frac{\int dp^N dr^N A(p^N, r^N) e^{-E(p^N, r^N)/k_B T}}{\int dp^N dr^N e^{-E(p^N, r^N)/k_B T}} = \lim_{t \to \infty} \frac{1}{t} \int_{t_o}^{t_o + t} A(\tau) d\tau \qquad (3.6)$$

By ergodicity assumption, ensemble averaged structural and thermodynamic properties from an equilibrated MD simulation can be calculated. While determining forces on each particle, following potential energy formula should be used:

$$U = \sum_i^N u_1(r_i) + \sum_i^N \sum_{j>i}^N u_2(r_i, r_j) + \sum_i^N \sum_{j>i}^N \sum_{k>j>i}^N u_3(r_i, r_j, r_k) + \ldots \qquad (3.7)$$

where $\sum_i^N \sum_{j>i}^N$ notation indicates a summation over all distinct pairs i and j without counting any pair twice. The first term in Equation 3.7 represents the effects of external field (i.e. container walls) on the system. In addition to the second term which represents the pair potential, other terms in Equation 3.7 accounts higher order particle interactions. A common approximation in MD is that potential energy of the whole system can be written as just pairwise additive sum of the potentials between individual atoms [94].

Periodic boundary conditions [91] are generally applied in MD simulations not to consider potentials caused by external effects. To form an infinite system, the central simulation box is replicated throughout the space. When a molecule leaves the central box through a face, one of its images enters through the opposite face. Short range interactions such as dispersive and repulsive effects are truncated and Ewald sum can be used to handle long range electrostatic interactions [93]. The atoms of solid medium can be either treated as flexible or rigid. Rigid nanoporous material assumption save computational time since it allows the interaction between a particular type of sorbate atom to be evaluated once and

tabulated before the simulation on a fine grid over the nanoporous material unit cell [84]. As simulation continues, potentials can be determined rapidly by interpolating from the tabulation [94].

Newton's equation of motion which should be solved is given below

$$m_i \ddot{r}_i = F_i \tag{3.8}$$

where m, r_i and F_i are the mass, coordinate vector, and total force acting on particle i, respectively. To integrate Equation 3.8, initial positions and velocities should be fully defined. Once initial positions and velocities were determined at time t, positions and velocities can be obtained at the later time $t + \delta t$ .The time step (δt) should be small enough in order to get accurate integration and conserve total energy of the system. Several algorithms can be used for integration such as Gear predictor-corrector algorithm or Verlet algorithm. In this thesis, Verlet algorithm which is obtained by adding two Taylor expansions is used as shown below

$$r(t+\delta t) = 2r(t) - r(t-\delta t) + \delta t^2 \ddot{r}(t) + \mathrm{O}(\delta t^4) \tag{3.9}$$

Although velocities are not explicitly present in Equation 3.9, following formula can be used for estimating kinetic energies.

$$v(t) = \frac{r(t+\delta t) - r(t-\delta t)}{2\delta t} + \mathrm{O}(\delta t^2) \tag{3.10}$$

As in the case of GCMC simulations, several ensembles such as canonical (constant temperature, volume and number of particles) and microcanonical (constant energy, volume and number of particles) can be applied to MD simulations. In this thesis canonical ensemble is used in EMD simulations to determine diffusion coefficients. Although diffusion is a non-equilibrium process, we used EMD to define diffusivities. We basically assumed that we are studying linear response region which is described in section 3.3. Tepper et al. [95] calculated corrected diffusivities (see section 3.3.) using both equilibrium molecular dynamics and nonequilibrium molecular dynamics (NEMD) with wave vector dependent Einstein expression. Figure 3.1 shows the resultant diffusivities.

According to Figure 3.1, corrected diffusivity values of Argon in $AlPO_4$-5 calculated using NEMD and EMD are perfectly agree with each other at large simulation box lengths, whereas as box length decreases deviation between NEMD and EMD becomes significant. This proves that, for calculating a nonequilibrium property, EMD can be accurately used if a large simulation box length is set.

Further information on details of using EMD simulations to obtain diffusion coefficients can be found in previous studies of zeolites, carbon nanotubes and MOFs [96-99].

3.3. Mass Fluxes in Nanoporous Medium

As it was mentioned in section 3.2, molecular dynamics is a simulation method which can be used for determining diffusion coefficients that characterize the rate of translational progress of adsorbed species in a porous medium. Studying transport in nanopores is important, since it is generally the rate limiting step in industrial applications like membrane processes or catalytic applications. In this part, we briefly review nonequilibrium thermodynamics used in transport phenomena for relating fluxes and

driving forces of diffusion, discuss statistical mechanical view of linear response theory and how it can be used in molecular simulations, introduce different types of diffusivities and explain relationships between these diffusivities.

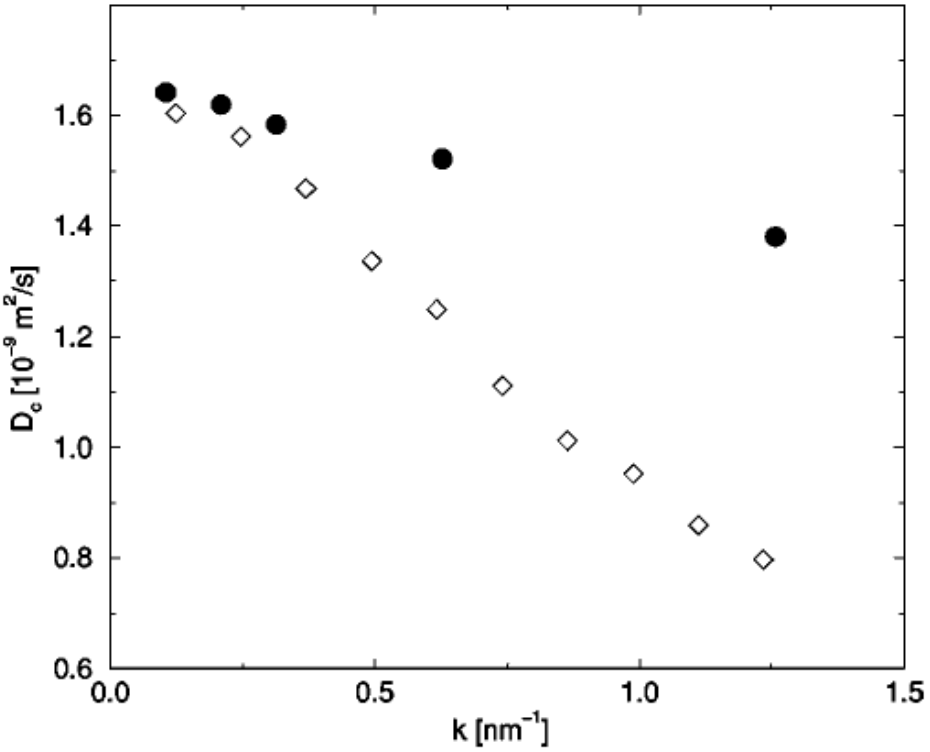

Figure 3.1: Corrected diffusivity of Argon in $AlPO_4$-5 vs. wave vector. Diffusivities with open symbols and closed symbols were calculated using NEMD and EMD, respectively. Wave vector is equal to $k = 2\pi/L_z$, where L_z is simulation box length [95].

All membrane permeation and separation processes are nonequilibrium processes, so the transport equation describing permeation through a membrane must satisfy nonequilibrium thermodynamics [100]. Onsager [101-102] originally proposed the

principles of nonequilibrium thermodynamics and stated that the rate of work loss associated to entropy production due to irreversible processes is the scalar product of steady state fluxes J_i and generalized forces X_i as shown below;

$$T\sigma = \sum_{i}^{N} J_i X_i \tag{3.11}$$

where σ is entropy production per unit area and T is the ambient temperature. According to principles of nonequilibrium thermodynamics, fluxes are linearly related to forces as

$$J_i = \sum_{k}^{N} L_{ik} X_k \tag{3.12}$$

where L_{ik} is the phenomenological coefficient. Equation 3.12 indicates that any flux can be caused by both its own conjugate force and any other driving forces. The phenomenological coefficients satisfy the Onsager's reciprocal relation:

$$L_{ik} = L_{ki} \tag{3.13}$$

These last three equations summarize the principles of linear nonequilibrium thermodynamics for irreversible processes such as membrane permeation. The driving force that causes mass transfer must be determined and nonequilibrium thermodynamics must be interpreted in a more practical way.

Consider a system consisting of a nanoporous solid Z, and the fluid species 1,2,..,N adsorbed within the solid, under isothermal conditions at temperature T. Any flux in the nature arises in response to inhomogeneties in the system or imposition of external force

fields, F_i (N/molecule), on each species i. In the mass transfer case, the driving force is chemical potential gradient, $\Delta\mu_i$ ($J.m^{-1}.molecules^{-1}$) [103]. To be safely in local thermodynamic equilibrium, we assume that these gradients of chemical potential or external forces are small. By this assumption, we guarantee that within the system, volume elements are small relative to macroscopic dimensions, however large enough relative to molecular dimensions [104]. Mass fluxes occurring in these volume elements over timescales considerably longer than the characteristic times of molecular level relaxation process in the system are described. Regarding to nanoporous medium, it should also be assumed that the relaxation process is homogeneous down to molecular length scales and translationally invariant in all three directions of space which eliminates considering random media where sorbate molecules are confined to move within finite, nonpercolating clusters or sites [105]. These approaches are valid for intracrystalline transport in most nanoporous materials, with the exception of porous materials that have small pores relative to sorbate molecules which are forced to single file diffusion [106-107].

Under the assumption of mechanical equilibrium in each volume element and employing a fixed frame of reference, Gibbs-Duhem equation [108] within the considered volume element leads to:

$$\sum_{i=1}^{N} N_i(\nabla\mu_i - F_i) + N_Z(\nabla\mu_z - F_z) = 0 \qquad (3.14)$$

By substituting $c_i = N_i / V$ which is molecular concentration of specie i, it gives the following expression for macroscopic flux J_i (molecules m^{-2} s^{-1}) of each species, according to nonequilibrium thermodynamics:

$$J_i = -\sum_{j=1}^{N}\left(L_{ij} - \frac{c_i}{c_Z}L_{iZ}\right)\left(\nabla\mu_j - F_j\right) \quad \text{(i=1,2,..,N)} \tag{3.15}$$

where the index i can take the values 1,2,…,N and Z. As it was mentioned before the phenomenological coefficients L_{ij}, (molecules^2.J^{-1}.m^{-1}.s^{-1}), obey Onsager's reciprocity relations. Also the microscopic (molecular) flux (j_i) of component i, that is, the mechanical quantity can be written as [109],

$$j_i = -\sum_{l=1}^{N} v_{il} \tag{3.16}$$

where v_{il} is the center-of-mass-velocity vector, *l* is a molecule of specie i which is running over all atoms of the medium and N is the total number of molecules of species i at a given time within an element of volume V of the system. Assuming medium Z as perfectly stationary is usually satisfactory, which means that $v_{zl} = 0$ for every *l* = 1,2,..,$N_{z.}$. By this assumption $L_{iz} = 0$ in Equation 3.15 for every i=1,2,..,N and the equation simplifies to:

$$J_i = -\sum_{j=1}^{N} L_{ij}\left(\nabla\mu_j - F_j\right) \quad \text{(i = 1,2,..,N)} \tag{3.17}$$

By perfectly stationary solid porous material approximation, no explicit consideration of the solid component Z is required. Additionally, in the absence of external forces:

$$J_i = -\sum_{j=1}^{N} L_{ij}\nabla\mu_j \quad \text{(i = 1,2,..,N)} \tag{3.18}$$

However, the use of Equation 3.18 is impractical, since chemical potentials can not be measured in the laboratory. Here the key is to express chemical potentials in terms of more convenient variables, especially experimentally observable ones, for the membrane transport processes. The first attempt of estimation of transport coefficients using molecular dynamics relies on Onsager's linear response theory which provides the bridge between equilibrium time correlation functions and nonequilibrium response to weak perturbations [110]. According to Onsager's regression hypothesis, the relaxation of weak nonequilibrium disturbances follows the same laws as the regression of the spontaneous fluctuations at equilibrium [111]. This means that using linear response theory one can arrive a molecular interpretation for the coefficients L_{ij} as applied to transport processes which are experimentally observable quantities [110]. Linear response theory dictates,

$$L_{ij} = \frac{1}{d_o V k_B T} \int_0^\infty \langle j_i(0).j_j(t) \rangle dt \qquad (3.19)$$

where i,j = 1,2,…,N,Z. The angular brackets, $\langle ... \rangle$, denote ensemble averages in an equilibrium system that finds itself at the same thermodynamic properties as the considered volume element of the non-equilibrium system at the considered time. V is the simulation volume, $j_i(0).j_j(t)$ is the flux cross correlation function and d_o is the space dimension. Equation 3.19 is the Green-Kubo form [111] which relates phenomenological transport coefficients to time integral of a correlation function. It states that the rate at which the volume element will respond to any gradient or external force field that causes it to depart from thermodynamic equilibrium can be estimated from the rate at which spontaneous fluctuations occurring within the same volume element in a state of equilibrium die out with time [94]. As it was mentioned before, gradient or external force should be small for

this relation to be valid between equilibrium fluctuations and nonequilibrium response. The molecular flux cross-correlation function $\langle j_i(0).j_j(t)\rangle$, can be analyzed as follows:

$$\langle j_i(0).j_j(t)\rangle = \sum_{l=1}^{N_i}\sum_{l^*=1}^{N_j}\langle v_{il}(0).v_{jl^*}(t)\rangle \quad \text{(for i} \neq \text{j)} \tag{3.20}$$

$$\langle j_i(0).j_i(t)\rangle = \sum_{l=1}^{N_i}\langle v_{il}(0).v_{il}(t)\rangle + \sum_{l=1}^{N_i}\sum_{\substack{l^*=1 \\ l^*\neq l}}^{N_i}\langle v_{il}(0).v_{il^*}(t)\rangle \quad \text{(for i=j)} \tag{3.21}$$

The velocity correlation and autocorrelation functions are expected to be nonzero only over a finite time t which is also known as molecular relaxation time. Equation 3.20 can also be written in terms equivalent Einstein form [110] using the general equilibrium equality by

$$\int_0^\infty \langle \dot{B}_1(0).\dot{B}_2(t)\rangle dt = \lim_{t\to\infty}\frac{1}{2t}\left\langle [B_1(t)-B_1(0)].[B_2(t)-B_2(0)]\right\rangle \tag{3.22}$$

where B is any scalar dynamical quantity and the dots denote time derivatives. The Einstein form of this equation, from the displacements of the centers of mass of swarms of i and j type molecules with time [112] is

$$L_{ij} = \frac{1}{2d_o V k_B T}\lim_{t\to\infty}\frac{1}{t}\left\langle \sum_{l=1}^{N_i}\left(r_{il}(t)-r_{il}(0)\right).\sum_{l^*=1}^{N_j}\left(r_{jl^*}(t)-r_{jl^*}(0)\right)\right\rangle \tag{3.23}$$

where $r_{il}(t)$ stands for the position vector of the *l*th molecule of species i at time t. Here macroscopic time scale is reflected by subsequently taking the limit of $t \to \infty$. Using Einstein form instead of Green-Kubo formalism has distinct advantages in simulations.

In addition to chemical potential, using L_{ij} is also not practical in experiments. Linear response theory states that time integrals of the autocorrelation functions are related to transport coefficients, so relating phenomenological coefficients with diffusion coefficients is required. There are three types of diffusivities used in characterizing different aspects of molecular transport and mobility within a nanoporous material; transport diffusivity, self diffusivity and corrected diffusivity. In the absence of force fields and isothermal/steady-state conditions, the transport diffusivity D_i for an adsorbed species i is defined by Fickian form [113] as a proportionality constant between the macroscopic flux J_i and the negative of the concentration gradient ∇c_i in a system of thermodynamic equilibrium.

$$J_i = -D_i \nabla c_i \tag{3.24}$$

For a multi component system Equation 3.24 becomes,

$$J_i = -\sum_{j=1}^{N} D_{ij} \nabla c_j \quad \text{(i = 1,2,..,N)} \tag{3.25}$$

As it can be noticed, Fickian form uses concentration gradient instead of chemical potential gradient as a driving force for mass flux. The relation between Onsager phenomenological coefficients and transport diffusivity can be seen by introducing the relation between chemical potential of species i and its fugacity f_i for a multicomponent sorbate system which is shown below:

$$\nabla \mu_i = \sum_{j=1}^{N} \frac{k_B T}{c_j} \left(\frac{\partial \ln f_i}{\partial \ln c_j} \right)_{T, c_{N-j}} \quad \text{for i=1,2,..,N} \tag{3.26}$$

Using Eqaution 3.26, transport diffusivity can be written as:

$$D = L \cdot \Gamma \tag{3.27}$$

where Γ is the thermodynamic correction factor [114] which incorporates the dependence of the fugacity of the sorbed component on its intracrystalline concentration as shown below:

$$\Gamma_{ij} = \frac{k_B T}{c_j} \left(\frac{\partial \ln f_i}{\partial \ln c_j} \right)_{T, c_{N-j}} \tag{3.28}$$

For the binary sorbate mixture, conjugate and off-diagonal transport diffusivities can be written as a function of Onsager phenomenological coefficients [112] as shown below.

$$D_{ii} = \frac{k_B T}{c_i} \left[L_{ii} \left(\frac{\partial \ln f_i}{\partial \ln c_i} \right)_{T, c_j} + L_{ij} \left(\frac{\partial \ln f_j}{\partial \ln c_i} \right)_{T, c_j} \right] \tag{3.29}$$

$$D_{ij} = \frac{k_B T}{c_j} \left[L_{ii} \left(\frac{\partial \ln f_i}{\partial \ln c_j} \right)_{T, c_i} + L_{ij} \left(\frac{\partial \ln f_j}{\partial \ln c_j} \right)_{T, c_i} \right] \tag{3.30}$$

As it can be seen from the expressions above, transport diffusivity is related to time integral of the autocorrelation function of the microscopic flux of the sorbed component within nonporous material, and a thermodynamic term. For pure sorbed systems, transport diffusivity can be also written as:

$$D_i = D_{o,i}\left(\frac{\partial \ln f_i}{\partial \ln c_i}\right)_T \tag{3.31}$$

where

$$D_{o,i} = \frac{1}{d_o N_i}\int_0^\infty \langle j_i(0).j_i(t)\rangle dt \tag{3.32}$$

is the corrected diffusivity [115] as its name suggests it considers thermodynamic nonidealities. Corrected diffusivity exhibits weaker concentration dependence than transport diffusivity in most systems. Corrected diffusivity can be written in Einstein form as follows:

$$D_{o,i} = \frac{1}{2d_o N_i}\lim_{t\to\infty}\left\langle\left[\sum_{l=1}^{N_i}\left[r_{il}(t)-r_{il}(0)\right]\right]^2\right\rangle \tag{3.33}$$

Self diffusivity is a measure of the translational mobility of individual molecules. Under the condition of thermodynamic equilibrium, one “tags” a molecule of species i and follows its trajectory over a long time. If the motion is diffusive, the equilibrium ensemble average of the squared displacement of the molecule from its original position will eventually grow linearly with time. Self diffusivity $D_{self,,i}$ is expressed as [116]:

$$D_{self,i} = \frac{1}{d_o}\int_0^{\infty} dt\left\langle v_i(0).v_i(t)\right\rangle \tag{3.34}$$

Equation 3.34 relates self diffusivity averaged over a d_o dimensional space and time integral of velocity autocorrelation function of the translational (center of mass) velocity v of the sorbed molecule. Using statistics, Equation 3.34 can also be written as:

$$D_{self,i} = \frac{1}{d_o}\int_0^{\infty} dt\left\langle \frac{1}{N_i}\sum_{l=1}^{N_i} v_{il}(0).v_{il}(t)\right\rangle \tag{3.35}$$

or equivalently, averaging over time for the mean square displacement of the center of mass position vectors r of all the molecules in the system [117] can be used to reduce statistical error as shown below:

$$D_{self,i} = \lim_{t\to\infty}\frac{1}{2d_o t}\left\langle \frac{1}{N_i}\sum_{l=1}^{N_i}\left[r_{il}(t)-r_{il}(0)\right]^2\right\rangle \tag{3.36}$$

Corrected diffusivity can be also written in terms of self diffusivity as follows:

$$D_{o,i} = \frac{1}{d_o N}\int_0^{\infty}\sum_{i=1}^{N}\sum_{j=1}^{N}\left\langle v_i(0).v_j(t)\right\rangle dt = D_{self,i} + \frac{1}{d_o N}\int_0^{\infty}\sum_{i=1}^{N}\sum_{\substack{j=1\\ j\neq i}}^{N}\left\langle v_i(0).v_j(t)\right\rangle dt \tag{3.37}$$

As it can be seen, corrected diffusivity is splitted into a cross correlation part and autocorrelation part which gives self diffusivity. The summation over cross correlations represents how motion of a single particle is affected by the initial motion of its

surrounding particles. Although $D_{self,i}$ and $D_{o,i}$ are both kinetic properties, latter has a collective nature whereas former consider just individual molecules. In addition to $D_{self,i}$, $D_{o,i}$ comprises the sum of the off-diagonal cross correlations terms. Also some studies assume that corrected diffusivity is equal to self diffusivity by neglecting cross correlation terms which is known as Darken approximation [118].

In the limit of very low occupancy, when cross correlation functions between velocities of different molecules approach zero and autocorrelation terms become dominant, transport, self and corrected diffusivities become similar:

$$\lim_{c\to 0} D\ (c) = \lim_{c\to 0} D_{self}\,(c) = \lim_{c\to 0} D_o\,(c) \tag{3.38}$$

3.4. Key Parameters for Determining Membrane Performance

There are several parameters that are taken into account when describing membrane performance or selecting one membrane over another. In this thesis, membranes are compared with each other by considering their adsorption selectivity, diffusion selectivity, permeation selectivity and permeability. This part gives brief information about how these parameters can be calculated using molecular simulations.

In the case of binary fluid of components i and j within porous medium Z, the macroscopic mass flux is given by the following expression for component i.

$$J_i = -L_{ii}\nabla\mu_i - L_{ij}\nabla\mu_j \tag{3.39}$$

Incorporating Equation 3.39 instead of chemical potential gradients which depend on both intracrystalline concentrations, c_i and c_j gives:

$$J_i = -\frac{k_B T}{c_i}\left[L_{ii}\left(\frac{\partial \ln f_i}{\partial \ln c_i}\right)_{T,c_j} + L_{ij}\left(\frac{\partial \ln f_j}{\partial \ln c_i}\right)_{T,c_j} \right]\nabla c_i - \frac{k_B T}{c_j}\left[L_{ii}\left(\frac{\partial \ln f_i}{\partial \ln c_j}\right)_{T,c_i} + L_{ij}\left(\frac{\partial \ln f_j}{\partial \ln c_i}\right)_{T,c_j} \right]\nabla c_j \tag{3.40}$$

which is equivalent to Fickian form of mass flux as shown below:

$$J_i = -D_{ii}\nabla c_i - D_{ij}\nabla c_j$$

Here transport diffusivities and concentrations are measured in m^2/s and mol/m^3, respectively. Permeability of specie i (measured in $mol.m^{-1}.s^{-1}.Pa^{-1}$ or Barrers) is calculated using macroscopic mass flux as follows:

$$P_i = \frac{J_i \phi}{\Delta f_i / l} \tag{3.41}$$

where ϕ is porosity of the nanoporous membrane, Δf_i is fugacity difference across membrane (measured in Pa) and l is membrane thickness (measured in m). In this thesis several assumptions were done to simplify the permeability formula. The membrane is assumed to be lie in the x-y plane, so that transmembrane flow occurs only in z direction (with a total length of l) which reduces 3-dimensional concentration gradient term ∇c to one dimension which can be written as follows:

$$\nabla c_i \cong \frac{\left(c_i^{perm} - c_i^{feed}\right)}{l} \tag{3.42}$$

Noble gas mixtures are taken as ideal, which means that fugacity of the gas specie is assumed to be equal to its bulk gas mixture composition multiplied by the total pressure. Also, membrane permeate site pressure drop is assumed to be vacuum, which means that pressure drop of a gas specie is assume to be equal to its feed pressure. Additionally, by taking permeate site as vacuum, c_i^{perm} can be assumed to be negligibly small as compared to c_i^{feed}. By all of these simplifications permeability formula becomes:

$$P_i = \frac{\left(D_{ii}c_i + D_{ij}c_j\right)\phi}{f_i} \tag{3.43}$$

Equation 3.43 is known to be detailed formula of calculating membrane permeability and it is computationally affording since transport diffusivities should be calculated by determining Onsager phenomenological coefficients. For efficient screening of membranes, further simplifications on the permeability formula were done by several researchers [119-120].

In a binary system, when both components are dilute (in the limit $c_1 \to 0$ and $c_2 \to 0$), the straight thermodynamic derivatives tend to one,

$$\left(\frac{\partial \ln f_i}{\partial \ln c_i}\right)_{T,c_j} \cong 1 \tag{3.44}$$

while cross-derivatives tend to zero,

$$\left(\frac{\partial \ln f_i}{\partial \ln c_j}\right)_{T,c_i} \cong 0 \tag{3.45}$$

Furthermore, cross correlation functions between velocities of different molecules of the same or different species reduce to zero, making L_{12} negligible and L_{11} is equal to $D_{self,1}c_1/k_BT$ as it can be derived from Equation 19 and Equation 23. In this limit, by Equation 3.29, it is clear that conjugate transport diffusivities will be equal to self diffusivities ($D_{11} \cong D_{self,1}$ and $D_{22} \cong D_{self,2}$) and off-diagonal transport diffusivities (D_{12} and D_{21}) will be zero. By this simplification, in dilute concentration limits, permeability equation becomes as follows:

$$P_{i,app} = \frac{D_{self,i}c_i\phi}{f_i} \tag{3.46}$$

where $P_{i,app}$ stands for the approximate permeability calculation. Although several researchers [121-123] use this formula for fast screening of nanoporous material performances, in the case of finite concentrations, L_{12} is generally nonzero due to correlation between the velocities of molecules of different types [124].

Permeation selectivity, $S_{permeation(i,j)}$, is relative permeabilities of gas species in nanoporous material as shown below:

$$S_{permeation(i,j)} = \frac{P_i}{P_j} = \frac{\dfrac{\left(D_{ii}c_i + D_{ij}c_j\right)\phi}{f_i}}{\dfrac{\left(D_{ji}c_i + D_{jj}c_j\right)\phi}{f_j}} = \frac{\left(D_{ii}c_i + D_{ij}c_j\right)}{\left(D_{ji}c_i + D_{jj}c_j\right)}\frac{y_j}{y_i} \tag{3.47}$$

This can be approximated as:

$$S_{permeation(i,j),app} = \frac{P_i}{P_j} = \frac{\frac{D_{self,i} c_i \phi}{f_i}}{\frac{D_{self,j} c_j \phi}{f_j}} = \frac{D_{self,i}}{D_{self,j}} \frac{c_i}{c_j} \frac{y_j}{y_i} \tag{3.48}$$

In Equation 3.48, the ratio of self diffusivities is called diffusion selectivity and the ratio of adsorbed concentrations multiplied by ratio of bulk gas composition is called adsorption selectivity as follows:

$$S_{permeatio(i,j),app} = S_{adsorption(i,j),app} . S_{diffusion(i,j),app} \tag{3.49}$$

$$S_{adsorption(i,j),app} = \left(\frac{c_i}{c_j} \frac{y_j}{y_i} \right) \tag{3.50}$$

$$S_{diffusion(i,j),app} = \left(\frac{D_{self,i}}{D_{self,j}} \right) \tag{3.51}$$

Chapter 4

COMPUTATIONAL DETAILS

In the first part of this thesis, adsorption and diffusion of noble gases in MOFs were examined. In the second part, noble gas separation performances of MOF membranes were predicted using theoretical correlations. This chapter gives information about the computational methodologies applied in these two parts. In all parts, GCMC and EMD simulations were used. Therefore first section of this chapter gives details on GCMC and EMD simulations.

4.1. Calculating Adsorption and Diffusion of Noble Gases Using Molecular Simulations

Grand canonical Monte Carlo (GCMC) and equilibrium molecular dynamics (EMD) simulations were used to compute adsorption and diffusion of Xe, Kr, Ar and their binary mixtures in MOFs. We chose ten MOFs having different metal sites, organic linkers, topologies and pore sizes to represent a variety of MOF properties. Structural information of MOFs including unit cell parameters and pore sizes are given in Table 4.1.

IRMOF-1, the prototype of isoreticular MOFs, is a three dimensional cubic structure with pore sizes 10.9/14.3 Å in diameter [125]. It has been very widely studied in the literature for gas adsorption and separation applications [126-129]. CuBTC, also known as HKUST-1, has main channels 9 Å in diameter, surrounded by tetrahedral pockets with

diameters of 5 Å and windows of 3.5 Å wide [130]. Similar to IRMOF-1, CuBTC is one of the most widely examined MOFs for gas storage and separation [131-132]. Coordination Polymers of Oslo (CPO-27-M, M=Ni, Co) were recently reported, they have three dimensional structures with honeycomb-like topology that contains one dimensional channel in the honeycomb with a diameter of ~11 Å [133-134]. Among several zeolite imidazolate frameworks (ZIFs), ZIF-1, ZIF-2, ZIF-3 AND ZIF-10 were studied in this thesis. ZIF-1 is monoclinic, ZIF-2 is orthorhombic whereas ZIF-3 and ZIF-10 have tetragonal structures [135]. ZIF-1 (ZIF-2) has 6.9 Å pores in diameter with 3 Å (6 Å) pore apertures [136]. ZIF-3 (ZIF-10) has 6 Å (12.1 Å) pores in diameter with 4.6 Å (8.2 Å) pore apertures [135-136]. $Zn(bdc)(ted)_{0.5}$ and bioMOF-11 were chosen to represent MOFs with smaller pores. $Zn(bdc)(ted)_{0.5}$ is a tetragonal structure with one channel having cross section of 7.5×7.5 Å and a smaller channel with a cross section of 4.8×3.2 Å [137]. BioMOF-11 has a tetragonal structure and each cavity in the structure can accommodate a sphere with a diameter of 5.8 Å and the aperture of cavities is 5.2 Å [138]. The only experimental gas adsorption data for noble gases in MOFs to date is Xe adsorption in IRMOF-1 and Xe, Kr adsorption in CPO-27-Ni. Therefore, we considered these MOFs in this work to validate the accuracy of force field parameters by comparing experimental measurements and our molecular simulations.

The atomic positions of all MOFs were obtained from their experimental XRD data and rigid structures were used. We compared the results of molecular simulations using rigid and flexible force fields for Xe adsorption. The Dreiding [139] force field was used in all simulations to describe the atoms of the MOFs. For the metal atoms, the van der Waals parameters were taken from the Universal Force Field (UFF) [140] since they are not available in the Dreiding force field. Simulation results employing Dreiding force field agreed well with the available experimental data for single component adsorption isotherms of Xe in IRMOF-1, Xe and Kr in CPO-27-Ni.

Table 4.1: Structural properties of MOFs studied in this work.*

Material	Crystal type	a,b,c (Å)	α,β,γ (°)	Pore size (Å)	Porosity
BioMOF-11	Tetragonal	15.435,15.435,22.775	90,90,90	5.2,5.8	0.54
CuBTC	Cubic	26.243, 26.343, 26.343	90,90,90	3.5,5,9	0.72
CPO-27-Co	Hexagonal	25.885,25.885,6.806	90,90,120	11	0.41
CPO-27-Ni	Hexagonal	25.785,25.785,6.770	90,90,120	11	0.41
IRMOF-1	Cubic	25.669,25.669,25.669	90,90,90	10.9,14.3	0.79
ZIF-1	Monoclinic	9.740,15.266,14.936	90,98.62,90	3,6.9	0.69
ZIF-2	Orthorhombic	9.679,24.114,24.45	90,90,90	6.4,6.9	0.66
ZIF-3	Tetragonal	18.970,18.970,16.74	90,90,90	4.6,6	0.68
ZIF-10	Tetragonal	27.061,27.061,19.406	90,90,90	8.2,12.1	0.73
$Zn(bdc)(ted)_{0.5}$	Tetragonal	14.899,14.899,19.136	90,90,90	3.2,4.8,7.5	0.65

*Porosity and free volume values of MOFs were taken from the study of Wu et al. [141] except CPOs and $Zn(bdc)(ted)_{0.5}$ for which values were taken from Dietzel et al. [142] and Liu et al.[137], respectively.

Spherical Lennard-Jones (LJ) 12-6 potentials [143] were used to model Xe (ε/k=221 K, σ=4.01 Å), Kr (ε/k=166.4 K, σ=3.636 Å), Ar (ε/k=119.8 K, σ=3.4 Å) [74, 144]. The Lorentz-Berthelot mixing rules were employed to calculate the adsorbate-adsorbent and adsorbate-adsorbate LJ cross interaction parameters. The intermolecular potentials were truncated at 13 Å for adsorption and diffusion simulations. A minimum 2×2×2 unit cell simulation box was used for GCMC simulations. For EMD simulations, the size of the simulation box was increased up to 3×3×3 to contain enough particles at the lowest loadings. Periodic boundary conditions were applied in all simulations [145-146]. Conventional GCMC was employed to compute the single component and mixture adsorption isotherms of gases. The temperature and the fugacity of the adsorbing gases were specified and the number of adsorbed molecules was calculated at equilibrium.

Simulations at the lowest fugacity for each system were started from an empty MOF matrix. Each subsequent simulation at higher fugacity was started from the final configuration of the previous run. Simulations consisted of a total of 3×10^7 trial configurations with the last half of the configurations used for data collection. A configuration is defined as an attempted translation, or creation or deletion of the adsorbates. For the case of mixture simulations, there is also an attempted swap of the particle species.

4.2. Predicting Noble Gas Separation Performance of MOFs Using Molecular Simulations

The adsorption selectivity of MOFs for Xe from Xe/Kr and Xe/Ar mixtures was calculated using approximate formula, as in Equation 3.50, as follows:

$$S_{adsorption,(Xe/Kr),app} = \frac{\Theta_{Xe} / \Theta_{Kr}}{y_{Xe} / y_{Kr}} \tag{4.1}$$

$$S_{adsorption,(Xe/Ar),app} = \frac{\Theta_{Xe} / \Theta_{Ar}}{y_{Xe} / y_{Ar}} \tag{4.2}$$

where Θ_i are the adsorbed loading of gas species (measured in molecules/unitcell) calculated by GCMC and y_i are the bulk gas composition of gas species.

As discussed in previous studies [122], adsorption selectivity and working capacity (also known as delta loading) govern the costs of separation in adsorption-based separation

processes. Using GCMC simulations, the Xe working capacities of the MOFs were calculated as the difference between the gas uptakes at a total gas phase fugacity of 10 bar and a desorption pressure of 1 bar at room temperature.

Single component and mixture self diffusivities of each species were calculated using EMD simulations using Equation 3.51. The self diffusivities of gases in the pores of MOFs were reported as average diffusivities using $D_{self,i} = (D_{self,x,i}+D_{self,y,i}+D_{self,z,i})/3$ and 10 independent MD trajectories were collected for calculating self diffusivity. Among the MOFs we considered in this work, CPO-27-Ni and CPO-27-Co have one dimensional pores therefore, self diffusivities of noble gases in CPOs were reported only in z direction. The Nosé-Hoover thermostat in NVT-ensemble was used in all EMD simulations [90]. After creating initial states with the appropriate loadings using GCMC simulations, each system was first equilibrated with EMD for about 20 ps prior to taking data. Self diffusivities of each component were computed at various adsorbed loadings of Xe/Kr and Xe/Ar mixtures that were obtained from mixture GCMC simulations.

The Xe working capacities (WC_{Xe}) of MOFs were calculated as the difference of gas uptakes (n mol Xe/kg MOF) at an adsorption pressure of 10 bar and a desorption pressure of 1 bar at room temperature:

$$WC_{Xe,sim} = n_{Xe(10bar),GCMC} - n_{Xe(1bar),GCMC} \qquad WC_{Xe,theory} = n_{Xe(10bar),IAST} - n_{Xe(1bar),IAST} \tag{4.3}$$

The gas permeability through MOFs was calculated using the following expressions [60]:

$$P_{i,sim} = \frac{\phi \cdot D_{self,i,MD}^{mixture} \cdot c_{i,GCMC}}{f_i} \qquad P_{i,theory} = \frac{\phi \cdot D_{self,i,KP}^{mixture} \cdot c_{i,IAST}}{f_i} \tag{4.4}$$

Once adsorption and diffusion data of gas mixtures were obtained from detailed molecular simulations as described, the performance of each MOF as a membrane for Xe/Kr and Xe/Ar separations can be predicted. Approximate permeation selectivities were calculated as in Equation 3.49.

$$S_{permeation(Xe/Kr),app} = \frac{\Theta_{Xe} / \Theta_{Kr}}{y_{Xe} / y_{Kr}} \cdot \frac{D_{self,Xe}(\Theta_{Xe}, \Theta_{Kr})}{D_{self,Kr}(\Theta_{Xe}, \Theta_{Kr})} \tag{4.5}$$

$$S_{permeation(Xe/Ar),app} = \frac{\Theta_{Xe} / \Theta_{Ar}}{y_{Xe} / y_{Ar}} \cdot \frac{D_{self,Xe}(\Theta_{Xe}, \Theta_{Ar})}{D_{self,Ar}(\Theta_{Xe}, \Theta_{Ar})} \tag{4.6}$$

As it was mentioned in section 3.4, in these approximate expressions, the diffusion selectivity is defined as the ratio of self diffusivities of each gas in a binary mixture evaluated directly at their corresponding adsorbed compositions. Equation 3.49 approximates a membrane's permeation selectivity at a specified feed pressure and feed gas composition based on a single GCMC simulation and an EMD simulation performed at the loadings determined from this GCMC simulation. We reported the permeation selectivity of MOFs for Xe/Kr and Xe/Ar separations as a function of feed pressure at room temperature.

We finally computed ideal selectivity of MOFs for noble gas separations. The ideal selectivity is simply the ratio of adsorbed amounts of pure gases multiplied by the ratio of self-diffusivities. For a Xe/Kr separation, a MOF's separation performance at 10 bar can be calculated as following:

$$S_{ideal(Xe/Kr)sim.} = \frac{\Theta^{single}_{Xe,GCMC,10bar}}{\Theta^{single}_{Kr,GCMC,10bar}} \cdot \frac{D^{single}_{self,Xe,MD(10bar)}}{D^{single}_{self,Kr,MD(10bar)}} \quad (4.7)$$

Early studies have shown that ideal selectivity can be significantly different than the mixture selectivity [120]. A revised version of the ideal selectivity that considers the composition effect of the mixture was recently suggested [147]. This revised version calculates ideal selectivity by considering the single component adsorption and diffusion of each component at their partial pressure in the mixture. For example, the ideal selectivity of a MOF for a Xe/Kr:20/80 bulk mixture at 10 bar can be computed as following:

$$S_{ideal(Xe/Kr),sim.with\ composition\ effect} = \frac{(\Theta^{single}_{Xe,GCMC,2bar}) \big/ \Theta^{single}_{Kr,GCMC,8bar})}{y_{Xe} \big/ y_{Kr}} \cdot \frac{D^{single}_{self,Xe,MD(2bar)}}{D^{single}_{self,Kr,MD(8bar)}} \quad (4.8)$$

Similar calculations were carried out to estimate the ideal selectivity of MOFs for Xe/Ar separations. Further details can be found in our recently published article [148].

4.3. Predicting Noble Gas Separation Performances of MOFs Using Theoretical Correlations

In the second part of this thesis, Krishna-Paschek (KP) correlations and Ideal Adsorbed Solution Theory (IAST) were applied to predict Xe/Kr (Xe/Ar) mixture self diffusivities and Xe/Kr (Xe/Ar) mixture adsorption isotherms, respectively. This section gives details about how KP correlations and IAST were applied and calculation methods of both permeability and selectivities by theoretical correlations.

4.3.1. Computing Single Component and Mixture Diffusion Coefficients from MD

In this section single component self-diffusivity ($D_{self,i}^{single}$) and single component corrected diffusivity ($D_{o,i}$) were computed as a function of adsorbed loading using MD simulations in canonical ensemble for Xe, Kr and Ar. Mixture self-diffusivities ($D_{self,i}^{mixture}$) for Xe/Kr and Xe/Ar were computed at predefined adsorbed compositions of 50/50, 25/75 and 75/25 using NVT-MD simulations. The details of using MD simulations to compute single component and mixture diffusion coefficients have been described in previous studies [49, 149-150]. The intermolecular potentials were truncated at 13 Å and the simulation box was increased up to 2×4×4 to contain enough particles at the lowest loadings considered. After creating initial states with the appropriate loadings using GCMC simulations, each system was first equilibrated with EMD for about 20 ps prior to taking data. 20 independent MD simulations were collected to determine both single component and mixture self and corrected diffusivities for each loading we considered. To describe the framework atoms, the van der Waals parameters were taken from Dreiding [139] force field. For describing metal atoms which are not present in Dreiding force field, Universal Force Field (UFF) [140] was used. Spherical Lennard-Jones (12-6) potentials were used to model Xe, Ar and Kr atoms. To calculate the adsorbate-adsorbent and adsorbate-adsorbate LJ cross interaction parameters, Lorentz-Berthelot mixing rules were employed. The intermolecular potentials were truncated at 13 Å for adsorption and diffusion simulations. Periodic boundary conditions were applied in all simulations

4.3.2. Predicting Mixture Diffusivities Using KP Correlation

Once the single component self- and corrected diffusivities were computed using MD simulations, they were fitted to continuous functions of fractional loading to apply KP

correlation to predict the mixture self-diffusivities. Fractional loading of species i (θ_i) is defined as the ratio of adsorbed loading (Θ_i) to the saturation loading ($\Theta_{i,sat}$) which the latter is calculated from the GCMC simulations [151]:

$$\theta_i = \left(\Theta_i \middle/ \Theta_{i,sat} \right) \tag{4.9}$$

In fitting of single component self- and corrected diffusivities, the functions describing corrected diffusivities were constrained to give the observed self-diffusion coefficients at zero loading as required by the definition of diffusivities [45]. In contrast to Keskin et al. [152], we did not constraint these functions at the saturation loading to vanish because non-zero diffusivities were reported from the MD simulations at loadings close to the saturation. At least ten data points were collected from the MD simulations for single component self- and corrected diffusivities of each species between zero loading and saturation loading. In this way, the accuracy of the fitting was increased since no fitting was done to predict diffusivities when simulation data is not present. In an adsorbed mixture, two additional diffusion coefficients, the self-exchange ($Đ_{ii}^{corr}$) and the binary-exchange ($Đ_{ij}^{corr}$) diffusivities define the correlation effects which may occur due to the topology of the adsorbent or momentum transfer between adsorbed molecules [48] or the concerted motions of adsorbed molecule clusters [153-154]. The self-exchange diffusivities ($Đ_{ii}^{corr}$) of each species were calculated using the single component self- and corrected diffusivities by the following expression [45]:

$$Đ_{ii}^{corr}(\theta) = \frac{\theta}{\dfrac{1}{D_{self,i}^{single}(\theta)} - \dfrac{1}{D_{o,i}(\theta)}} \tag{4.10}$$

In order to use this expression for mixtures, we replaced the fractional single component occupancy with the fractional total occupancy [152], $\theta = \theta_i + \theta_j = \left(\Theta_i / \Theta_{i,sat}\right) + \left(\Theta_j / \Theta_{j,sat}\right)$. The binary exchange coefficients, $Đ_{ij}^{corr}$ were estimated by the following expression [155]:

$$\Theta_{j,sat} Đ_{ij}^{corr}(\theta) = \left[\Theta_{j,sat} Đ_{ii}^{corr}(\theta)\right]^{\Theta_i/(\Theta_i+\Theta_j)} \cdot \left[\Theta_{i,sat} Đ_{jj}^{corr}(\theta)\right]^{\Theta_j/(\Theta_i+\Theta_j)} \quad (4.11)$$

Once the single component self-exchange and binary-exchange diffusivities were calculated as described above, the KP correlation predicts the mixture self-diffusivities of each species ($D_{self,i}^{mixture}$) from pure component diffusivities as follows [45]:

$$D_{i,self}^{mixture} = \frac{1}{\frac{1}{D_{o,i}} + \frac{\theta_i}{Đ_{ii}^{corr}} + \frac{\theta_j}{Đ_{ij}^{corr}}} \quad (4.12)$$

We predicted self-diffusivities of Xe/Kr and Xe/Ar mixture at adsorbed compositions of 50/50, 25/75, 75/25 and compared these predictions with the results of mixture MD simulations.

4.3.3. Predicting Mixture Adsorption Using IAST

After evaluating the single component adsorption isotherms of each component up to 30 bar by GCMC, dual-site Langmuir or dual-site Freundlich model was fitted to single component adsorption isotherms of Xe, Kr and Ar in all MOFs:

$$\Theta_{i,Langmuir} = \frac{aP}{b+P} + \frac{cP}{d+P} \qquad \Theta_{i,Freundlich} = \frac{eP^f}{g+P^f} + \frac{hP^k}{m+P^k} \tag{4.13}$$

In these models, P is the pressure (bar) and others are parameters of the models. The saturation loadings ($\Theta_{i,sat}$) of the single components were evaluated at infinitely large pressures. Using fitted adsorption isotherms and applying IAST [44, 52], adsorption isotherms of Xe/Kr and Xe/Ar mixtures were predicted. IAST assumes ideal gas behavior and does not consider the adsorbent heterogeneity, therefore it works very well at low pressures and for materials with homogenous adsorption sites. IAST has been widely used to predict mixture adsorption in MOFs such as C_2H_4/C_2H_6 adsorption in ZIF-8 [156], CH_4/N_2 adsorption in MFI, MIL-47, IRMOF-12 [157], CO_2/N_2 adsorption in IRMOF-3, MOF-177, UMCM-1[158] and it was found to make accurate predictions.

4.3.4. Predicting Selectivity and Permeability of MOFs Using Theoretical Correlations

The main objective of this part is to examine if one can evaluate the noble gas separation performance of MOFs using theoretical correlations without performing computationally demanding mixture simulations as explained in section 4.1. We calculated adsorption selectivity, permeation selectivity, working capacity and gas permeability of MOFs for Xe/Kr and Xe/Ar mixtures using theoretical correlations, namely IAST and KP, and compared our findings with the results of mixture simulations, GCMC and EMD. Permeation selectivity ($S_{permeation(i/j)}$) can be approximated as the multiplication of adsorption selectivity ($S_{adsorption(i/j)}$) and diffusion selectivity ($S_{diffusion(i/j)}$) as mentioned before.

$$S_{permeation_{(i/j),sim}} = S_{adsorption_{(i/j),GCMC}} \cdot S_{diffusion_{(i/j),MD}} = \frac{(\Theta_{i,GCMC}) \big/ (\Theta_{j,GCMC})}{y_i \big/ y_j} \cdot \frac{D_{self,i}^{mixture}(\Theta_i, \Theta_{j,})_{,MD}}{D_{self,j}^{mixture}(\Theta_i, \Theta_j)_{,MD}} \tag{4.14}$$

The adsorbed loadings were obtained from the mixture GCMC simulations and the bulk phase composition of Xe/Kr and Xe/Ar mixtures was set to 20/80 to represent the industrial gas separation conditions. The adsorption and permeation selectivity of MOFs for Xe/Kr and Xe/Ar separations can be estimated using only the pure component data and theoretical correlations as follows:

$$S_{permeation_{(i/j),theory}} = S_{adsorption_{(i/j),IAST}} \cdot S_{diffusion_{(i/j),KP}} = \frac{(\Theta_{i,IAST}) \big/ (\Theta_{j,IAST})}{y_i \big/ y_j} \cdot \frac{D_{self,i}^{mixture}(\Theta_i, \Theta_{j,})_{,KP}}{D_{self,j}^{mixture}(\Theta_i, \Theta_j)_{,KP}} \tag{4.15}$$

In these expressions, mixture adsorption amounts of each species were calculated from IAST based on pure component adsorption isotherms and the mixture self-diffusivities were calculated using KP correlation based on single component self-, corrected and exchange diffusivities. We compared the adsorption selectivities calculated from simulations ($S_{adsorption(i/j),GCMC}$) with the ones calculated from theory ($S_{adsorption(i/j),IAST}$) and permeation selectivities calculated from simulations ($S_{permeation(i/j),sim}$) with the ones calculated from the theory ($S_{permeation(i/j),theory}$) at 298 K and 10 bar.

Chapter 5

MOLECULAR MODELING OF MOFs FOR NOBLE GAS SEPARATIONS

This chapter gives all results and discussions of calculations. Firstly, the results of modeling MOFs for adsorption and diffusion were given and the effects of pore size and structure, loading, pore heterogeneity on adsorption and diffusion were discussed. In the second part, predicting noble gas separation performances of MOFs by molecular simulations and theoretical correlations were examined and probable reasons of deviation between the results of correlations and simulations were discussed.

5.1. Modeling MOFs for Adsorption, Diffusion and Separation of Noble Gas Mixtures

We first compared the results of our molecular simulations with the available experimental data for adsorption of noble gases in MOFs. Figure 5.1a shows experimental Xe adsorption isotherm of IRMOF-1 at 292 K, simulated Xe adsorption isotherm by Greathouse et al. [75] using flexible framework and our simulated Xe adsorption isotherm using rigid framework. Greathouse et al. used the LJ parameters defined by Dubbeldam et al. [159] for IRMOF-1 atoms whereas we used Dreiding force field parameters. There is a very good agreement between experiments and molecular simulations at low pressures, but at higher pressures, simulations employing flexible force field underestimated the experimental data. Results of our molecular simulations using Dreiding force field and rigid framework assumption agreed well with the experimental adsorption isotherm of Xe

in IRMOF-1. Thallapally et al. [81] very recently measured single component Xe and Kr adsorption isotherms at room temperature in CPO-27-Ni and activated carbon. Figure 5.1b shows that our simulation results agree with the experimental data both for Xe and Kr adsorption. For example, experiments reported Xe uptake of 55.6 wt% at 1 bar, 298 K and our simulations predicted 59.1 wt% under the same conditions. The uptake capacity of CPO-27-Ni is higher than that of activated carbon which adsorbs 48 wt% Xe at 1 bar, 298 K.

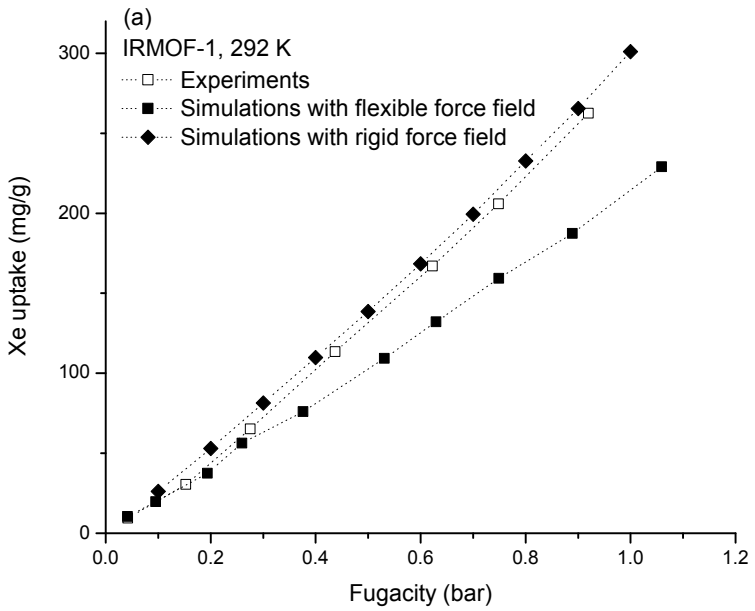

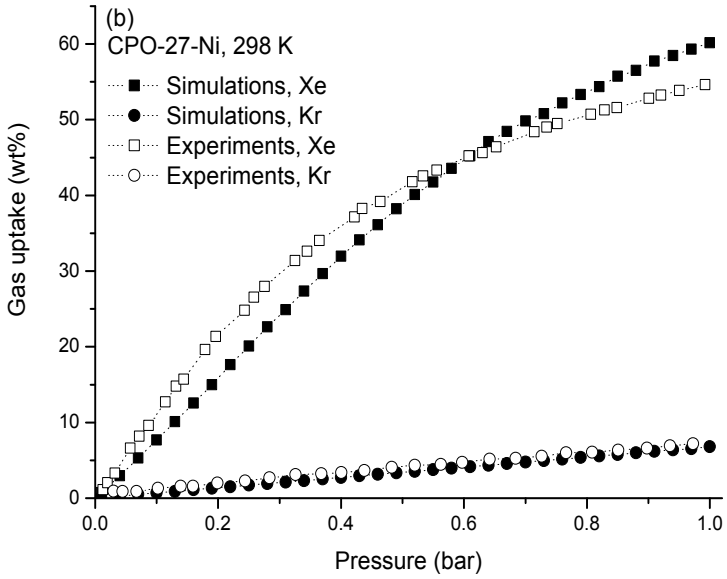

Figure 5.1: Experimental and simulated adsorption isotherms of a)Xe in IRMOF-1 b)Xe and Kr in CPO-27-Ni. Experimental data was taken from a) Greathouse et al. [75] b) Thallapally et al. [81]

Single component Xe, Kr, Ar uptakes of MOFs at 5 bar and 10 bar were tabulated in Table 5.1. We also included the experimental measurements of Bazan et al. [160] for Xe, Kr, Ar uptakes in three zeolites, SorboNorit B3, Koestrolith 13X-K2 and Koestrolith 4AK. The comparison between zeolites and MOFs showed that MOFs considered in this work exhibit higher Xe, Kr and Ar uptake capacities than Koestrolith 4AK. All MOFs except bioMOF-11 and ZIF-1 have higher Kr and Ar uptake capacities than Koestrolith 13X-K2 and SorboNorit B3 at 10 bar. These results suggest that MOFs studied in this work can be potential candidates for noble gas storage.

Table 5.1: Single component uptakes of Xe, Kr and Ar in MOFs and zeolites.

	Xe (mmol/g)		Kr (mmol/g)		Ar (mmol/g)	
MOFs (298 K, this work)	5 bar	10 bar	5 bar	10 bar	5 bar	10 bar
BioMOF-11	3.84	3.91	2.44	3.21	0.93	1.62
CuBTC	8.95	10.03	3.95	6.60	1.73	3.03
IRMOF-1	11.45	15.80	2.78	5.57	1.31	2.57
CPO-27-Co	7.12	7.92	3.67	5.78	1.29	2.40
CPO-27-Ni	6.73	7.34	3.45	5.38	1.25	2.29
ZIF-1	2.68	2.83	2.39	2.87	1.23	1.84
ZIF-2	6.12	6.60	4.36	5.80	1.83	3.08
ZIF-3	8.08	8.79	3.79	5.69	1.59	2.70
ZIF-10	8.26	9.63	2.64	4.72	1.09	2.07
$Zn(bdc)(ted)_{0.5}$	8.47	8.93	5.51	7.35	2.11	3.67
Zeolites (303 K, Bazan et al.[160])						
SorboNorit B3	5.58	-	2.8	3.79	0.95	1.70
Koestrolith 13X-K2	9.18	9.83	2.58	4.00	0.44	0.73
Koestrolith 4AK	~1.60	-	1.17	1.66	0.41	0.72

Single component adsorption isotherms of Xe, Kr, Ar and binary adsorption isotherms of Xe/Kr and Xe/Ar mixtures in all MOFs at 298 K were shown in Figures A.1 and A.2 of Appendix. As representatives, adsorption isotherms of CPO-27-Ni, ZIF-3 and $Zn(bdc)(ted)_{0.5}$ were given in Figure 5.2. Adsorption of Xe is higher than that of Kr and Ar in all MOFs due to energetic effects. As the pressure increases, Xe reaches saturation whereas smaller Kr atoms can still find places in the narrow pores of bioMOF-11, CuBTC, ZIF-2 and $Zn(bdc)(ted)_{0.5}$. Therefore, Kr adsorption gets higher than Xe at higher pressures

in these materials due to entropic effects. As should be expected from the single component isotherms, mixture GCMC simulations showed that adsorption favors Xe over Kr and Ar in the mixtures because the more strongly adsorbing Xe atoms exclude the weakly adsorbed ones in the pores.

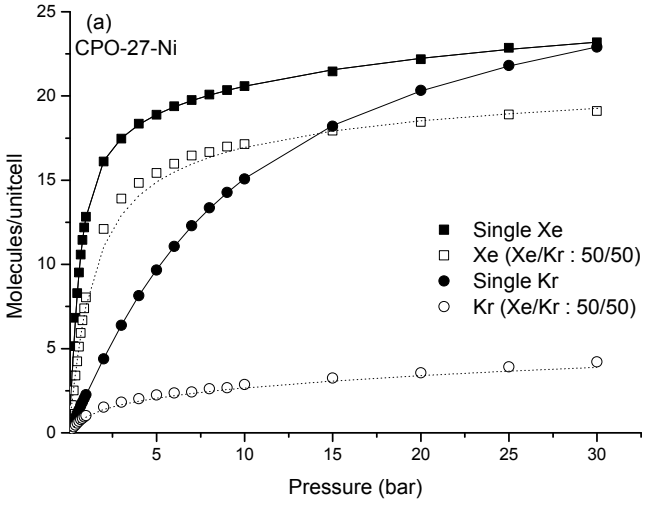

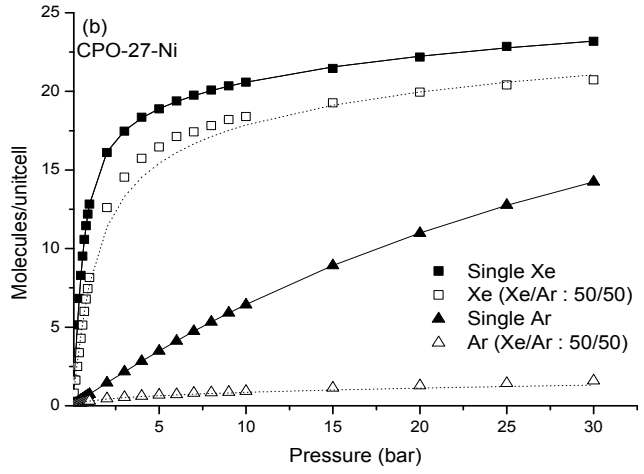

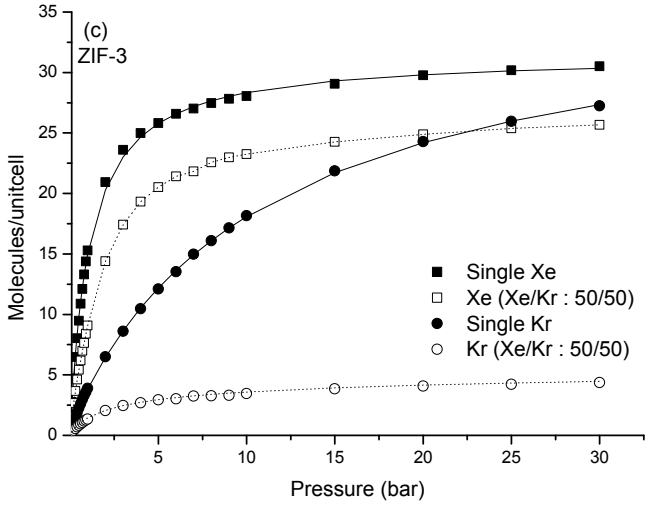
(c)
ZIF-3
Molecules/unitcell
Pressure (bar)
Single Xe
Xe (Xe/Kr : 50/50)
Single Kr
Kr (Xe/Kr : 50/50)

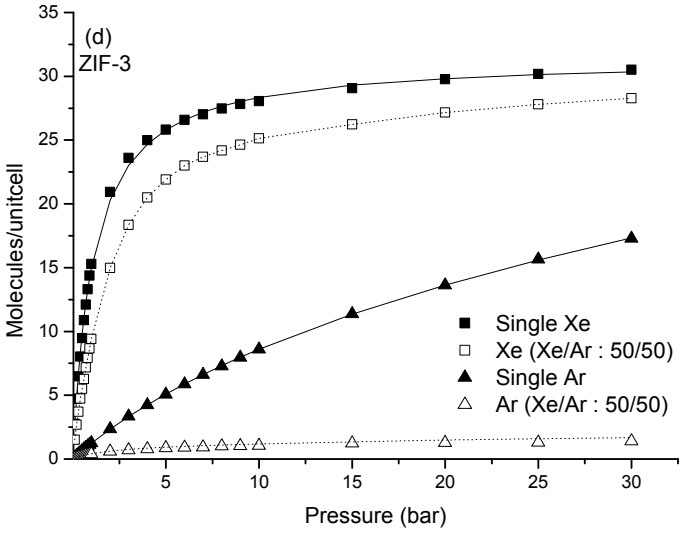
(d)
ZIF-3
Molecules/unitcell
Pressure (bar)
Single Xe
Xe (Xe/Ar : 50/50)
Single Ar
Ar (Xe/Ar : 50/50)

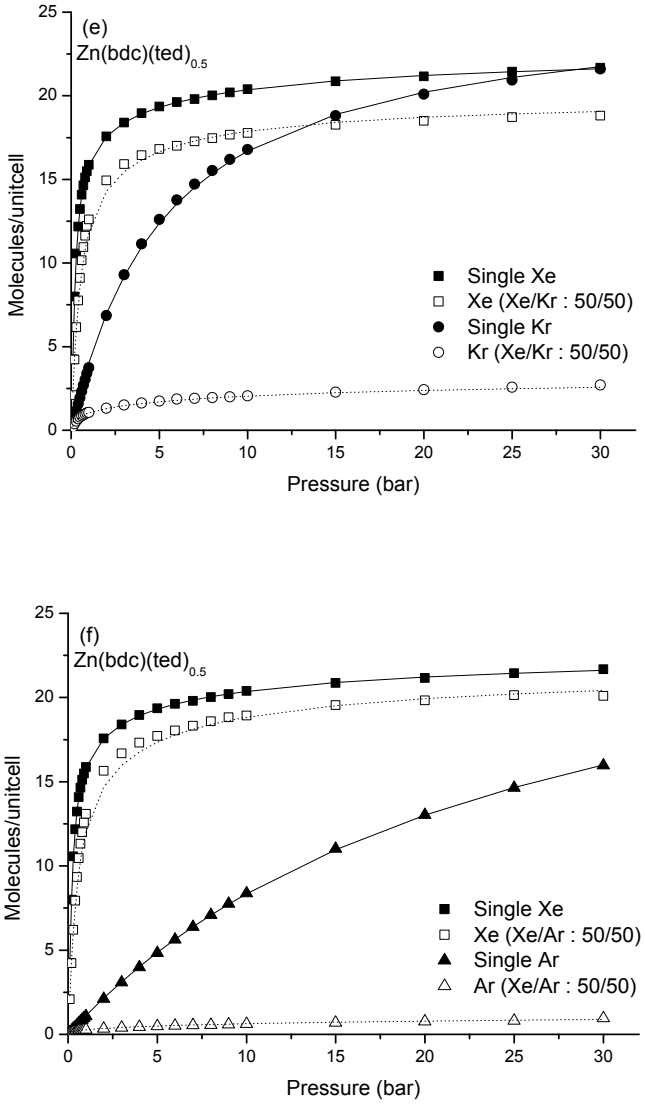

Figure 5.2: Single component and binary adsorption isotherms of Xe/Kr and Xe/Ar in a-b)CPO-27-Ni c-d)ZIF-3 e-f)Zn(bdc)(ted)$_{0.5}$ at room temperature. The compositions of the bulk gas mixture are equimolar. The continuous and dotted lines represent the fitted single component adsorption isotherm and the prediction of IAST, respectively.

We used Ideal Adsorbed Solution Theory (IAST) [44] to determine whether pure gas adsorption isotherms could be used to make accurate predictions for mixture isotherms. IAST is well known to give accurate predictions for mixture adsorption isotherms based on adsorption isotherms of pure gases in many nanoporous materials except in materials characterized by strong energetic or geometric heterogeneity [161-162]. In order to apply IAST, we fitted dual-site Langmuir and dual-site Freundlich models to single component adsorption isotherms of Xe, Kr and Ar. The single component isotherms fits and the predictions of IAST were shown in Figure 5.2 by continuous lines and dotted lines, respectively. The predictions of IAST agree fairly well with the mixture GCMC simulations of MOFs.

After mixture adsorption data was obtained using GCMC simulations, we estimated the performances of MOFs in adsorption-based noble gas separation applications. The adsorption selectivities of MOFs as a function of Xe composition in the bulk phase at 1 bar and 10 bar for Xe/Kr and Xe/Ar mixtures are shown in Figures A.3 and A.4. Our values for Xe/Kr selectivity of IRMOF-1 (3.5-4.3) agreed well with the previous results of Ryan et al. [74] and our values for Xe/Ar selectivity of IRMOF-1 (7-11.2) agreed with the previous results of Greathouse et al. [75] MOFs having small pores such as bioMOF-11, $Zn(bdc)(ted)_{0.5}$, ZIF-1, ZIF-2, CuBTC exhibit higher adsorption selectivities (7-16 for Xe/Kr and 19-79 for Xe/Ar) than MOFs having large pores such as IRMOF-1, CPO-27-Ni and CPO-Co (3-8 for Xe/Kr and 7-28 for Xe/Ar). This can be explained with the following discussion: Materials with relatively smaller pores provide a stronger confinement for Xe atoms whereas the degree of confinement of Kr or Ar atoms in small pores and large pores can be thought as being similar, because in both cases the atom is small relative to the pore size, giving similar adsorption strength. The stronger confinement of Xe in narrow-pore MOFs results in higher adsorption selectivity for Xe.

Figure 5.3 shows that Xe selectivity from Xe/Ar mixtures is higher than the one from Xe/Kr mixtures. The adsorption selectivity was greatly enhanced when Xe was mixed with smaller atoms (Ar) compared to the larger atoms (Kr). For example, at 1 bar, ZIF-2 (ZIF-10) exhibits Xe selectivity of ~10 and ~40 (~5 and ~15) from equimolar Xe/Kr and Xe/Ar mixtures, respectively. The effect of feed gas composition on the adsorption selectivity can be also seen in Figures 5.3, A.3 and A.4. As the composition of Xe in the feed increases, the adsorbed amount of Xe (Kr or Ar) increases (decreases). The selectivities of ZIF-2 and ZIF-10 shown in Figure 5.3 are largely independent of the feed composition of Xe at 1 bar. As discussed in previous studies [61, 75], adsorbate-adsorbate interactions become more dominant at 10 bar and Xe selectivity becomes composition dependent at this pressure.

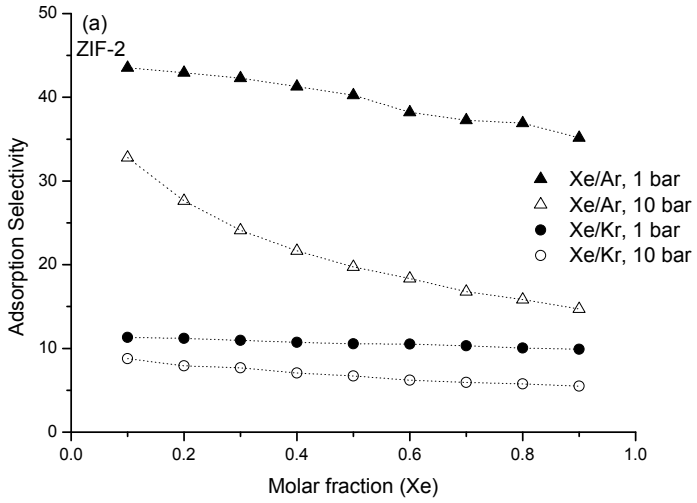

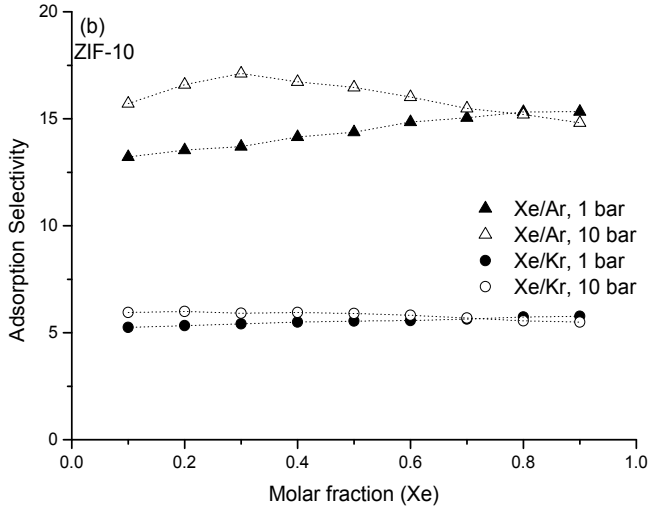

Figure 5.3: Effect of feed gas composition and pressure on Xe selectivity for Xe/Kr and Xe/Ar separations.

Maintaining the selectivity across a wide range of pressures is also desired for an adsorption-based separation process. Figures A.3-A.4 show that materials having small pores/pockets exhibit high adsorption selectivities at 1 bar but this selectivity drops off quickly at 10 bar. For example, Xe is strongly confined in the narrow pores of CuBTC, $Zn(bdc)(ted)_{0.5}$, ZIF-1, ZIF-2 and these MOFs exhibit high Xe selectivity over Kr and Ar at 1 bar. However, as pressure is increased to 10 bar, small pockets are filled and adsorbates go into the large cavities of the MOFs, hence Xe selectivity decreases. This result suggests that MOFs with uniformly small pores without large cavities can be better candidates for noble gas separations.

Figure 5. 4 compares the adsorption selectivities and working capacities of MOFs. The adsorption selectivities and working capacities were calculated for Xe/Kr:20/80 mixtures to

represent an industrial gas mixture. [43] The most desirable materials for adsorption-based separation of noble gases should be located in the top right hand corner of Figure 5.4.

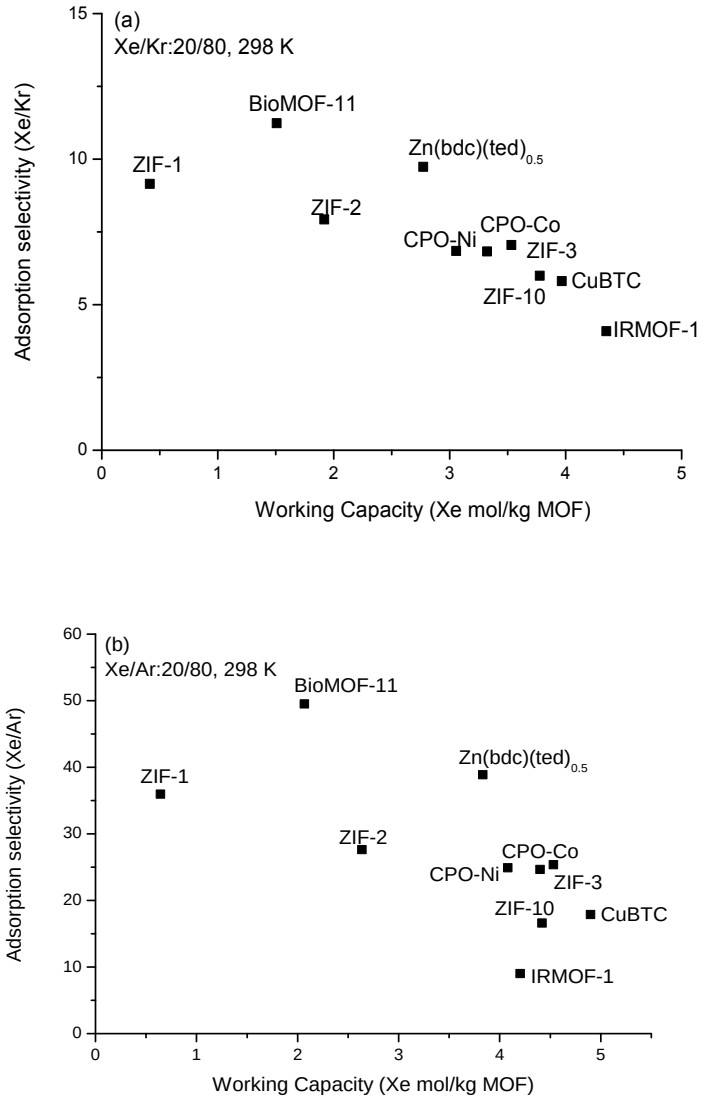

Figure 5.4: Adsorption selectivity and working capacity of MOFs for a)Xe/Kr and b)Xe/Ar separations.

The results of molecular simulations showed that there is a trade-off between adsorption selectivity and working capacity. For example, ZIF-1 exhibits good Xe/Kr selectivity (~9) but low Xe working capacity (~0.41 mol Xe/kg MOF) whereas IRMOF-1 has a high working capacity (~4.35 mol Xe/kg MOF) but low selectivity (~4). Among the MOFs studied in this work, $Zn(bdc)(ted)_{0.5}$ can be considered as the material with the best Xe selectivity/working capacity combination (10 and 2.77 mol Xe/kg MOF, respectively). It is also important to compare the separation performance of MOFs with that of well known zeolites. Previous research showed that NaX zeolite has a selectivity of ~6 for Xe over Kr [74, 163]. NaA zeolite has a Xe selectivity of 4-4.5 (20-25) from an equimolar Xe/Kr (Xe/Ar) mixture at 300 K between 1-10 bar [164]. Except IRMOF-1 and ZIF-10 all the MOFs considered in this thesis show higher Xe selectivity than NaA and NaX. For example, under the same conditions, $Zn(bdc)(ted)_{0.5}$ has a Xe selectivity of 10-12.5 (30-50) for Xe/Kr (Xe/Ar) separations.

The transport rates of gas components inside the material of interest are crucial in determining the overall performance of this material in gas separation applications. We computed self diffusivities of Xe/Kr and Xe/Ar mixtures in MOFs using EMD simulations. As expected, strongly adsorbed component diffuses slowly compared to the weakly adsorbed component. For example, room temperature self diffusivities of Xe and Kr (Ar) in Xe/Kr:20/80 (Xe/Ar:20/80) mixtures in IRMOF-1 were 5.7×10^{-5} and 1.2×10^{-4} (2.3×10^{-4}) cm^2/s, respectively. Our diffusivity data agreed well with the previously reported Ar diffusion in IRMOF-1 [98]. The self diffusivities of Xe were computed as $1\text{-}5\times10^{-5}$ cm^2/s in $Zn(bdc)(ted)_{0.5}$, IRMOF-1, ZIFs and $\sim10^{-4}$ cm^2/s in CPOs. These diffusivities are comparable with the ones in carbon nanotubes and zeolites. Nasrabadi et al. [165] recently used EMD simulations and calculated self diffusivities of Xe and Kr (Ar) in a (10,10) single walled carbon nanotube at 300 K as 7.5×10^{-6} and 1.7×10^{-5} (3.4×10^{-5}) cm^2/s. Bergh et al. [166] reported self diffusivity of Ar using EMD simulations in DDR, CHA, FAU, MFI

as 1-2×10^{-5}, 3×10^{-5}, 04×10^{-5} and 0.5-2×10^{-4} cm^2/s, respectively. Luca et al. [167] reported calculated and experimental diffusivities of Ar and Xe as 2-3.1×10^{-6} and 2.7-2.8×10^{-5} cm^2/s.

Using adsorption and diffusion selectivities calculated from GCMC and EMD simulations, we estimated permeation selectivities of MOFs for Xe/Kr and Xe/Ar mixtures. In Figure 5.5, the selectivity greater than 1 indicates that MOF is selective for Xe. As discussed before, adsorption selectivity favors Xe due to energetic effects but it was compensated by the low diffusion selectivities towards Xe since strongly adsorbed Xe species diffuse more slowly than the weakly adsorbed species. As a result, permeation selectivities of MOFs for Xe are smaller than their adsorption selectivities. As an example, adsorption selectivity of bioMOF-11 for Xe/Kr mixture is 11 at 10 bar, 298 K whereas diffusion selectivity is 0.6 indicating that Kr diffuses 1.6 times faster than Xe in the pores of bioMOF-11. The combined effect of adsorption and diffusion preferences resulted in Xe selective bioMOF-11 membrane with a selectivity of 6.6.

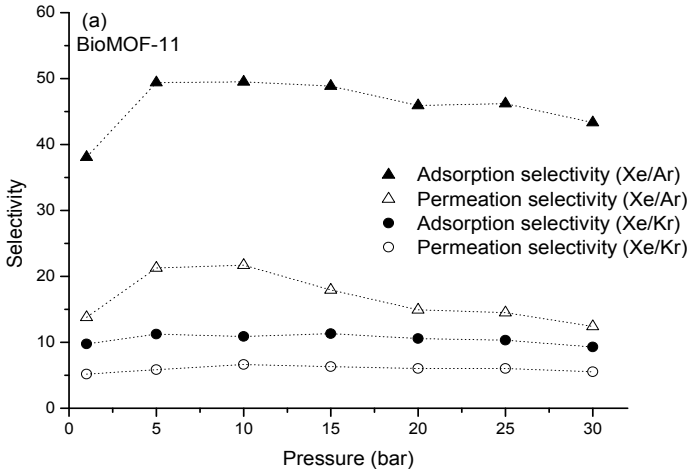

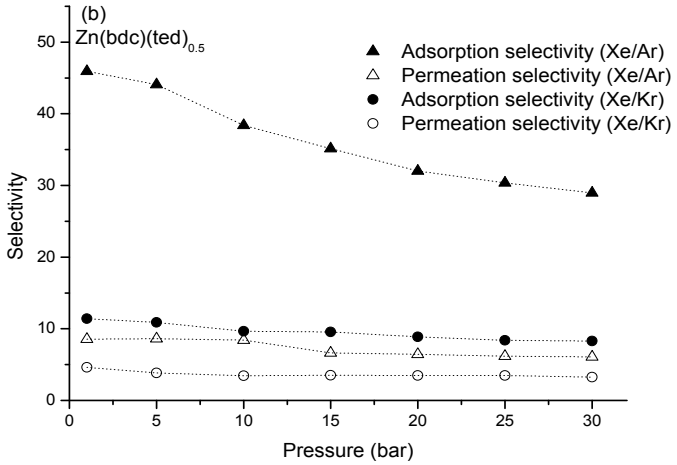

Figure 5.5: Adsorption and permeation selectivity of MOFs at 298 K as a function of pressure. The composition of the bulk gas mixture is 20/80.

Figure 5.6 compares permeation selectivity and permeability of MOFs for Xe/Kr and Xe/Ar separations at a feed pressure of 10 bar. The most desirable materials for permeation-based separation of noble gases should have both high permeation selectivity and high permeability. High permeability is desired to perform the separation with a smaller membrane area, thus low capital cost. Figure 5.6 shows that CPOs having one dimensional large pores in z direction exhibit higher Xe permeability than all other MOFs. This can be attributed to the high adsorption and fast diffusion of Xe in CPOs (17 molecules per unit cell and 10^{-4} cm^2/s at 10 bar, 298 K).

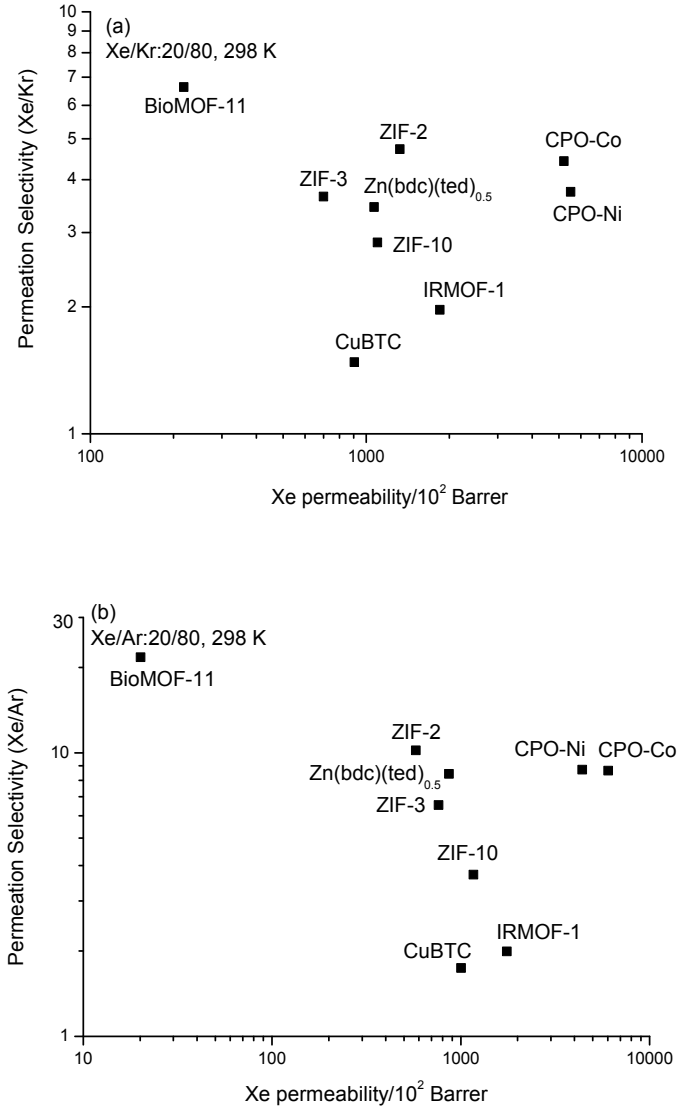

Figure 5.6: Permeation selectivity and gas permeability of MOFs at 10 bar for a)Xe/Kr and b)Xe/Ar separations.

Figure 5.6.b shows the Xe permability of CPO-27-Co is slightly higher than that of CPO-27-Ni which can be attributed to the stronger confinement of Xe atoms in the former due to the larger kinetic diameter of Co atoms that constraints the pores. Since both adsorption and diffusion selectivities of CPOs are close to each other, it is expected to see similar permeation selectivities for these two materials. The diffusivity of Xe in bioMOF-11 is low ($6\text{-}8\times10^{-7}$ cm^2/s), therefore permeability of this MOF is lower than the other MOFs. It is important to compare the noble gas permeability of MOF membranes with other nanoporous membranes to assess the performance of MOFs in noble gas separations. Sholl [168] computed single component steady state permeance of Xe through a 10 μm thick $AlPO_4$-31 single crystal membrane as 10^{-5} $mol/m^2/s/Pa$ at 300 K. Our calculated Xe permeances were $7.3\times10^{-7}\text{-}1.8\times10^{-5}$ $mol/m^2/s/Pa$ at 298 K for Xe/Kr:20/80 bulk gas mixtures in 10 μm thick MOF membranes. Nakai et al. [169] measured permeability of Xe in cellulose acetate membranes as 0.97-2.7 Barrers whereas we calculated Xe permeabilities in a range of 2-55 Barrers in MOFs. Considering the porosity of MOFs, it is natural to observe higher gas permeabilities in MOF membranes compared to polymer membranes [148].

5.2. Predicting Noble Gas Separation Performances of MOFs Using Theoretical Correlations

The results we showed in Figure 5.6 were obtained from detailed molecular simulations. We then examined whether theoretical correlations can be used to predict separation performances of MOFs instead of computationally demanding simulations. We first examined the accuracy of KP correlation for predicting the mixture self-diffusivities of noble gases in MOFs by comparing the theoretical predictions with the results of mixture MD simulations. Based on this comparison, we categorized the MOFs into three groups:

MOFs for which the predictions of KP correlation are in a very good agreement with the simulations (IRMOF-1, ZIF-3 and ZIF-10), MOFs for which the predictions of KP correlation are in a reasonable agreement with the simulations (ZIF-2, $Zn(bdc)(ted)_{0.5}$, CPO-Ni and CPO-Co) and finally MOFs for which the predictions of KP correlation do not agree with the simulations (bioMOF-11 and CuBTC). In every case, we showed the results for one representative MOF and the results of all other MOFs for Xe/Kr and Xe/Ar mixtures are given in Figure B.1 and Figure B.2 of the Appendix, respectively.

In all MOFs, the magnitude of the single component self-diffusivities has the following order: $D_{self,Xe} < D_{self,Kr} < D_{self,Ar}$. The adsorbate with the highest interaction energy parameter (Xe) has a stronger adsorption tendency and therefore lower mobility whereas the adsorbate with the lowest interaction energy parameter (Ar) has a higher tendency to diffuse. The diffusion order also agrees with the molecular weight of the gases, the lighter adsorbate (Ar) shows the higher diffusivity. As expected from the single component diffusion behavior, Kr (Ar) diffuses faster than Xe in Xe/Kr (Xe/Ar) mixtures in all MOFs we studied.

Figure 5.7 shows the self-diffusivities of Xe/Kr mixture as a function of total adsorbed loading at three different adsorbed compositions in IRMOF-1. The predictions of KP correlation agree well with the results of mixture MD simulations at all loadings. This good agreement between theory and simulations can be explained by considering the mixture correlation effects: IRMOF-1 is the most porous material among the ones we considered in this work with a large cavity diameter of ~15 Å and total pore volume of 74%. Due to this high free volume, the adsorbates act as they are in the single component case. For example, the presence of the slow Xe (fast Kr) atoms does not significantly decrease (increase) the diffusion of fast Kr (slow Xe) atoms. This shows that the correlation effects between different adsorbates are negligible, which leads to high accuracy of KP. Another observation from Figure 5.7a-c is that the mixture self-diffusivities of Xe and Kr are almost

independent from the adsorbed loading since the material's free volume is high and both gases are away from saturation. Figure 5.7d compares the predictions of KP correlation with the results of mixture MD simulations at all compositions and suggests that KP correlation accurately predicts the self-diffusivities of Xe/Kr mixtures at various conditions. The same discussion is valid for Xe/Ar mixtures in IRMOF-1 and the results are shown in Figure A.2. As we mentioned in the beginning of discussion, KP also makes accurate predictions for self-diffusivities of Xe/Kr and Xe/Ar mixtures in ZIF-3 and ZIF-10 using pure component diffusivities of Xe, Kr and Ar. These MOFs also possess larger cavity diameters and higher free volumes compared to the other MOFs we considered in this work. Similar to IRMOF-1, the self-diffusivity values for Xe/Kr and Xe/Ar mixtures do not significantly change with the loadings in ZIF-3 and ZIF-10.

In Figure 5.8, we showed the results of ZIF-2, a representative MOF for which there is a fair agreement between theory and simulations for self-diffusivities of noble gas mixtures. The KP correlation captures the diffusion behavior of equimolar mixtures well but make less accurate predictions if one component is dominated in the adsorbed mixture. Figure 5.8a shows that the self-diffusivities of Xe and Kr are almost independent from the adsorbed loadings in an equimolar adsorbed mixture and the KP predictions agree well with the simulations at this composition. On the other hand, Figure 5.8b shows that the diffusivity of Kr decreases sharply when the concentration of slowly diffusing Xe atoms increases in the mixture. It is well known that more mobile components (in our case Kr) are much affected from the correlation effects compared to slow components [45]. Since the slower component (Xe) does not vacate the adsorption site quickly, a sharp decrease is observed in Kr diffusivity. Here it is important to explain why we did not study the mixture of Xe/Kr:25/75 in ZIF-2. The industrial gas mixture has a bulk composition of Xe/Kr:20/80 (Xe/Ar:20/80) which corresponds to adsorbed compositions of Xe>50 in all MOFs (see Table B.1 and Table B.2). The minimum adsorbed Xe composition was observed in

IRMOF-1. Therefore, except IRMOF-1, we did not show the results for Xe/Kr:25/75 and Xe/Ar:25/75.

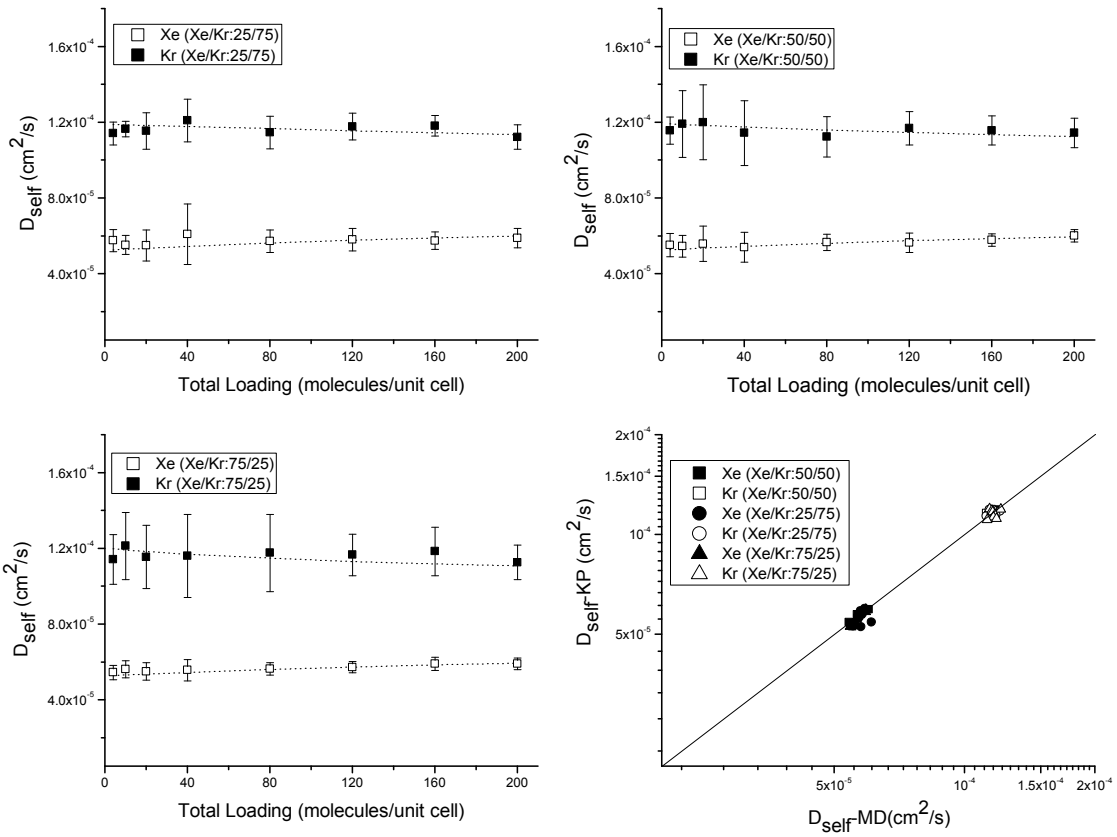

Figure 5.7: The predictions of KP correlation (dotted lines) and the results of mixture MD simulations (symbols) for self-diffusion coefficients of a)Xe/Kr:25/75 b)Xe/Kr:50/50 c)Xe/Kr:75/25 mixtures in IRMOF-1. d)Comparison of theory and simulations for mixture self-diffusivities at all loadings and compositions.

The deviations between KP correlation and MD simulations can be also discussed in terms of binary-exchange diffusivities. According to Equation 4.11, the ratio of binary exchange diffusivities ($Đ_{ij}/Đ_{ji}$) is equal to the ratio of saturation loadings of pure components ($\Theta_{i,sat}/\Theta_{j,sat}$) at all mixture compositions. For example, the single component saturation loadings of Xe and Kr in ZIF-2 were calculated as 25.3 and 28.6 molecules/unit cell at room temperature, respectively. Since these values are close to each other, the binary exchange-diffusivities, $Đ_{ij}$ and $Đ_{ji}$, are also similar. For equimolar mixtures, getting similar binary-exchange diffusivity values is reasonable, which is also supported by the accurate predictions of KP. The KP correlation assumes that the rate of filling a Xe vacancy by a Kr atom is almost equal to the rate of filling a Kr vacancy by a Xe atom. However, this is not a good assumption for mixtures where one species is dominant in the mixture such as Xe/Kr:75/25. Therefore, less accurate predictions are expected from the KP correlations for this composition. Our results also showed that the KP predictions are generally better for Xe/Kr mixtures compared to Xe/Ar mixtures and this can be attributed to the fast diffusion of Ar which is more affected by the correlation effects as we discussed above.

In Figure 5.9, we presented the results of a MOF, bioMOF-11, for which the agreement between theory and simulations is weak. The mixture self-diffusivities of both components show sharp decrease with increasing loading for all adsorbed compositions of Xe/Kr mixtures instead of slightly decreasing behavior proposed by KP correlation. The failure of KP correlation can be attributed to several reasons: The cavities of bioMOF-11 are 5.8 Å in diameter and its apertures between cavities are 5.2 Å in diameter, which indicates that the pores of this material are too narrow for mutual passage of Xe and Kr. Furthermore, the pore volume of bioMOF-11 (0.45 cm^3/g) [133] is low compared to other MOFs and saturation loadings of Xe, Kr and Ar are very low (see Table B.1 and B.2). Therefore, as the loading increases, steric hindrance effects become dominant and the self-diffusivities of

both gases decrease sharply. Since KP does not include steric hindrance and topology effects, it overestimates the self diffusivities of both components.

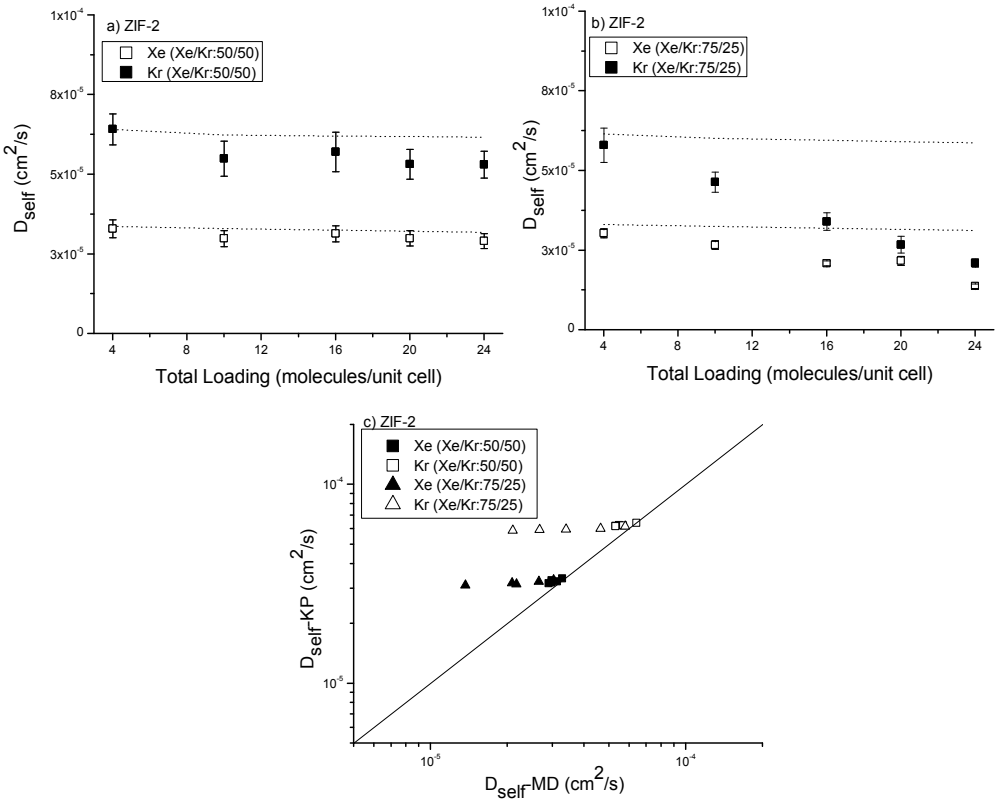

Figure 5.8: The predictions of KP correlation (dotted lines) and the results of mixture MD simulations (symbols) for self-diffusion coefficients of a)Xe/Kr:50/50 b)Xe/Kr:75/25 mixtures in ZIF-2. c)Comparison of theory and simulations for mixture self-diffusivities at all loadings and compositions.

We also presented the self-diffusivities of Xe/Kr mixtures in CuBTC because the diffusivity trends of gases in CuBTC are different from the ones in other MOFs. Figure

5.10 shows that self-diffusivities of Xe and Kr in CuBTC increase with loading and then approach a plateau at higher loadings. This is in contrast to the loading independent diffusion in IRMOF-1, ZIF-3, ZIF-10 and decreasing diffusivity trend observed in ZIF-2, $Zn(bdc)(ted)_{0.5}$, CPO-Ni, CPO-Co and bioMOF-11 (see Figures B.1 and B.2). The loading dependency of self-diffusivity in CuBTC can be explained by the Type III diffusion behavior proposed by Karger et al. [170] They suggested that some adsorption sites of the material have strong adsorption energies and these sites attract the molecules at the lowest loadings and prevent their diffusion. As the loading increases, these strong binding sites becomes occupied and other less-strong adsorption sites are filled by adsorbates which lead to an increase in the self-diffusivity. The self-diffusivity becomes constant as the loading further increases because every strong adsorption site is filled at high loadings. Figure 5.10 shows that KP captures the increasing trend of mixture diffusivities at low loadings qualitatively but do not make very accurate predictions quantitatively. This is an expected result because it is well known that KP correlation does not work accurately for energetically heterogeneous materials [171-172]. It is important to note that KP was also reported to be inaccurate for predicting mixture diffusion of CO_2/H_2 in CuBTC [119] and IAST was reported to be less accurate for Xe/Kr and CO_2/H_2 adsorption in CuBTC [74, 173].

One conclusion from the results we had so far is that KP correlation makes accurate predictions especially at low loadings although it may not be accurate at high loadings. At zero loading, the single component self-diffusivity is equal to the corrected diffusivity since there is no adsorbate-adsorbate interaction. At low loadings, the mixture self-diffusivity approaches to single component self- and corrected diffusivities $D_{ielf,i}^{single}(\theta \to 0) \cong Đ_{o,i}\ (\theta \to 0) \cong D_{self,i}^{mixture}(\theta_i \to 0, \theta_j \to 0)$ (see Equations 4.10 and 4.12). Therefore, KP makes accurate predictions at low loadings for mixture self-diffusivities by using the single component self- and corrected diffusivities. As the loading increases,

adsorbate-adsorbate interactions become important and predictions of KP get less accurate. If the mixture self-diffusivities show similar trend to the single component self-diffusivities, a high accuracy is expected from the KP correlation. In order to examine this, we computed the ratio of pure component self-diffusivity to the mixture self-diffusivity ($D_{self,i}^{single} / D_{ielf,i}^{mixture}$) for each component in Xe/Kr and Xe/Ar as a function of total loading using MD simulations. If this ratio is around one that means mixture self-diffusivities do not deviate from the single component diffusivities and the KP correlation makes accurate estimates for mixture diffusivities using single component data. Figure 5.11 represents that this ratio is close to one for equimolar adsorbed composition of Xe/Kr mixtures in all MOFs except bioMOF-11 and we already showed that KP correlation makes accurate estimates for all MOFs except bioMOF-11 if the composition is equimolar. Deviation from one was observed for Xe/Kr:75/25 mixtures and become more observable for bioMOF-11, ZIF-2 and Zn(bdc)(ted)$_{0.5}$, the materials for which KP makes less accurate predictions for non-diagonal compositions.

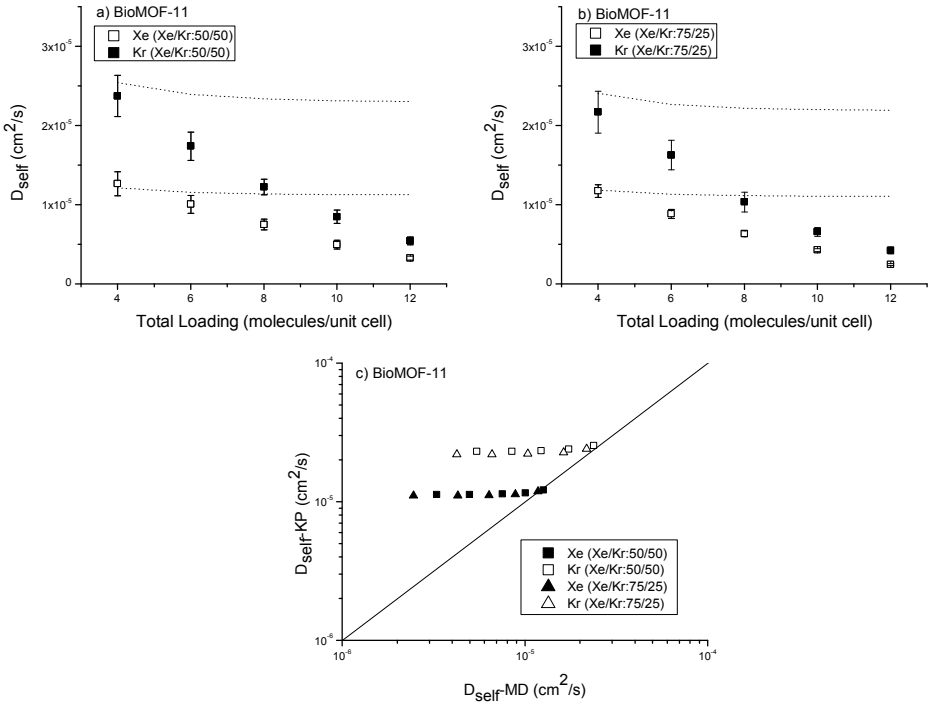

Figure 5.9: The predictions of KP correlation (dotted lines) and the results of mixture MD simulations (symbols) for self-diffusion coefficients of a)Xe/Kr:50/50 b)Xe/Kr:75/25 mixtures in bioMOF-11. c) Comparison of theory and simulations for mixture self-diffusivities at all loadings and compositions.

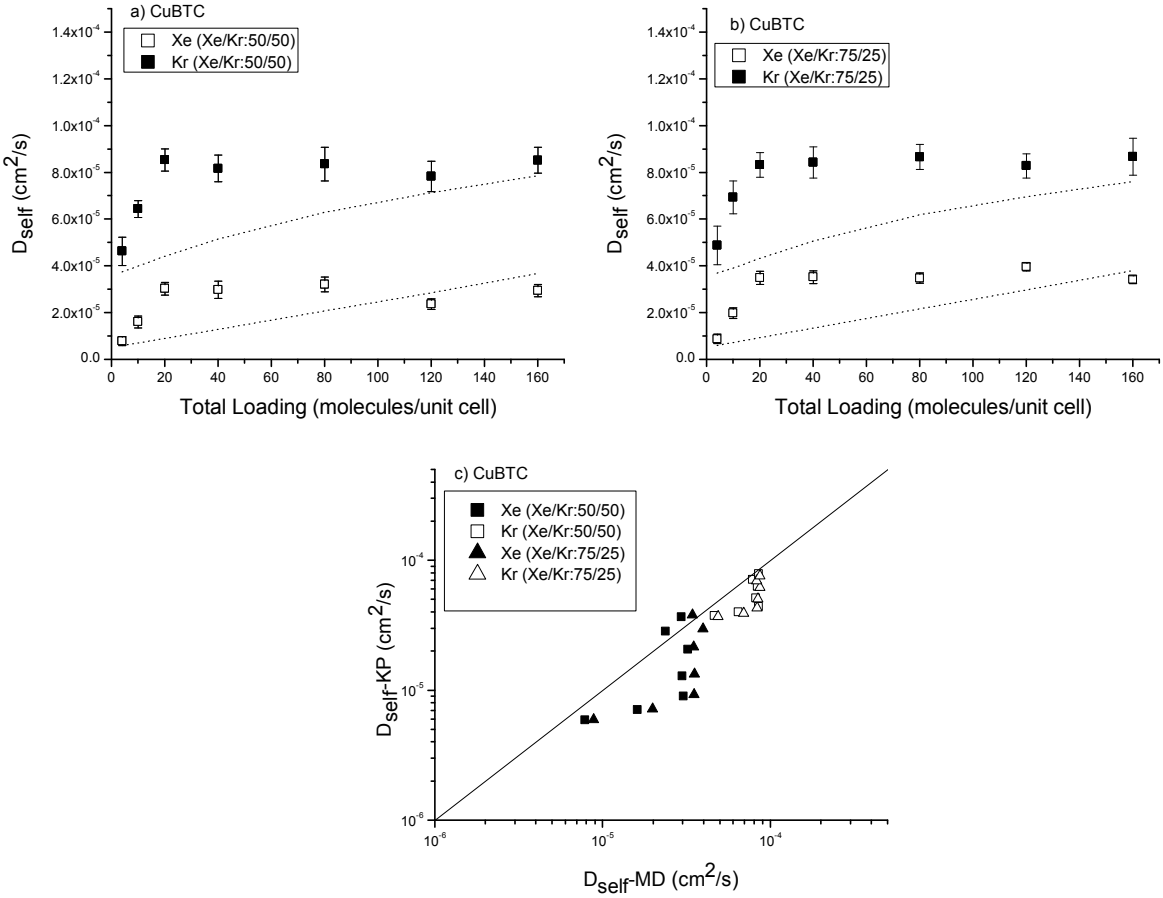

Figure 5.10: The predictions of KP correlation (dotted lines) and the results of mixture MD simulations (symbols) for self-diffusion coefficients of a)Xe/Kr:50/50 b)Xe/Kr:75/25 mixtures in CuBTC. c)Comparison of theory and simulations for mixture self-diffusivities at all loadings and compositions.

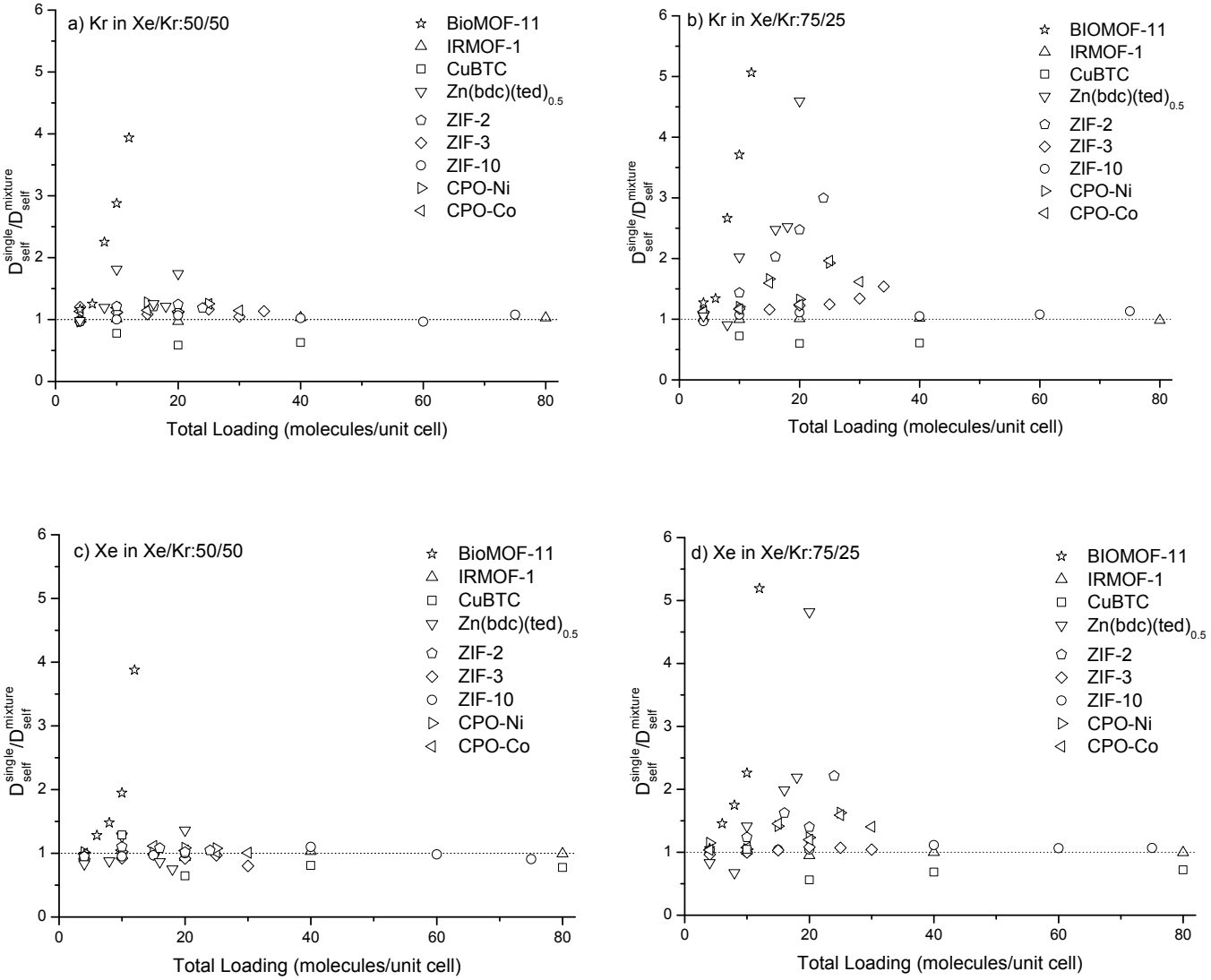

Figure 5.11: The ratio of single component self-diffusivity to the mixture self-diffusivity for a)Kr in Xe/Kr:50/50 b)Kr in Xe/Kr:75/25 c)Xe in Xe/Kr:50/50 d)Xe in Xe/Kr:75/25 in all MOFs.

We also examined the effect of composition on $D_{self,i}^{single} / D_{self,i}^{mixture}$ using the data shown in Figure 5.11. For example, the maximum value of $D_{self,i}^{single} / D_{self,i}^{mixture}$ for Kr in bioMOF-11 is 3.94 at Xe/Kr:50/50 mixture. This value increases up to 5.06 for Xe/Kr:75/25 because the mixture self-diffusivity of Kr decreases as the number of slow Xe atoms increases in the mixture. Similarly, the maximum value of $D_{self,i}^{single} / D_{self,i}^{mixture}$ for Xe in bioMOF-11 is 5.19 at Xe/Kr:75/25 and this value decreases to 3.87 for Xe/Kr:50/50 mixture. As the amount of Kr increases in the mixture, Kr atoms fasten the slow Xe atoms, the self-diffusivity of Xe atoms increases and the value of $D_{self,i}^{single} / D_{self,i}^{mixture}$ decreases. Figure 5.12 shows $D_{self,i}^{single} / D_{self,i}^{mixture}$ values for Xe/Ar mixtures. Similar to the Xe/Kr case, the deviation of the ratio from one is less for equimolar gas mixtures. If we compare Figure 5.11 and 5.12, we can see that deviation of the ratio for Ar is higher than the one for Kr in the mixtures where adsorbed composition of Xe is 75%. For example, at a total loading of 18 molecules/unit cell for Zn(bdc)(ted)$_{0.5}$, the value of ratio is 2.53 and 3.68 for Kr and Ar, respectively. This observation also supports the idea of fast diffusing component (Ar) is much more affected from the correlation effects. These results suggest that one can predict whether the KP correlation will give accurate estimates or not by computing $D_{self,i}^{single} / D_{self,i}^{mixture}$ using MD simulations at a few loadings prior to doing extensive calculations. If the value of $D_{self,i}^{single} / D_{self,i}^{mixture}$ is around 1, then the KP correlation can be used to accurately predict the mixture self-diffusivities of the components at a wide range of loadings for that material. It is important to note that the adsorbed loadings considered in Figures 5.5-5.6 are different for each MOF. Since saturation loadings of IRMOF-1, ZIF-10 and CuBTC are higher than the other MOFs, pure component and mixture-self diffusivities were examined up to higher loadings for these MOF compared to others.

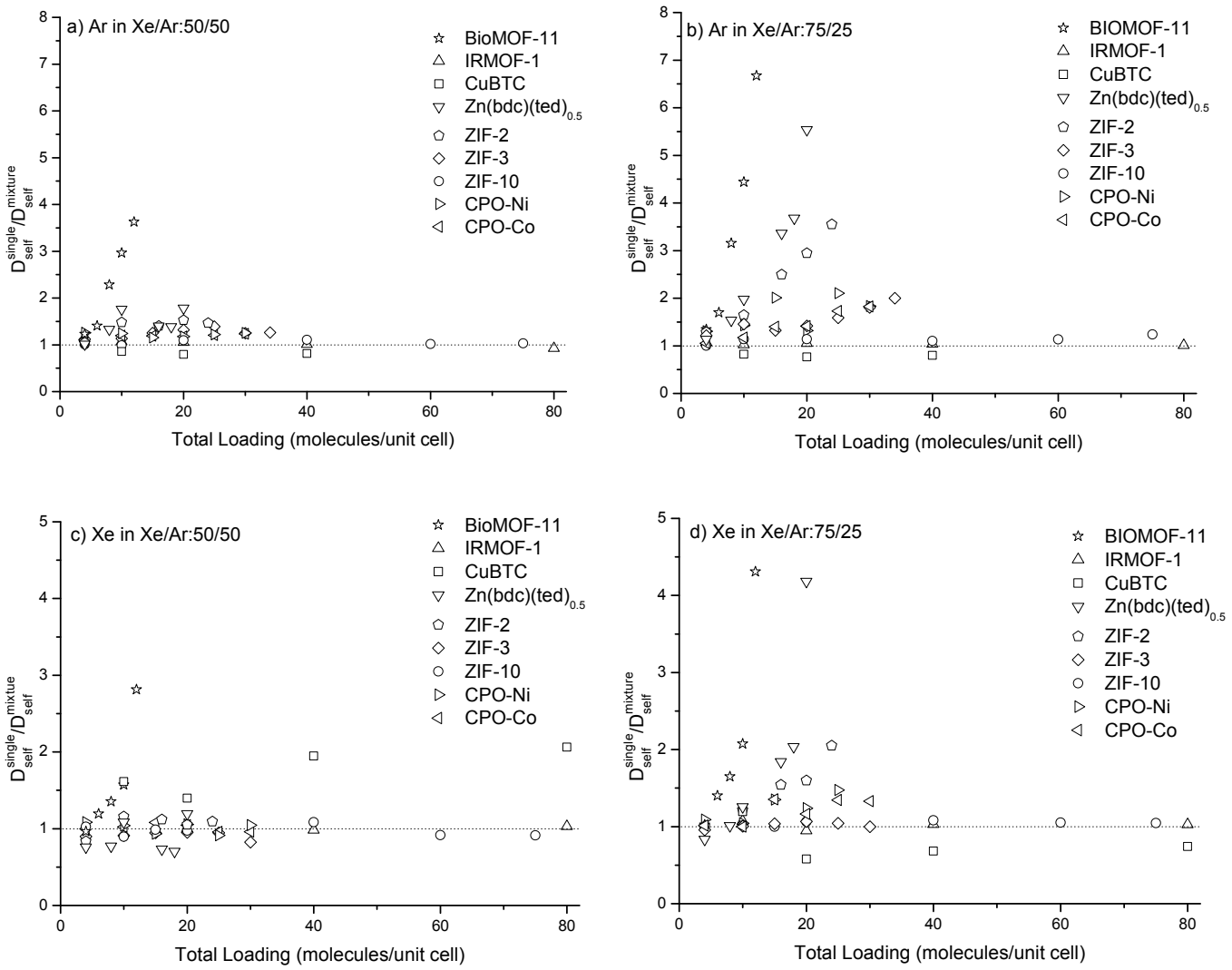

Figure 5.12: The ratio of single component self-diffusivity to the mixture self-diffusivity of a)Ar in Xe/Ar:50/50 b)Ar in Xe/Ar:75/25 c)Xe in Xe/Ar:50/50 d)Xe in Xe/Ar:75/25 in all MOFs.

After testing the accuracy of a theoretical correlation for predicting mixture self-diffusivities, we now turn to the theoretical method that can predict the mixture adsorption based on single component adsorption data. Figure 5.13 shows adsorption selectivity and working capacity of MOFs calculated at 10 bar and 298 K using mixture GCMC simulations and IAST. The results showed that IAST predictions for adsorption of Xe/Kr and Xe/Ar mixtures are good for all materials. Small deviations were observed in predicting working capacity due to the accumulation of the errors in adsorbed concentration values at 1 bar and 10 bar. The largest deviation between the mixture GCMC simulations and IAST was observed for the Xe/Ar adsorption selectivity of bioMOF-11. IAST overestimates Ar adsorption and underestimates Xe adsorption in bioMOF-11 therefore its selectivity prediction is less than the one calculated from mixture GCMC. This figure shows that using IAST instead of computationally demanding mixture GCMC simulations can give accurate answers for evaluating the adsorption-based separation performance of MOFs. Previous research showed that NaX zeolite has an adsorption selectivity of ~6 for Xe over Kr, [74, 174], NaA zeolite has a Xe selectivity of 4-4.5 (20-25) from an equimolar Xe/Kr (Xe/Ar) mixture at 300 K between 1 and 10 bar [47]. Except IRMOF-1 and ZIF-10 all the MOFs considered in this work show higher Xe selectivity than NaA and NaX zeolites.

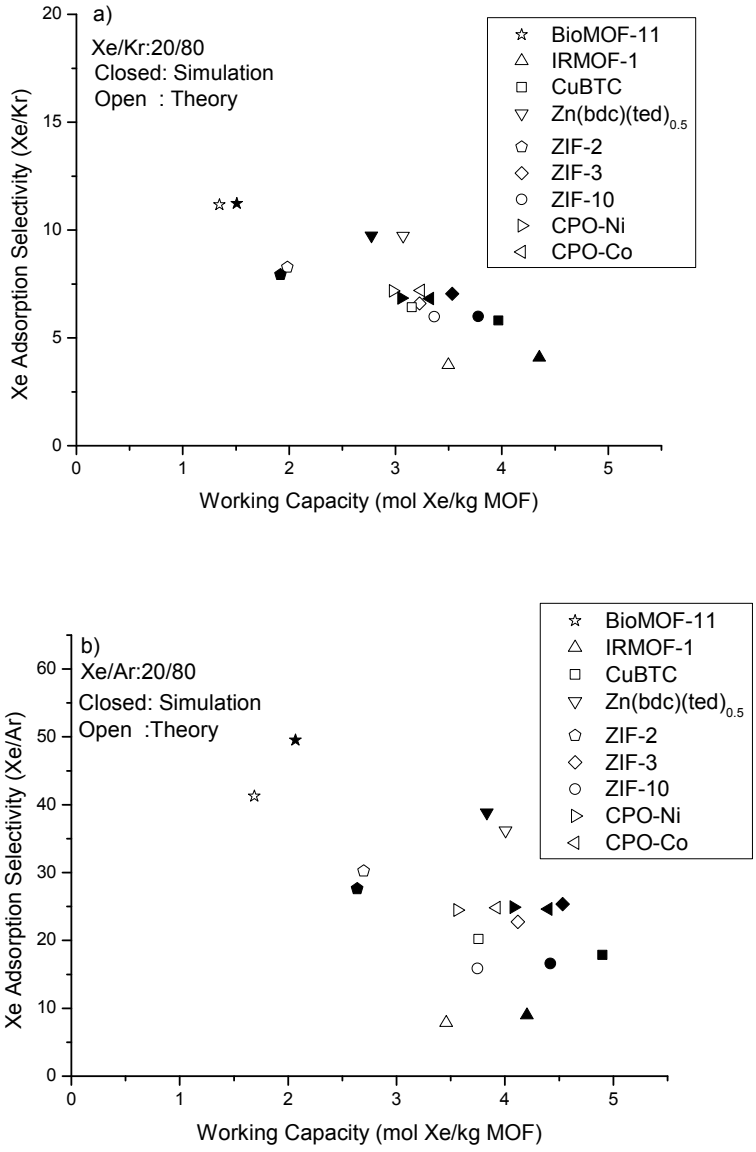

Figure 5.13: Adsorption selectivity and working capacity of MOFs calculated from GCMC simulations and predicted by IAST for a)Xe/Kr and b)Xe/Ar separations at 10 bar, 298 K.

Once mixture self-diffusivities are predicted using KP and mixture adsorption isotherms are predicted using IAST, the permeation selectivity and permeability of MOFs for membrane-based separation of Xe/Kr and Xe/Ar mixtures can be estimated using Equations 4.15 and 4.4, respectively. Figure 5.14 compares the Xe permeability and permeation selectivity calculated from mixture simulations (GCMC and MD) with the values predicted from theoretical correlations (KP and IAST) for Xe/Kr and Xe/Ar mixtures. Since permeation selectivity is the product of adsorption selectivity and diffusion selectivity, the differences between theory and simulations is due to the deviation of IAST and/or KP. Figure 5.13 showed that adsorption selectivities predicted from IAST are in a good agreement with the ones directly calculated from mixture GCMC, therefore differences observed in permeation selectivity in Figure 5.14 must be due to the deviation of KP. For example, Xe/Kr:20/80 bulk mixture in bioMOF-11 corresponds to an adsorbed mixture of Xe/Kr:73/27.

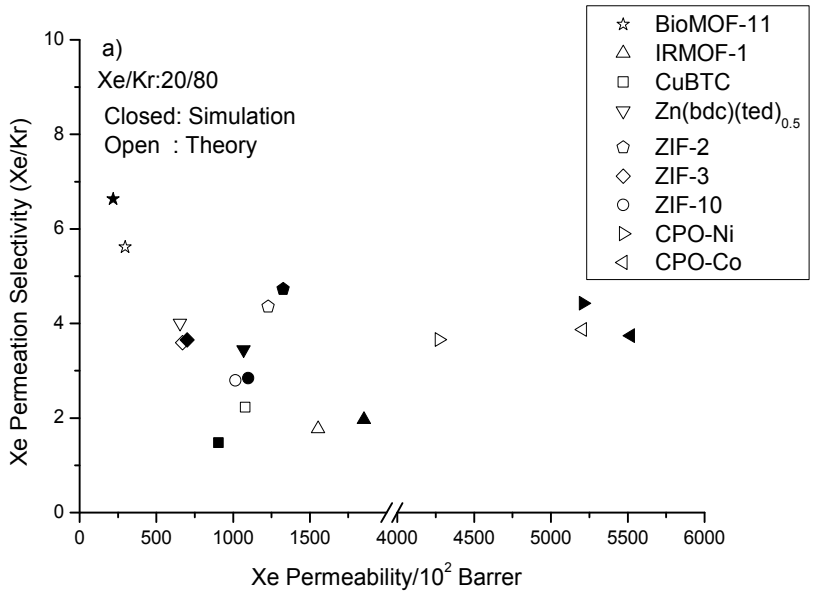

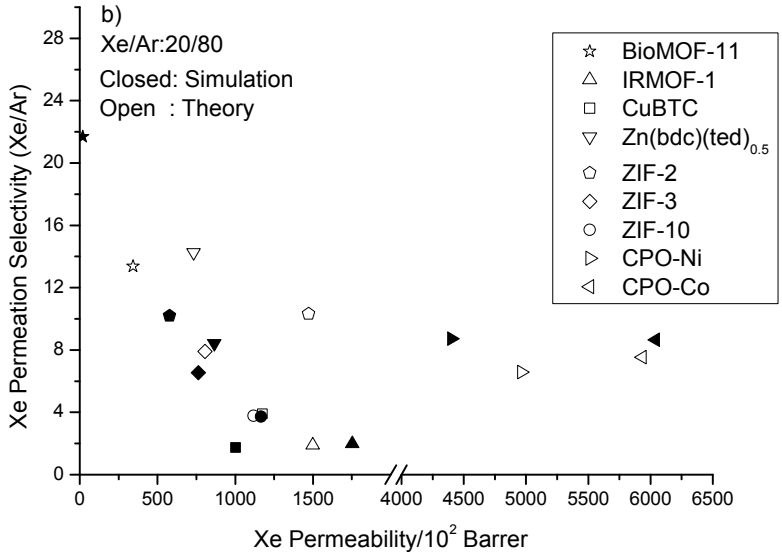

Figure 5.14: Permeation selectivity and gas permeability of MOFs calculated from simulations (GCMC and MD) and predicted by theory (IAST and KP) for a)Xe/Kr and b)Xe/Ar separations at 10 bar, 298 K.

We showed that KP overestimates both Xe and Kr self-diffusivities compared to EMD at an adsorbed composition of Xe/Kr:75/25 in Figure 5.9, and overestimation for Kr was higher than Xe. Due to this reason, permeation selectivity calculated from theory is less than the value calculated from simulations. One interesting case from Figure 5.14 is the Xe/Ar separation performance of ZIF-2. In this case, theory overestimates Xe permeability of ZIF-2 in Xe/Ar separations but predicts the Xe selectivity well compared to the simulations. This is due to the overestimation of individual diffusion coefficients by the KP correlation. The KP correlation overestimates the mixture self-diffusivities of Xe and Ar ($D_{self,Xe}^{mixture}$ and $D_{self,Ar}^{mixture}$) in the same amount and therefore predicts almost the same diffusion

selectivity ($D_{self,Xe}^{mixture} / D_{self,Ar}^{mixture}$) with the mixture MD simulations. Since the estimates of IAST agree well with the GCMC results, the Xe permeations selectivity calculated by the simulations and predicted by the theories are almost same although the Xe permeability was overestimated (see Table B.2).

In summary, Figure 5.14 indicates that using theoretical correlations to evaluate the performance of MOFs for permeation-based separation of noble gas mixtures for prescreening purposes is appropriate. The predictions of theory agree with the results of simulations about the materials' performance in separation applications. For example, both theory and simulations suggest that CPOs are good candidates in adsorption-based and membrane-based separation of noble gases due to their high gas permeability and good selectivity. The example that we discussed above for ZIF-2 indicates that diffusion selectivity derived from theory and the one obtained from simulations can be very similar, but this does not guarantee that the individual diffusion coefficients are accurately predicted by the KP correlation. Because of this reason, it is better to compare the adsorbed amounts and self-diffusivities of each component obtained from theory and simulations to make a better judgment about the accuracy of theoretical correlations. With this aim, we compared the results of simulations and predictions of theories for the adsorbed concentrations and self-diffusivities of each component in Xe/Kr and Xe/Ar mixtures at 10 bar, 298 K in Figure B.3. The adsorbed amounts predicted by IAST perfectly agree with the ones calculated from GCMC in Figure B.3a-b. On the other hand, deviations between KP correlation and MD simulations are observed for bioMOF-11 and $Zn(bdc)(ted)_{0.5}$ in Figure B.3c-d. For instance, KP correlation underestimates (overestimates) both Xe and Kr mixture self-diffusivities in $Zn(bdc)(ted)_{0.5}$ (bioMOF-11) by nearly the same ratio, therefore Xe permeation selectivities obtained by simulations and predicted by theory are similar to each other for this MOF even though the self-diffusivities are not.

We finally compared the ideal selectivity of MOFs for Xe/Kr and Xe/Ar separations with the mixture selectivities calculated from theoretical correlations and simulations. Table 5.2 and Table 5.3 show that ideal selectivity calculated using single component data is significantly different than the mixture selectivity for Xe/Kr and Xe/Ar separations.

Table 5.2: Comparison of permeation selectivity and ideal selectivity for Xe from Xe/Kr mixture at 10 bar and 298 K.

MOFs	$S_{permeation,theory}$	$S_{permeation,simulation}$	$S_{ideal\ with\ composition\ effect}$	S_{ideal}
BioMOF-11	5.62	6.63	1.99	0.49
IRMOF-1	1.77	1.97	1.78	1.30
ZIF-2	4.35	4.73	2.07	0.50
ZIF-3	3.59	3.65	2.31	0.67
ZIF-10	2.79	2.84	2.52	0.83
$Zn(bdc)(ted)_{0.5}$	4.01	3.44	1.45	0.51
CPO-Co	3.87	3.74	2.93	0.71
CPO-Ni	3.66	4.42	2.44	0.73
CuBTC	2.23	1.48	1.49	0.78

Table 5.3: Comparison of permeation selectivity and ideal selectivity for Xe from Xe/Ar mixture at 10 bar and 298 K.

MOFs	$S_{permeation,theory}$	$S_{permeation,simulation}$	$S_{ideal\ with\ composition\ effect}$	S_{ideal}
BioMOF-11	13.37	21.69	2.16	0.61
IRMOF-1	1.90	1.99	2.00	1.31
ZIF-2	10.31	10.19	2.22	0.53
ZIF-3	7.91	6.54	2.06	0.58
ZIF-10	3.77	3.72	2.88	0.94
$Zn(bdc)(ted)_{0.5}$	14.26	8.43	1.31	0.41
CPO-Co	7.54	8.64	3.68	0.84
CPO-Ni	6.59	8.72	2.91	0.76
CuBTC	3.90	1.74	1.36	0.71

The ideal selectivity that considers the composition effect is slightly higher but its predictions are not close to the mixture selectivity since the competition between adsorbates is not considered. For example, both theory and simulations suggest that ZIF-2 is a good candidate for separation of Xe/Ar mixtures due to its high Xe selectivity (predicted as 10.3 by theory and computed as 10.2 by simulations) compared to other MOFs. However, ideal selectivity assumes that ZIF-2 is only weakly Ar selective (1.89) under the same conditions. This result underlines the importance of evaluating a material's separation performance based on mixed gas feeds rather than the single gas feeds. We can conclude that if the single component adsorption and diffusion data is available, using KP and IAST to estimate the mixture selectivity is much more accurate than calculating the ideal selectivity in order to evaluate the performance of a material in separation processes. More details of this part can also found in our recently published paper [175].

Chapter 6

CONCLUSIONS and FUTURE PROSPECTS

In this thesis, potential of MOFs for diffusion, adsorption and separation of noble gases were investigated using molecular simulations and theoretical correlations. Adsorption and diffusion of Xe, Kr and Ar and their binary mixtures were predicted using grand canonical Monte Carlo (GCMC) and equilibrium molecular dynamics (EMD) simulations, respectively. Ten representative MOFs that have different metal sites, organic linkers, pore size, shape, pore volume and chemical structures were selected to examine their Xe adsorption selectivity, working capacity, permeation selectivity and permeability.

In the first part of this thesis, adsorption simulations of noble gases in MOFs were compared with the available experimental data. There was a good agreement between the results of our molecular simulations and experimental adsorption isotherms. Comparing the single component adsorption isotherms of Xe, Kr and Ar in MOFs and several zeolites showed that MOFs have higher noble gas adsorption capacity than most zeolites. Single component adsorption isotherms of noble gases in MOFs showed that at low pressures, Xe adsorption is higher than Kr (Ar) due to energetic effects. However, as pressure increases, Kr (Ar) adsorption gets higher than Xe adsorption, as a result of entropic effects. According to binary mixture adsorption results, MOFs having small pores (bioMOF-11, $Zn(bdc)(ted)_{0.5}$, ZIF-1, ZIF-2, CuBTC) show higher Xe adsorption selectivities than MOFs having large pores (IRMOF-1, CPO-27-Ni and CPO-Co), which is attributed to the

stronger confinement of Xe atoms in smaller pores that leads to stronger interactions between framework and Xe atoms.

Binary mixture EMD results show that Xe self-diffusivity is lower than Kr (Ar) diffusivity in Xe/Kr (Xe/Ar) mixtures in all MOFs. The reason is the strong adsorption of Xe, which slows its diffusion through the pores. Both high adsorption selectivity and high working capacity are desired for efficient gas separation. However, a trade-off between adsorption selectivity and working capacity was seen in all MOFs for noble gas separations. Among studied MOFs, $Zn(bdc)(ted)_{0.5}$ gives the best adsorption selectivity and working capacity combination.

Xe permeabilities and permeation selectivities were compared for both Xe/Kr and Xe/Ar mixtures in all MOFs. High adsorption selectivity for Xe was compensated by low diffusion selectivity for Xe and this led to low Xe permeation selectivities in all MOFs. A promising membrane should have both high Xe permeability and high Xe permeation selectivity. The results showed CPO materials have higher Xe permeability than the other MOFs since CPOs have higher Xe adsorption and faster Xe diffusion in their pores. Xe permeabilities of MOFs considered in this thesis were found to be higher than several nanoporous materials due to high porosity of MOFs.

In the second part of the thesis, adsorption and diffusion of Xe/Kr and Xe/Ar mixtures were predicted using theoretical correlations. Mixture self diffusivities were predicted by Krishna-Paschek (KP) correlations using single component self diffusivity data and compared with the results of EMD simulations. Three different mixture compositions (25/75, 50/50 and 75/25) were examined for Xe/Kr and Xe/Ar mixtures. According to the results, MOFs were categorized into three groups: MOFs for which correlations show very good agreement with the simulations (IRMOF-1, ZIF-3 and ZIF-10), MOFs for which correlations show reasonable agreement with the simulations (ZIF-2, $Zn(bdc)(ted)_{0.5}$, CPO-Ni and CPO-Co) and finally MOFs for which KP correlations do not capture mixture

diffusivity trend (bioMOF-11 and CuBTC). Good agreement between KP correlations and EMD simulations in IRMOF-1, ZIF-3 and ZIF-10 is attributed to the larger cavity diameters and larger pore volumes of these materials. Due to this high free volume, adsorbates behave like they are in the single component diffusion case. This shows that correlation effects between different adsorbates are negligible in these MOFs, which results in a high accuracy of KP.

For ZIF-2, $Zn(bdc)(ted)_{0.5}$, CPO-Ni and CPO-Co, KP correlations capture mixture self diffusivity in equimolar mixture, but make less accurate predictions if one component is dominated in the adsorbed mixture. For bioMOF-11 and CuBTC, the agreement between theory and simulations is weak. In bioMOF-11, cavity diameters and apertures between cavities are small which indicates that these pores are too narrow for mutual passage of Xe and Kr (Ar). Therefore as loading increases steric hindrance effects become dominant and the self diffusivities of gases decrease sharply. Steric hindrance effects and material topologies are not considered in the KP correlations, therefore KP correlation overestimates the mixture self diffusivity of gases. The weak predictions for CuBTC were attributed to its heterogeneous adsorption sites which are also not considered in KP correlations.

The results showed that at low loadings KP make accurate predictions for all MOFs and for all mixture compositions. As loading increases adsorbate-adsorbate interactions become important and predictions of KP get less accurate. Results showed that if the mixture self diffusivities show similar trend to the single component self diffusivities than KP gives accurate predictions. It was also found that KP predictions are generally better for Xe/Kr mixtures rather than Xe/Ar mixtures. This was attributed to the fast diffusion of Ar which is more affected by the correlation effects.

Mixture adsorptions were predicted by applying IAST and results were compared with the GCMC. The results showed that IAST predictions for adsorption of Xe/Kr and Xe/Ar

mixtures are good for all materials. Adsorption selectivity and working capacity calculated by both GCMC simulations and IAST gave similar results.

Xe Permeability and permeation selectivity were calculated using both simulations (GCMC and EMD) and theoretical correlations (IAST and KP) for Xe/Kr and Xe/Ar mixtures and results were compared. The reason of deviations between simulations and theoretical correlations in Xe permeation selectivity was attributed to the weak predictions of KP correlations. It was concluded that presence of heterogeneous adsorption sites, existence of different pore sizes, shapes, loading, and composition of the adsorbates may play important role in some cases although they are not considered by theoretical correlations. When all the results were taking into account, it was found that for prescreening purposes using theoretical correlations to evaluate the performance of MOFs for permeation-based separation of noble gas mixtures is appropriate. By using these correlations, it is possible to rapidly examine a large range of potential operating conditions (pressure, temperature, composition) for chemical mixtures as soon as information on each species in the MOF of interest is known.

Finally, ideal selectivity of MOFs for Xe/Kr and Xe/Ar separations were compared with the mixture selectivities calculated from theoretical correlations and simulations. According to the results, using KP and IAST to estimate the mixture selectivity is much more accurate than calculating the ideal selectivity based on single component adsorption and diffusion data in order to evaluate the performance of a material in separation processes.

As a conclusion, studies on noble gas separation by nanoporous materials in the literature are very limited which is the main motivation of this thesis. This thesis can be considered as the first study in the literature which predicts the separation performance of MOFs as membranes and adsorbents. The results of this thesis and the approaches

presented in this thesis will be helpful for design and development of new MOF adsorbents and membranes for noble gas separations.

BIBLIOGRAPHY

[1] C.F. Poole, M. Cooke, and I.D. Wilson, Encyclopedia of Separation Science, Academic Press, (2000).
[2] C.J. Geankoplis, Transport Processes and Separation Process Principles, Prentice Hall, (2003).
[3] W.R. Vieth, Diffusion in and through Polymers: Principles and Applications, Hanser Publishers, (1991).
[4] F.M. Dautzenberg and M. Mukherjee, Process Intensification Using Multifunctional Reactors, Chemical Engineering Science, 56 (2001), 251-267.
[5] P. Bernardo, E. Drioli, and G. Golemme, Membrane Gas Separation: A Review/State of the Art, Industrial & Engineering Chemistry Research, 48 (2009), 4638-4663.
[6] R.W. Baker, Future Directions of Membrane Gas Separation Technology, Industrial & Engineering Chemistry Research, 41 (2002), 1393-1411.
[7] W.J. Koros and R. Mahajan, Pushing the Limits on Possibilities for Large Scale Gas Separation: Which Strategies?, Journal of Membrane Science, 175 (2000), 181-196.
[8] B.D. Freeman, Basis of Permeability/Selectivity Tradeoff Relations in Polymeric Gas Separation Membranes, Macromolecules, 32 (1999), 375-380.
[9] L.M. Robeson, Correlation of Separation Factor versus Permeability for Polymeric Membranes, Journal of Membrane Science, 62 (1991), 165-185.
[10] S. Alexander Stern, Polymers for Gas Separations: The Next Decade, Journal of Membrane Science, 94 (1994), 1-65.
[11] I.M. Ward and D.W. Hadley, An Introduction to the Mechanical Properties of Solid Polymers, Wiley, (1993).
[12] Y. Yampolskii, Polymeric Gas Separation Membranes, Macromolecules, 45 (2012), 3298-3311.
[13] G. Strobl, The Physics of Polymers: Concepts for Understanding Their Structures and Behavior, Springer, (1997).
[14] J.L. Barrat, J. Baschnagel, and A. Lyulin, Molecular Dynamics Simulations of Glassy Polymers, Soft Matter, 6 (2010), 3430-3446.
[15] R.N. Haward and R.J. Young, The Physics of Glassy Polymers, Chapman & Hall, (1997).
[16] P. Shao and R.Y.M. Huang, Polymeric Membrane Pervaporation, Journal of Membrane Science, 287 (2007), 162-179.
[17] J. Ferry, Viscoelastic Properties of Polymers, Wiley, (1980).
[18] L.M. Robeson, W.F. Burgoyne, M. Langsam et al., High-Performance Polymers for Membrane Separation, Polymer, 35 (1994), 4970-4978.

[19] G. Maier, Gas Separation with Polymer Membranes, Angewandte Chemie-International Edition, 37 (1998), 2961-2974.
[20] M. Moaddeb and W.J. Koros, Gas Transport Properties of Thin Polymeric Membranes in the Presence of Silicon dioxide Particles, Journal of Membrane Science, 125 (1997), 143-163.
[21] A.F. Ismail and L.I.B. David, A Review on The Latest Development of Carbon Membranes for Gas Separation, Journal of Membrane Science, 193 (2001), 1-18.
[22] K. Keizer and H. Verweij, Progress in Inorganic Membranes, Chemtech, 26 (1996), 37-41.
[23] R. Soria, Overview on Industrial Membranes, Catalysis Today, 25 (1995), 285-290.
[24] J. Hayashi, H. Mizuta, M. Yamamoto et al., Pore Size Control of Carbonized BPDA-pp'ODA Polyimide Membrane by Chemical Vapor Deposition of Carbon, Journal of Membrane Science, 124 (1997), 243-251.
[25] T.C. Bowen, R.D. Noble, and J.L. Falconer, Fundamentals and Applications of Pervaporation Through Zeolite Membranes, Journal of Membrane Science, 245 (2004), 1-33.
[26] A.B. Fuertes and T.A. Centeno, Preparation of Supported Carbon Molecular Sieve Membranes, Carbon, 37 (1999), 679-684.
[27] C.H. Liang, G.Y. Sha, and S.C. Guo, Carbon Membrane for Gas Separation Derived from Coal Tar Pitch, Carbon, 37 (1999), 1391-1397.
[28] A.B. Fuertes, Adsorption-Selective Carbon Membrane for Gas Separation, Journal of Membrane Science, 177 (2000), 9-16.
[29] B. Moulton and M.J. Zaworotko, From Molecules to Crystal Engineering: Supramolecular Isomerism and Polymorphism in Network Solids, Chemical Reviews, 101 (2001), 1629-1658.
[30] M. Eddaoudi, H. Li, and O.M. Yaghi, Highly Porous and Stable Metal−Organic Frameworks: Structure Design and Sorption Properties, Journal of the American Chemical Society, 122 (2000), 1391-1397.
[31] B.F. Hoskins and R. Robson, Infinite Polymeric Frameworks Consisting of 3 Dimensionally Linked Rod-like Segments, Journal of the American Chemical Society, 111 (1989), 5962-5964.
[32] D. Venkataraman, G.B. Gardner, S. Lee et al., Zeolite-like Behavior of A Coordination Network, Journal of the American Chemical Society, 117 (1995), 11600-11601.
[33] O.M. Yaghi, G.M. Li, and H.L. Li, Selective Binding and Removal of Guests in a Microporous Metal-Organic Framework, Nature, 378 (1995), 703-706.
[34] S. Subramanian and M.J. Zaworotko, Porous Solids By Design: A Single Framework Octahedral Coordination Polymer with Large Square Channels, Angewandte Chemie-International Edition, 34 (1995), 2127-2129.

[35] S.T. Meek, J.A. Greathouse, and M.D. Allendorf, Metal-Organic Frameworks: A Rapidly Growing Class of Versatile Nanoporous Materials, Advanced Materials, 23 (2011), 249-267.
[36] R.B. Getman, Y.S. Bae, C.E. Wilmer et al., Review and Analysis of Molecular Simulations of Methane, Hydrogen, and Acetylene Storage in Metal-Organic Frameworks, Chemical Reviews, 112 (2012), 703-723.
[37] S. Keskin, in Molecular Dynamics-Theoretical Developments and Applications in Nanotechnology and Energy, L. Wang, Editor, InTech, (2012).
[38] A. Battisti, S. Taioli, and G. Garberoglio, Zeolitic Imidazolate Frameworks for Separation of Binary Mixtures of CO_2, CH_4, N_2 and H_2: A Computer Simulation Investigation, Microporous and Mesoporous Materials, 143 (2011), 46-53.
[39] R. Babarao and J. Jiang, Diffusion and Separation of CO_2 and CH_4 in Silicalite, C_{168} Schwarzite, and IRMOF-1: A Comparative Study from Molecular Dynamics Simulation, Langmuir, 24 (2008), 5474-5484.
[40] Y. Liu, D. Liu, Q. Yang et al., Comparative Study of Separation Performance of COFs and MOFs for $CH_4/CO_2/H_2$ Mixtures, Industrial & Engineering Chemistry Research, 49 (2010), 2902-2906.
[41] I. Asimov, The Noble Gases, Basic Books, (1966).
[42] M. Halka and B. Nordstrom, Halogens and Noble Gases, Facts On File, (2010).
[43] F.G. Kerry, Industrial Gas Handbook : Gas Separation and Purification, CRC Press, (2007).
[44] A.L. Myers and J.M. Prausnitz, Thermodynamics of Mixed-Gas Adsorption, AIChE Journal, 11 (1965), 121-127.
[45] R. Krishna and D. Paschek, Self-Diffusivities in Multicomponent Mixtures in Zeolites, Physical Chemistry Chemical Physics, 4 (2002), 1891-1898.
[46] A.I. Skoulidas and D.S. Sholl, Molecular Dynamics Simulations of Self-Diffusivities, Corrected Diffusivities, and Transport Diffusivities of Light Gases in Four Silica Zeolites to Assess Influences of Pore Shape and Connectivity, Journal of Physical Chemistry A, 107 (2003), 10132-10141.
[47] C.J. Jameson, A.K. Jameson, and H.M. Lim, Competitive Adsorption of Xenon and Krypton in Zeolite NaA: Xe-129 Nuclear Magnetic Resonance Studies and Grand Canonical Monte Carlo Simulations, Journal of Chemical Physics, 107 (1997), 4364-4372.
[48] A.I. Skoulidas and D.S. Sholl, Transport Diffusivities of CH_4, CF_4, He, Ne, Ar, Xe, and SF_6 in Silicalite from Atomistic Simulations, The Journal of Physical Chemistry B, 106 (2002), 5058-5067.
[49] R.Q. Snurr and J. Karger, Molecular Simulations and NMR Measurements of Binary Diffusion in Zeolites, Journal of Physical Chemistry B, 101 (1997), 6469-6473.

[50] R. Krishna and J.M. van Baten, Using Molecular Simulations for Screening of Zeolites for Separation of CO_2/CH_4 Mixtures, Chemical Engineering Journal, 133 (2007), 121-131.

[51] S.E. Jee and D.S. Sholl, Carbon Dioxide and Methane Transport in DDR Zeolite: Insights from Molecular Simulations into Carbon Dioxide Separations in Small Pore Zeolites, Journal of the American Chemical Society, 131 (2009), 7896-7904.

[52] A. Goj, D.S. Sholl, E.D. Akten et al., Atomistic Simulations of CO_2 and N_2 Adsorption in Silica Zeolites: The Impact of Pore Size and Shape, Journal of Physical Chemistry B, 106 (2002), 8367-8375.

[53] E.J. Maginn, A.T. Bell, and D.N. Theodorou, Transport Diffusivity of Methane in Silicalite From Equilibrium and Nonequilibrium Simuations, Journal of Physical Chemistry, 97 (1993), 4173-4181.

[54] T. Duren, L. Sarkisov, O.M. Yaghi et al., Design of New Materials for Methane Storage, Langmuir, 20 (2004), 2683-2689.

[55] T. Duren and R.Q. Snurr, Assessment of Isoreticular Metal-Organic Frameworks for Adsorption Separations: A Molecular Simulation Study of Methane/n-butane Mixtures, Journal of Physical Chemistry B, 108 (2004), 15703-15708.

[56] D.H. Jung, D. Kim, T.B. Lee et al., Grand Canonical Monte Carlo Simulation Study on the Catenation Effect on Hydrogen Adsorption onto the Interpenetrating Metal−Organic Frameworks, The Journal of Physical Chemistry B, 110 (2006), 22987-22990.

[57] S.S. Han, S.H. Choi, and W.A. Goddard, Zeolitic Imidazolate Frameworks as H_2 Adsorbents: Ab Initio Based Grand Canonical Monte Carlo Simulation, Journal of Physical Chemistry C, 114 (2010), 12039-12047.

[58] R. Krishna and J.M. van Baten, Investigating the Potential of MgMOF-74 Membranes for CO_2 Capture, Journal of Membrane Science, 377 (2011), 249-260.

[59] R. Krishna and J.M. van Baten, In Silico Screening of Metal-Organic Frameworks in Separation Applications, Physical Chemistry Chemical Physics, 13 (2011), 10593-10616.

[60] R. Krishna and J.M. van Baten, In Silico Screening of Zeolite Membranes for CO_2 Capture, Journal of Membrane Science, 360 (2010), 323-333.

[61] Q. Yang, C. Xue, C. Zhong et al., Molecular Simulation of Separation of CO_2 From Flue Gases in CU-BTC Metal-Organic Framework, AIChE Journal, 53 (2007), 2832-2840.

[62] H. Guo, F. Shi, Z.-f. Ma et al., Molecular Simulation for Adsorption and Separation of CH_4/H_2 in Zeolitic Imidazolate Frameworks, The Journal of Physical Chemistry C, 114 (2010), 12158-12165.

[63] C. Zheng, D. Liu, Q. Yang et al., Computational Study on the Influences of Framework Charges on CO_2 Uptake in Metal−Organic Frameworks, Industrial & Engineering Chemistry Research, 48 (2009), 10479-10484.

[64] R. Babarao, J. Jiang, and S.I. Sandler, Molecular Simulations for Adsorptive Separation of CO_2/CH_4 Mixture in Metal-Exposed, Catenated, and Charged Metal−Organic Frameworks, Langmuir, 25 (2008), 5239-5247.

[65] R. Babarao and J. Jiang, Unprecedentedly High Selective Adsorption of Gas Mixtures in *rho* Zeolite-like Metal−Organic Framework: A Molecular Simulation Study, Journal of the American Chemical Society, 131 (2009), 11417-11425.

[66] E. Atci, I. Erucar, and S. Keskin, Adsorption and Transport of CH_4, CO_2, H_2 Mixtures in a Bio-MOF Material from Molecular Simulations, Journal of Physical Chemistry C, 115 (2011), 6833-6840.

[67] E. Atci and S. Keskin, Atomically Detailed Models for Transport of Gas Mixtures in ZIF Membranes and ZIF/Polymer Composite Membranes, Industrial & Engineering Chemistry Research, (2012).

[68] S. Keskin, Comparing Performance of CPO and IRMOF Membranes for Gas Separations Using Atomistic Models, Industrial & Engineering Chemistry Research, 49 (2010), 11689.

[69] S. Keskin, Atomistic Simulations for Adsorption, Diffusion, and Separation of Gas Mixtures in Zeolite Imidazolate Frameworks, The Journal of Physical Chemistry C, 115 (2010), 800-807.

[70] S. Keskin and D.S. Sholl, Assessment of a Metal−Organic Framework Membrane for Gas Separations Using Atomically Detailed Calculations: CO_2, CH_4, N_2, H_2 Mixtures in MOF-5, Industrial & Engineering Chemistry Research, 48 (2008), 914-922.

[71] S. Keskin, Adsorption, Diffusion, and Separation of CH_4/H_2 Mixtures in Covalent Organic Frameworks: Molecular Simulations and Theoretical Predictions, The Journal of Physical Chemistry C, 116 (2011), 1772-1779.

[72] A. Nalaparaju, X.S. Zhao, and J.W. Jiang, Molecular Understanding for the Adsorption of Water and Alcohols in Hydrophilic and Hydrophobic Zeolitic Metal−Organic Frameworks, The Journal of Physical Chemistry C, 114 (2010), 11542-11550.

[73] Y. Chen and J. Jiang, A Bio-Metal–Organic Framework for Highly Selective CO_2 Capture: A Molecular Simulation Study, ChemSusChem, 3 (2010), 982-988.

[74] P. Ryan, O.K. Farha, L.J. Broadbelt et al., Computational Screening of Metal-Organic Frameworks for Xenon/Krypton Separation, AIChE Journal, 57 (2011), 1759-1766.

[75] J.A. Greathouse, T.L. Kinnibrugh, and M.D. Allendorf, Adsorption and Separation of Noble Gases by IRMOF-1: Grand Canonical Monte Carlo Simulations, Industrial & Engineering Chemistry Research, 48 (2009), 3425-3431.

[76] A.I. Skoulidas, Molecular Dynamics Simulations of Gas Diffusion in Metal−Organic Frameworks: Argon in CuBTC, Journal of the American Chemical Society, 126 (2004), 1356-1357.

[77] T. Van Heest, S.L. Teich-McGoldrick, J.A. Greathouse et al., Identification of Metal–Organic Framework Materials for Adsorption Separation of Rare Gases: Applicability of Ideal Adsorbed Solution Theory (IAST) and Effects of Inaccessible Framework Regions, The Journal of Physical Chemistry C, 116 (2012), 13183-13195.

[78] B.J. Sikora, C.E. Wilmer, M.L. Greenfield et al., Thermodynamic Analysis of Xe/Kr Selectivity in Over 137 000 Hypothetical Metal-Organic Frameworks, chemical science, 3 (2012), 2217-2223.

[79] U. Mueller, M. Schubert, F. Teich et al., Metal organic frameworks-prospective industrial applications, J. Mater. Chem., 16 (2006), 626-636.

[80] J. Liu, P.K. Thallapally, and D. Strachan, Metal–Organic Frameworks for Removal of Xe and Kr from Nuclear Fuel Reprocessing Plants, Langmuir, 28 (2012), 11584-11589.

[81] P.K. Thallapally, J.W. Grate, and R.K. Motkuri, Facile Xenon Capture and Release at Room Temperature Using a Metal-Organic Framework: A Comparison with Activated Charcoal, Chemical Communications, 48 (2012), 347-349.

[82] A. Soleimani Dorcheh, D. Denysenko, D. Volkmer et al., Noble Gases and Microporous Frameworks; from Interaction to Application, Microporous and Mesoporous Materials, 162 (2012), 64-68.

[83] C.A. Fernandez, J. Liu, P.K. Thallapally et al., Switching Kr/Xe Selectivity with Temperature in a Metal–Organic Framework, Journal of the American Chemical Society, 134 (2012), 9046-9049.

[84] R.L. June, A.T. Bell, and D.N. Theodorou, Molecular Dynamics Study of Methane and Xenon in Silicalite, Journal of Physical Chemistry, 94 (1990), 8232-8240.

[85] A.I. Skoulidas and D.S. Sholl, Self-Diffusion and Transport Diffusion of Light Gases in Metal-Organic Framework Materials Assessed Using Molecular Dynamics Simulations, The journal of physical chemistry B, 109 (2005), 15760-15768.

[86] N.-K.B. Steffen Jost, Siegfried Fritzsche, Reinhold Haberlandt, Jorg Karger, Diffusion of a Mixture of Methane and Xenon in Silicate: A Molecular Dynamics Study and Pulsed Field Gradient Nuclear Magnetic Resonance Experiments, Journal of Physical Chemistry B, 102 (1998), 6375.

[87] D.D. Do, H.D. Do, and K. Kaneko, Effect of Surface-Perturbed Intermolecular Interaction on Adsorption of Simple Gases on a Graphitized Carbon Surface, Langmuir, 20 (2004), 7623-7629.
[88] S.T. Meek, S.L. Teich-McGoldrick, J.J. Perry et al., Effects of Polarizability on the Adsorption of Noble Gases at Low Pressures in Monohalogenated Isoreticular Metal–Organic Frameworks, The Journal of Physical Chemistry C, 116 (2012), 19765-19772.
[89] N. Metropolis, A.W. Rosenbluth, M.N. Rosenbluth et al., Equation of State Calculations by Fast Computing Machines, Journal of Chemical Physics, 21 (1953), 1087-1092.
[90] D. Frenkel and B. Smit, Understanding Molecular Simulation: From Algorithms to Applications, 2nd ed, Academic Press, (2002).
[91] M.P. Allen and D.J. Tildesley, Computer Simulation of Liquids, Clarendon Press, (1987).
[92] D.N. Theodorou, Progress and Outlook in Monte Carlo Simulations, Industrial & Engineering Chemistry Research, 49 (2010), 3047-3058.
[93] J.M. Haile, Molecular Dynamics Simulation, John Wiley & Sons, (1992).
[94] D.N. Theodorou, R.Q. Snurr, and A.T. Bell, eds, Molecular Dynamics and Diffusion in Microporous Materials, ed., G. Alberti and T. Bein, Elsevier Science, (1996).
[95] H.L. Tepper and W.J. Briels, Comments on the Use of the Einstein Equation for Transport Diffusion: Application to Argon in AlPO4-5, Journal of Chemical Physics, 116 (2002), 9464-9474.
[96] D.M. Ackerman, A.I. Skoulidas, D.S. Sholl et al., Diffusivities of Ar and Ne in carbon nanotubes, Molecular Simulations, 29 (2003), 677-684.
[97] M.J. Sanborn and R.Q. Snurr, Diffusion of Binary Mixtures of CF_4 and n-Alkanes in Faujasite, Separation Purification Technology, 20 (2000), 1-13.
[98] A.I. Skoulidas and D.S. Sholl, Self-Diffusion and Transport Diffusion of Light Gases in Metal-Organic Framework Materials Assessed Using Molecular Dynamics Simulations, Journal of Physical Chemistry B, 109 (2005), 15760-15768.
[99] A.I. Skoulidas and D.S. Sholl, Molecular Dynamics Simulations of Self-Diffusivities, Corrected Diffusivities, and Transport Diffusivities of Light Gases in Four Silica Zeolites to Assess Influences of Pore Shape and Connectivity, Journal of Physical Chemistry A, 107 (2003), 10132-10141.
[100] S.-T. Hwang, Nonequilibrium Thermodynamics of Membrane Transport, AIChE Journal, 50 (2004), 862-870.
[101] L. Onsager, Reciprocal Relations in Irreversible Processes. I, Physical Review, 37 (1931), 405-426.

[102] L. Onsager, Reciprocal Relations in Irreversible Processes. II, Physical Review, 38 (1931), 2265-2279.
[103] J. Karger, Ruthven D.M., Diffusion in Zeolites and Other Microporous Solids, John Wiley & Sons, (1992).
[104] J.M.D. MacElroy, ed. Diffusion in Polymers, ed., P. Neogi, Dekker, (1995).
[105] D. Stauffer, Introduction to Percolation Theory, Taylor and Francis, (1985).
[106] K. Hahn, J. Kärger, and V. Kukla, Single-File Diffusion Observation, Physical Review Letters, 76 (1996), 2762-2765.
[107] C. Lutz, M. Kollmann, and C. Bechinger, Single-File Diffusion of Colloids in One-Dimensional Channels, Physical Review Letters, 93 (2004), 26001-26004.
[108] H.B. Callen, Thermodynamics and An Introduction to Thermosatistics, John Wiley & Sons, (1985).
[109] M.J. Sanborn and R.Q. Snurr, Predicting Membrane Flux of CH_4 and CF_4 Mixtures in Faujasite from Molecular Simulations, AIChE Journal, 47 (2001), 2032-2041.
[110] J.P. Hansen and I.R. McDonald, Theory of Simple Liquids, 2nd edn ed, Academic Press, (1986).
[111] G.K. Papadopoulos, H. Jobic, and D.N. Theodorou, Transport Diffusivity of N_2 and CO_2 in Silicalite: Coherent Quasielastic Neutron Scattering Measurements and Molecular Dynamics Simulations, Journal of Physical Chemistry B, 108 (2004), 12748-12756.
[112] A.I. Skoulidas, T.C. Bowen, C.M. Doelling et al., Comparing Atomistic Simulations and Experimental Measurements for CH_4/CF_4 Mixture Permeation through Silicalite Membranes, Journal of Membrane Science, 227 (2003), 123-136.
[113] R.B. Bird, W.E. Stewart, and E.N. Lightfoot, Transport Phenomena, John Wiley & Sons, (2007).
[114] M. Sant, J.M. Leyssale, G.K. Papadopoulos et al., Molecular Dynamics of Carbon Dioxide, Methane and Their Mixtures in a Zeolite Possessing Two Independent Pore Networks as Revealed by Computer Simulations, Journal of Physical Chemistry B, 113 (2009), 13761-13767.
[115] G.K. Papadopoulos and D.N. Theodorou, Simulation Studies of Methane, Carbon dioxide, Hydrogen and Deuterium in ITQ-1 and NaX Zeolites, Molecular Simulation, 35 (2009), 79-89.
[116] S. Chempath, R. Krishna, and R.Q. Snurr, Nonequilibrium Molecular Dynamics Simulations of Diffusion of Binary Mixtures Containing Short n-Alkanes in Faujasite, Journal of Physical Chemistry B, 108 (2004), 13481-13491.
[117] J. Keil Frerich, R. Krishna, and M.-O. Coppens, Modeling of Diffusion in Zeolites, Reviews in Chemical Engineering, 16 (2000), 71-197.
[118] D.M. Ruthven, Principles of Adsorption and Adsorption Processes, Wiley, (1954).

[119] S. Keskin and D.S. Sholl, Efficient Methods for Screening of Metal Organic Framework Membranes for Gas Separations Using Atomically Detailed Models, Langmuir, 25 (2009), 11786-11795.
[120] S. Keskin and D.S. Sholl, Screening Metal−Organic Framework Materials for Membrane-based Methane/Carbon Dioxide Separations, The Journal of Physical Chemistry C, 111 (2007), 14055-14059.
[121] R. Krishna and J.M. van Baten, In Silica Screening of Zeolite Membranes for CO_2 Capture, J. Memb. Sci., 360 (2010), 323-333.
[122] R. Krishna and J.M. van Baten, In Silico Screening of Metal-Organic Frameworks in Separation Applications, Physical Chemistry Chemical Physic, 13 (2011), 10593-10616.
[123] S. Keskin and D.S. Sholl, Efficient Methods for Screening of Metal Organic Framework Membranes for Gas Separations using Atomically-detailed Models, Langmuir, 25 (2009), 11786-11795.
[124] R. Krishna and J.M. van Baten, Onsager Coefficients for Binary Mixture Diffusion in Nanopores, Chemical Engineering Science, 63 (2008), 3120-3140.
[125] M. Eddaoudi, J. Kim, N. Rosi et al., Systematic Design of Pore Size and Functionality in Isoreticular MOFs and Their Application in Methane Storage, Science, 295 (2002), 469-472.
[126] J.A. Greathouse and M.D. Allendorf, Force Field Validation for Molecular Dynamics Simulations of IRMOF-1 and Other Isoreticular Zinc Carboxylate Coordination Polymers, J. Phys. Chem. C, 112 (2008), 5795–5802.
[127] R. Babarao and J. Jiang, Diffusion and Separation of CO_2 and CH_4 in Silicalite, C_{168} Schwarzite and IRMOF-1: A comparative Study from Molecular Dynamics Simulation, Langmuir, 24 (2008), 5474-5484.
[128] D. Dubbeldam, H. Frost, K. S. Walton et al., Molecular Simulation of Adsorption Sites of Light Gases in the Metal-Organic Framework IRMOF-1, Fluid Phase Equilibria, 261 (2007), 152-161.
[129] R. Babarao, Z. Hu, J. Jiang et al., Storage and Separation of CO_2 and CH_4 in Silicalite, C_{168} Schwarzite, and IRMOF-1: A Comparative Study from Monte Carlo Simulations, Langmuir, 23 (2007), 659-666.
[130] S.S.-Y. Chui, S.M.-F. Lo, J.P.H. Charmant et al., A Chemically Functionalizable Nanoporous Material $[Cu_3(TMA)_2(H_2O)_3]_n$, Science, 283 (1999), 1148-1150.
[131] S. Keskin, J. Liu, J.K. Johnson et al., Atomically-Detailed Models of Gas Mixture Diffusion through CuBTC Membranes, Microporous Mesoporous Materials, 125 (2009), 101-106.
[132] C. Chmelik, J. Kärger, M. Wiebcke et al., Adsorption and Diffusion of Alkanes in CuBTC Crystals Investigated Using Infrared Microscopy and Molecular Simulations, Microporous Mesoporous Materials, 117 (2009), 22-32.

[133] N.L. Rosi, J. Kim, M. Eddaoudi et al., Rod Packings and Metal-Organic Frameworks Constructed from Rod-Shaped Secondary Building Units, Journal of the American Chemical Society, 127 (2005), 1504-1518.
[134] P.D.C. Dietzel, B. Panella, M. Hirscher et al., Hydrogen Adsorption in a Nickel Based Coordination Polymer with Open Metal Sites in the Cylindrical Cavities of the Desolvated Framework, Chemical Communications, (2006), 959-961.
[135] A. Phan, C.J. Doonan, F.J. Uribe-Romo et al., Synthesis, Structure, and Carbon Dioxide Capture Properties of Zeolitic Imidazolate Frameworks, Acc.Chem. Res., 43 (2010), 58-67.
[136] K.S. Park, Z. Ni, A.P. Cote et al., Exceptional Chemical and Thermal Stability of Zeolitic Imidazolate Frameworks, Proc. Nat. Acad. Sci., 103 (2006), 10186-10191.
[137] J. Liu, J.Y. Lee, L. Pan et al., Adsorption and Diffusion of Hydrogen in a New Metal Organic Framework Material:[Zn(bdc)(ted)$_{0.5}$], Journal of Physical Chemistry C, 112 (2008), 2911-2917.
[138] J. An, S.J. Geib, and N.L. Rosi, High and Selective CO2 Uptake in a Cobalt Adeninate Metal-Organic Framework Exhibiting Pyrimidine- and Amino-Decorated Pores, Journal of the American Chemical Society, 132 (2010), 38-39.
[139] S.L. Mayo, B.D. Olafson, and W.A. Goddard, Dreiding: A Generic Force Field for Molecular Simulations, Journal of Physical Chemistry C, 94 (1990), 8897-8909.
[140] A.K. Rappe, C.J. Casewit, K.S. Colwell et al., UFF, A Full Periodic Table Force Field for Molecular Mechanics and Molecular Dynamics Simulations, Journal of American Chemical Society, 114 (1992), 10024-10035.
[141] D. Wu, C. Wang, B. Liu et al., Large-Scale Computational Screening of Metal-Organic Frameworks for CH_4/H_2 Separation, AIChE J., DOI 10.1002/aic.12744.
[142] P.D.C. Dietzel, B. Panella, M. Hirscher et al., Hydrogen Adsorption in a Nickel Based Coordination Polymer with Open Metal Sites in the Cylindrical Cavities of the Desolvated Framework, Chemical Community, (2006), 959-961.
[143] L.N. Gergidis and D.N. Theodorou, Molecular Dynamics Simulation of n-Butane-Methane Mixtures in Silicalite, Journal of Physical Chemistry B, 103 (1999), 3380-3390.
[144] G.C. Maitland, M. Rigby, E.B. Smith et al., Intermolecular Forces: Their Origin and Determination, Clarendon Press, (1981).
[145] M.P. Allen and D.J. Tildesley, Computer Simulation of Liquids, Clarendon Press;Oxford University Press, (1987).
[146] D. Frenkel and B. Smit, Understanding Molecular Simulation : From Algorithms to Applications, Understanding Molecular Simulation : From Algorithms to Applications, (2002).

[147] Y.-S. Bae and R.Q. Snurr, Development and Evaluation of Porous Materials for Carbon Dioxide Separation and Capture, Angewandte Chemie International Edition, 50 (2011), 11586-11596.
[148] Y. Gurdal and S. Keskin, Atomically Detailed Modeling of Metal Organic Frameworks for Adsorption, Diffusion, and Separation of Noble Gas Mixtures, Industrial & Engineering Chemistry Research, 51 (2012), 7373-7382.
[149] D.C. Ford, D. Dubbeldam, R.Q. Snurr et al., Self-Diffusion of Chain Molecules in the Metal–Organic Framework IRMOF-1: Simulation and Experiment, the journal of physical chemistry letters, 3 (2012), 930-933.
[150] M.J. Sanborn and R.Q. Snurr, Diffusion of Binary Mixtures of CF_4 and n-Alkanes in Faujasite, Separation and Purification Technology, 20 (2000), 1-13.
[151] R. Krishna, Diffusion of Binary Mixtures in Zeolites: Molecular Dynamics Simulations versus Maxwell-Stefan Theory, Chemical Physics Letters, 326 (2000), 477-484.
[152] S. Keskin, J.C. Liu, J.K. Johnson et al., Testing the Accuracy of Correlations for Multicomponent Mass Transport of Adsorbed Gases in Metal-Organic Frameworks: Diffusion of H_2/CH_4 Mixtures in CuBTC, Langmuir, 24 (2008), 8254-8261.
[153] D.S. Sholl and C.K. Lee, Influences of Concerted Cluster Diffusion on Single-File Diffusion of CF_4 in AlPO4-5 and Xe in AlPO4-31, Journal of Chemical Physics, 112 (2000), 817-824.
[154] D.S. Sholl, Predicting Single-Component Permeance through Macroscopic Zeolite Membranes from Atomistic Simulations, Industrial & Engineering Chemistry Research, 39 (2000), 3737-3746.
[155] A.I. Skoulidas, D.S. Sholl, and R. Krishna, Correlation Effects in Diffusion of CH_4/CF_4 Mixtures in MFI Zeolite. A Study Linking MD Simulations with the Maxwell-Stefan Formulation, Langmuir, 19 (2003), 7977-7988.
[156] H. Bux, C. Chmelik, R. Krishna et al., Ethene/ethane Separation by the MOF Membrane ZIF-8: Molecular Correlation of Permeation, Adsorption, Diffusion, Journal of Membrane Science, 369 (2011), 284-289.
[157] B. Liu and B. Smit, Comparative Molecular Simulation Study of CO_2/N_2 and CH_4/N_2 Separation in Zeolites and Metal-Organic Frameworks, Langmuir, 25 (2009), 5918-5926.
[158] A.N. Dickey, A.O. Yazaydin, R.R. Willis et al., Screening CO_2/N_2 Selectivity in Metal-Organic Frameworks Using Monte Carlo Simulations and Ideal Adsorbed Solution Theory, Canadian Journal of Chemical Engineering, 90 (2012), 825-832.
[159] D. Dubbeldam, K.S. Walton, D.E. Ellis et al., Exceptional Negative Thermal Expansion in Isoreticular Metal-Organic Frameworks, Angew. Chem. Int. Ed., 46 (2007), 4496-4499.

[160] R.E. Bazan, M. Bastos-Neto, A. Moeller et al., Adsorption Equilibria of O_2, Ar, Kr and Xe on Activated Carbon and Zeolites: Single Component and Mixture Data, Journal of the International Adsorption Society, 17 (2011), 371-383.

[161] S. Keskin, J.C. Liu, J.K. Johnson et al., Testing the Accuracy of Correlations for Multicomponent Mass Transport of Adsorbed Gases in Metal-Organic Frameworks: Diffusion of H_2/CH_4 Mixtures in CuBTC, Langmuir, 24 (2008), 8254-8261.

[162] H.B. Chen and D.S. Sholl, Examining the Accuracy of Ideal Adsorbed Solution Theory without Curve-Fitting Using Transition Matrix Monte Carlo Simulations, Langmuir, 23 (2007), 6431-6437.

[163] J. Izumi, Waste Gas Treatment Using Zeolites in Nuclear-Related Industries, in Handbook of Zeolite Science and Technology, S.M. Auerbach, K. Carrado, and P. Dutta, Editors, Marcel Dekker, (2003).

[164] C.J. Jameson, A.K. Jameson, and H.M. Lim, Competitive Adsorption of Xenon and Krypton in Zeolite NaA: Xe-129 Nuclear Magnetic Resonance Studies and Grand Canonical Monte Carlo Simulations, Journal of Chemical Physics, 107 (1997), 4364-4372.

[165] M. Foroutan and A.T. Nasrabadi, Adsorption and Separation of Binary Mixtures of Noble Gases on Single-Walled Carbon Nanotube Bundles, Physica E-Low-Dimensional Systems & Nanostructures, 43 (2011), 851-856.

[166] J. van den Bergh, S.A. Ban, T.J.H. Vlugt et al., Diffusion in Zeolites: Extension of the Relevant Site Model to Light Gases and Mixtures thereof in Zeolites DDR, CHA, MFI and FAU, Separation Purification Technology, 73 (2010), 151-163.

[167] G. De Luca, P. Pullumbi, G. Barbieri et al., Calculation of the Diffusion Coefficients of Light Gases in Silicalite-1 Membrane and Silica-Sodalite Zeolite, Separation Purification Technology, 36 (2004), 215-228.

[168] D.S. Sholl, Predicting Single-Component Permeance through Macroscopic Zeolite Membranes from Atomistic Simulations, Industrial and Engineering Chemistry Research, 39 (2000), 3737-3746.

[169] Y. Nakai, H. Yoshimizu, and Y. Tsujita, Enhanced Gas Permeability of Cellulose Acetate Membranes under Microwave Irradiation, Journal of Membrane Science, 256 (2005), 72-77.

[170] J. Karger and H. Pfeifer, NMR Self-Diffusion Studies in Zeolite Science and Technology, Zeolites, 7 (1987), 90-107.

[171] D.S. Sholl, Testing Predictions of Macroscopic Binary Diffusion Coefficients Using Lattice Models with Site Heterogeneity, Langmuir, 22 (2006), 3707-3714.

[172] D. Paschek and R. Krishna, Inter-Relation Between Self and Jump Diffusivities in Zeolites, Chemical Physics Letters, 333 (2001), 278-284.

[173] Q. Yang and C. Zhong, Molecular Simulation of Carbon Dioxide/Methane/Hydrogen Mixture Adsorption in Metal−Organic Frameworks, The Journal of Physical Chemistry B, 110 (2006), 17776-17783.
[174] J. Izumi, in Handbook of Zeolite Science and Technology, S.M. Auerbach, Carrado, K., Dutta, P., Eds., Editor, Marcel Dekker, (2003).
[175] Y. Gurdal and S. Keskin, Predicting Noble Gas Separation Performance of Metal Organic Frameworks Using Theoretical Correlations, The Journal of Physical Chemistry C, 117 (2013), 5229-5241.

APPENDIX

A:Modeling MOFs for Adsorption, Diffusion and Separation of Noble Gas Mixtures

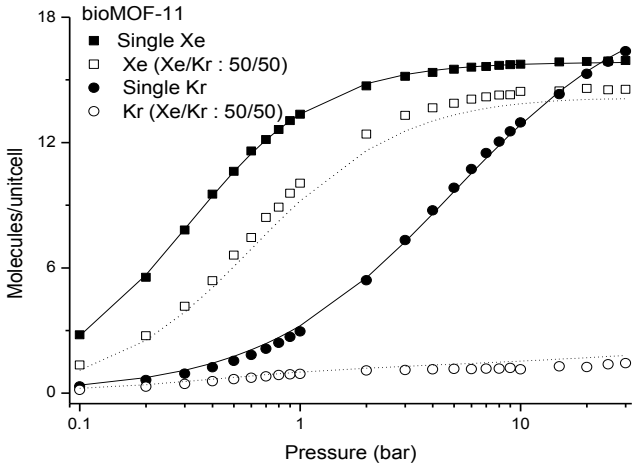

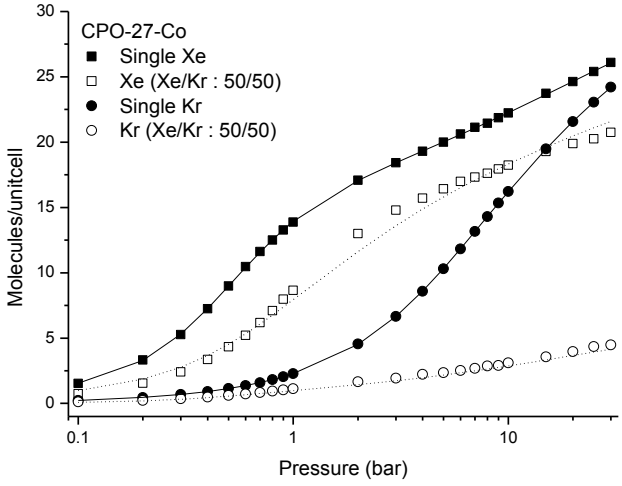

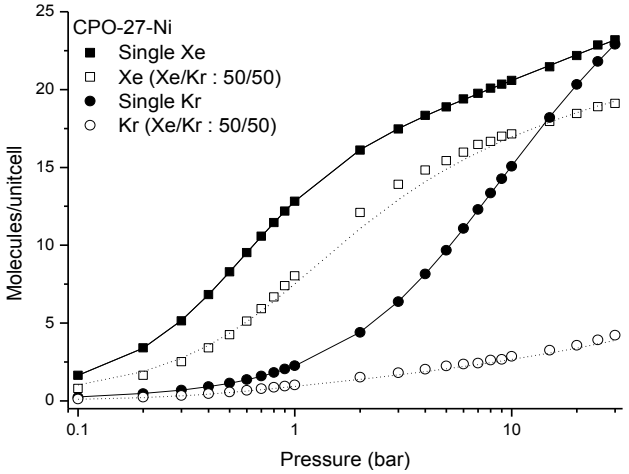
CPO-27-Ni
Single Xe
Xe (Xe/Kr : 50/50)
Single Kr
Kr (Xe/Kr : 50/50)
Molecules/unitcell
Pressure (bar)
0
5
10
15
20
25
0.1
1
10

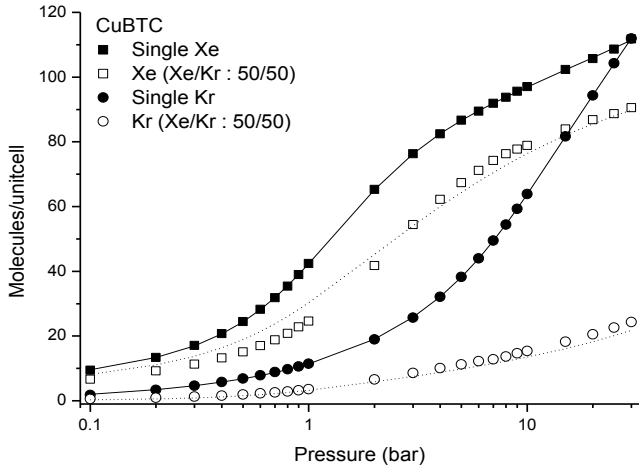
CuBTC
Single Xe
Xe (Xe/Kr : 50/50)
Single Kr
Kr (Xe/Kr : 50/50)
Molecules/unitcell
Pressure (bar)
0
20
40
60
80
100
120
0.1
1
10

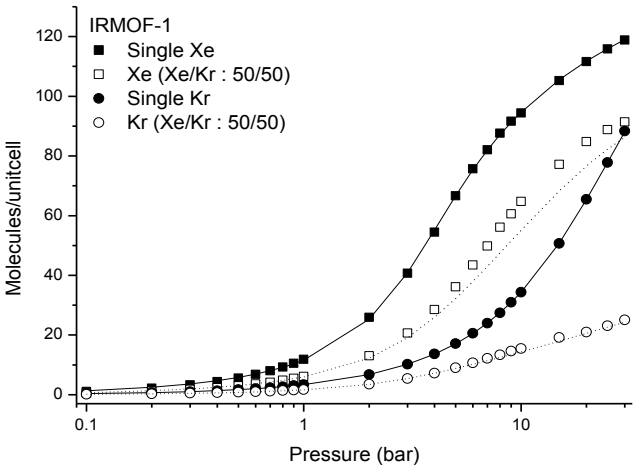
IRMOF-1
Single Xe
Xe (Xe/Kr : 50/50)
Single Kr
Kr (Xe/Kr : 50/50)
Molecules/unitcell
Pressure (bar)
0
20
40
60
80
100
120
0.1
1
10

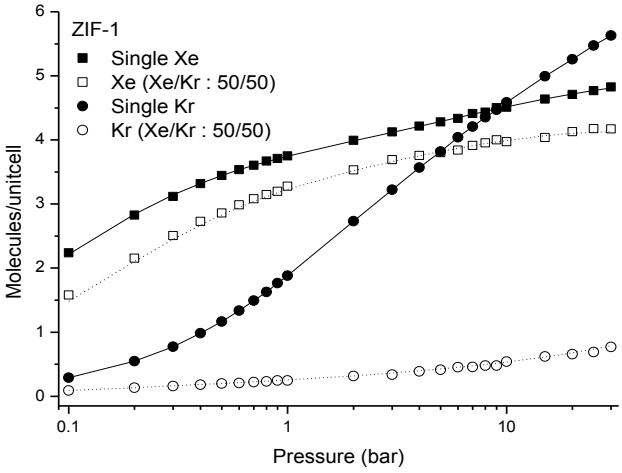
ZIF-1
Single Xe
Xe (Xe/Kr : 50/50)
Single Kr
Kr (Xe/Kr : 50/50)
Molecules/unitcell
Pressure (bar)
0
1
2
3
4
5
6
0.1
1
10

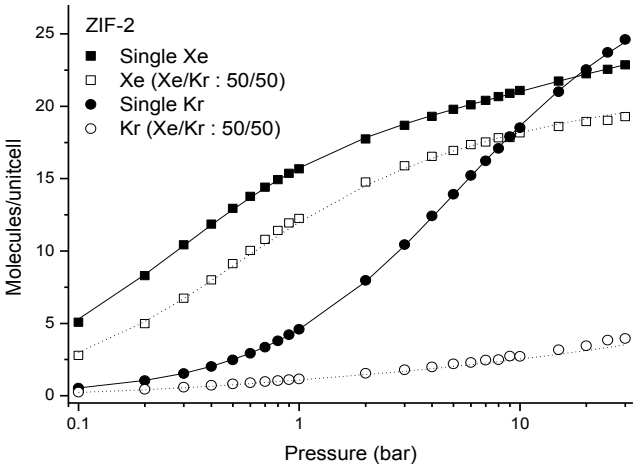
ZIF-2
Single Xe
Xe (Xe/Kr : 50/50)
Single Kr
Kr (Xe/Kr : 50/50)
Molecules/unitcell
Pressure (bar)
0
5
10
15
20
25
0.1
1
10

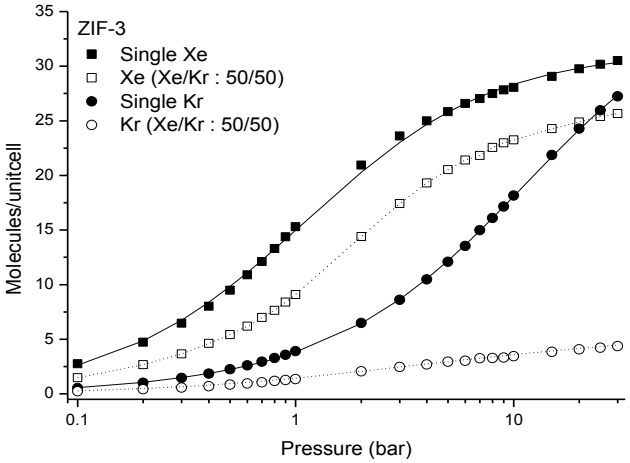
ZIF-3
Single Xe
Xe (Xe/Kr : 50/50)
Single Kr
Kr (Xe/Kr : 50/50)
Molecules/unitcell
Pressure (bar)
0
5
10
15
20
25
30
35
0.1
1
10

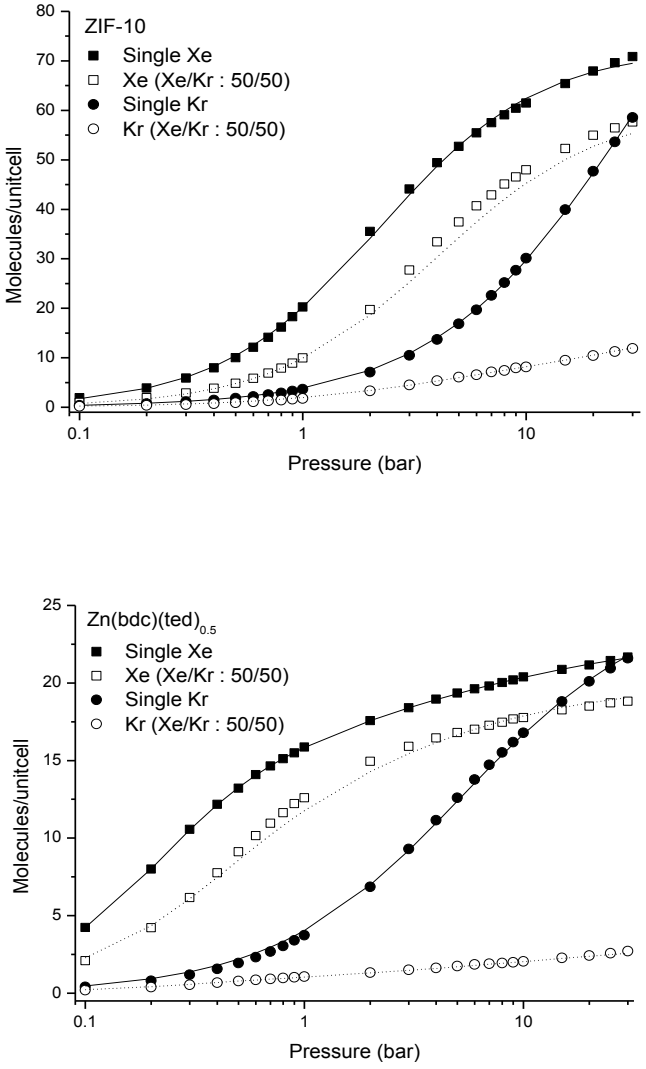

Figure A.1: Single component and binary adsorption isotherms of Xe and Kr in MOFs at room temperature. The composition of the bulk gas mixture is equimolar. The continuous and dotted lines represent the fitted single component adsorption isotherm and the prediction of IAST, respectively.

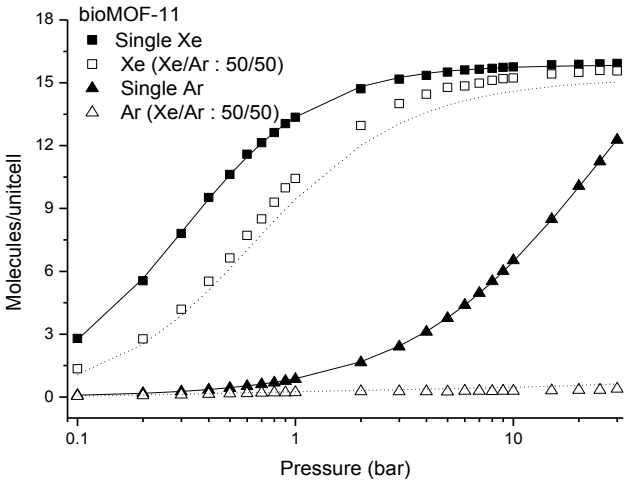
bioMOF-11
Single Xe
Xe (Xe/Ar : 50/50)
Single Ar
Ar (Xe/Ar : 50/50)
Molecules/unitcell
Pressure (bar)
0
3
6
9
12
15
18
0.1
1
10

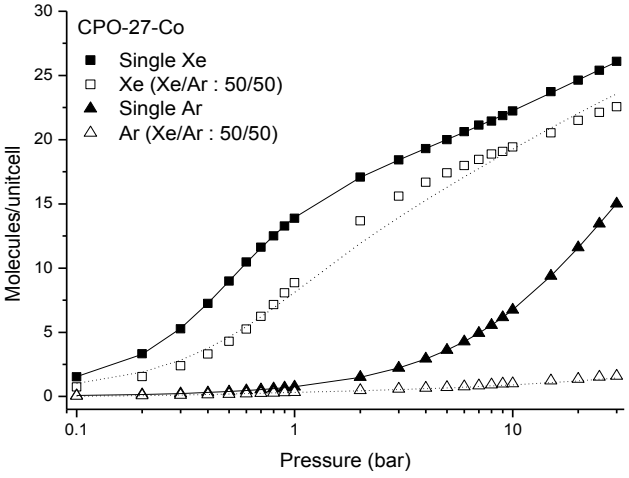
CPO-27-Co
Single Xe
Xe (Xe/Ar : 50/50)
Single Ar
Ar (Xe/Ar : 50/50)
Molecules/unitcell
Pressure (bar)
0
5
10
15
20
25
30
0.1
1
10

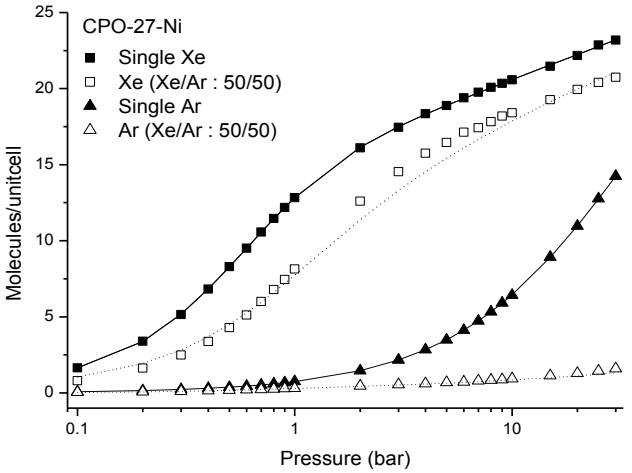
CPO-27-Ni
Single Xe
Xe (Xe/Ar : 50/50)
Single Ar
Ar (Xe/Ar : 50/50)
Molecules/unitcell
Pressure (bar)
0
5
10
15
20
25
0.1
1
10

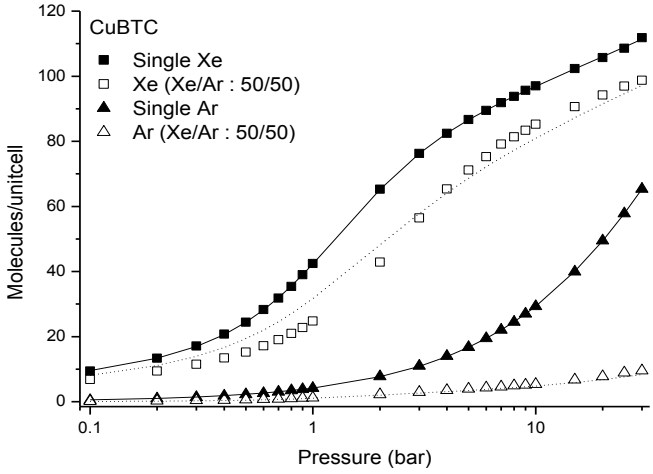
CuBTC
Single Xe
Xe (Xe/Ar : 50/50)
Single Ar
Ar (Xe/Ar : 50/50)
Molecules/unitcell
Pressure (bar)
0
20
40
60
80
100
120
0.1
1
10

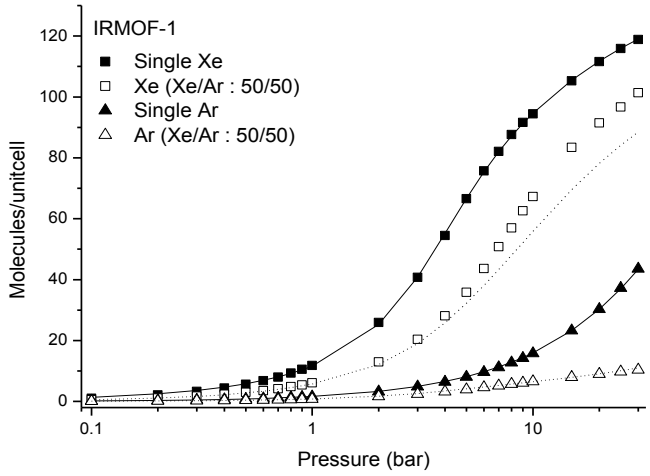
IRMOF-1
Single Xe
Xe (Xe/Ar : 50/50)
Single Ar
Ar (Xe/Ar : 50/50)
Molecules/unitcell
Pressure (bar)
0
20
40
60
80
100
120
0.1
1
10

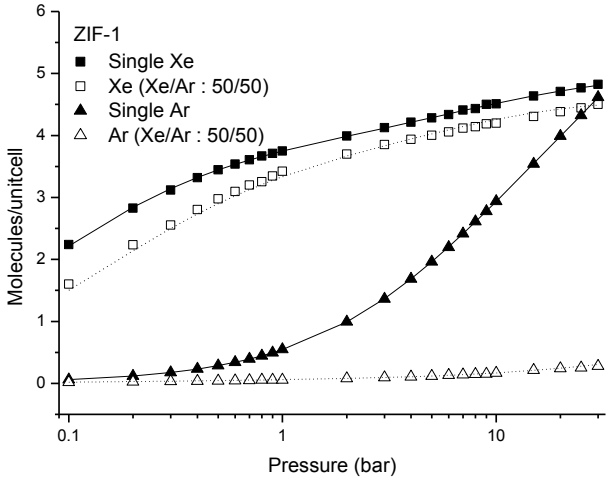
ZIF-1
Single Xe
Xe (Xe/Ar : 50/50)
Single Ar
Ar (Xe/Ar : 50/50)
Molecules/unitcell
Pressure (bar)
0
1
2
3
4
5
6
0.1
1
10

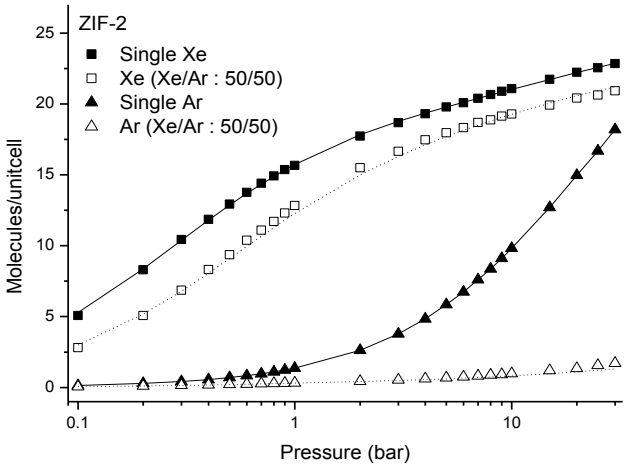
ZIF-2
Single Xe
Xe (Xe/Ar : 50/50)
Single Ar
Ar (Xe/Ar : 50/50)
Molecules/unitcell
Pressure (bar)
0
5
10
15
20
25
0.1
1
10

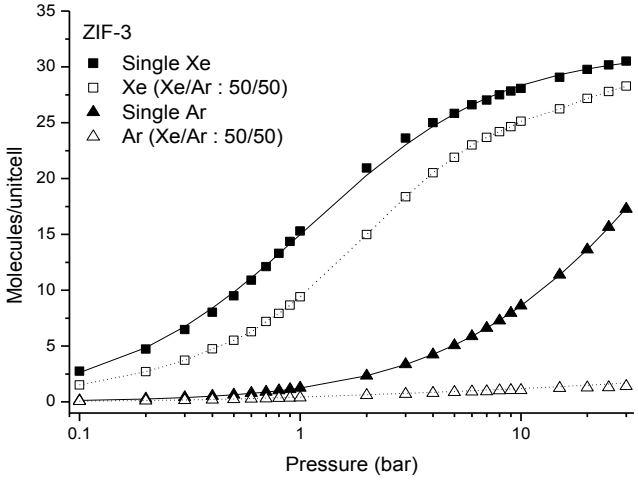
ZIF-3
Single Xe
Xe (Xe/Ar : 50/50)
Single Ar
Ar (Xe/Ar : 50/50)
Molecules/unitcell
Pressure (bar)
0
5
10
15
20
25
30
35
0.1
1
10

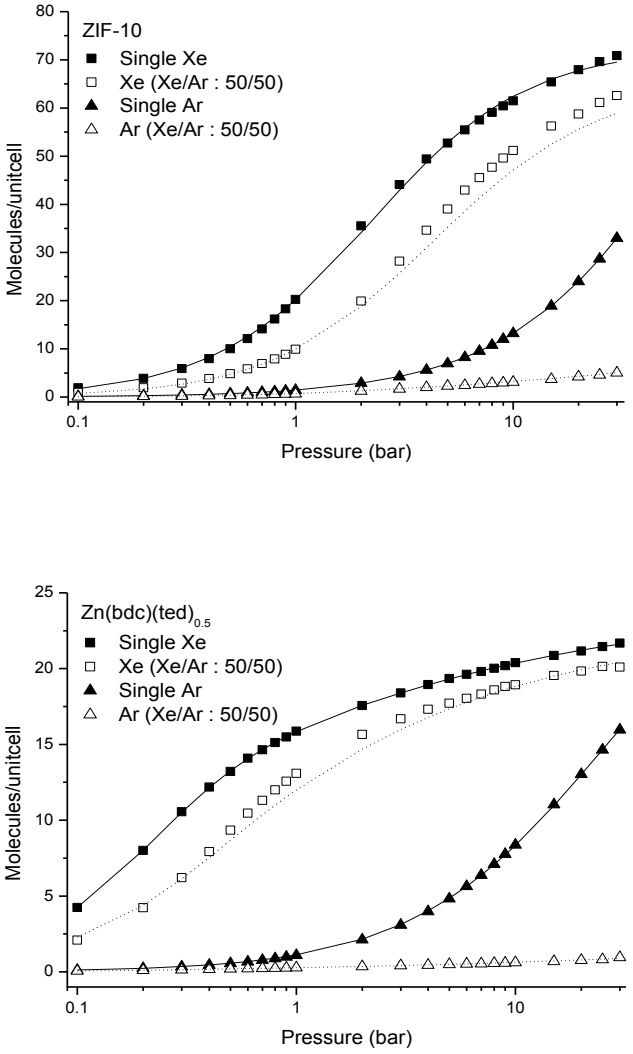

Figure A.2: Single component and binary adsorption isotherms of Xe and Ar in MOFs at room temperature. The composition of the bulk gas mixture is equimolar. The continuous and dotted lines represent the fitted single component adsorption isotherm and the prediction of IAST, respectively.

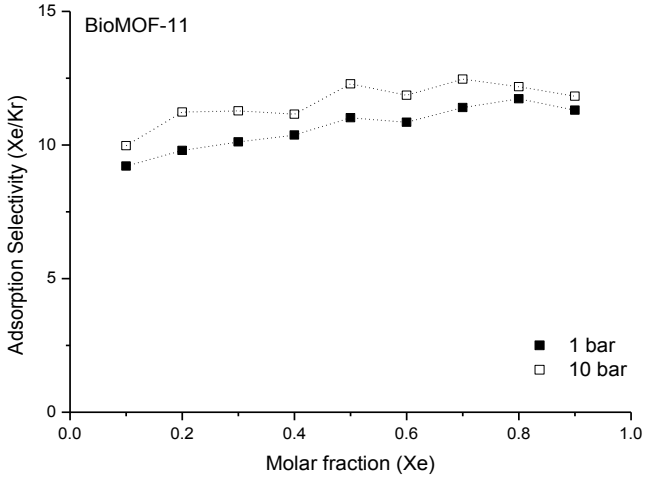
BioMOF-11
Adsorption Selectivity (Xe/Kr)
Molar fraction (Xe)
1 bar
10 bar
0
5
10
15
0.0
0.2
0.4
0.6
0.8
1.0

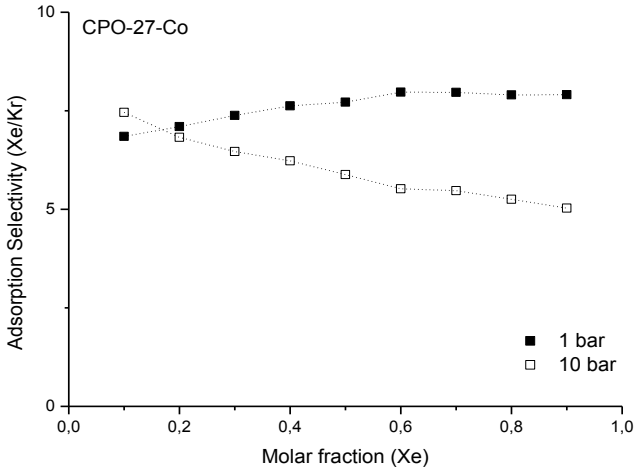
CPO-27-Co
Adsorption Selectivity (Xe/Kr)
Molar fraction (Xe)
1 bar
10 bar
0
5
10
0,0
0,2
0,4
0,6
0,8
1,0

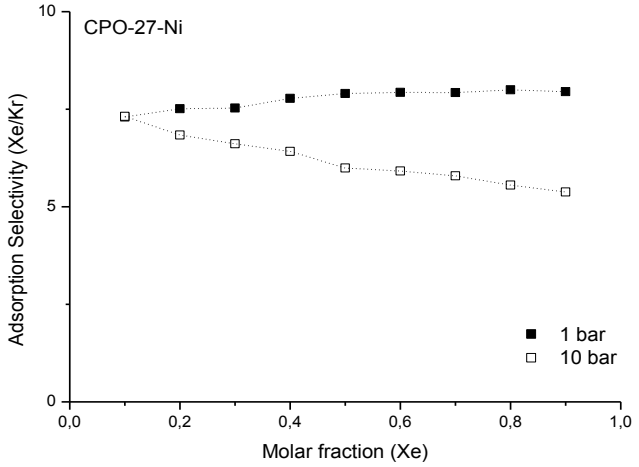
CPO-27-Ni
Adsorption Selectivity (Xe/Kr)
Molar fraction (Xe)
1 bar
10 bar
0
5
10
0,0
0,2
0,4
0,6
0,8
1,0

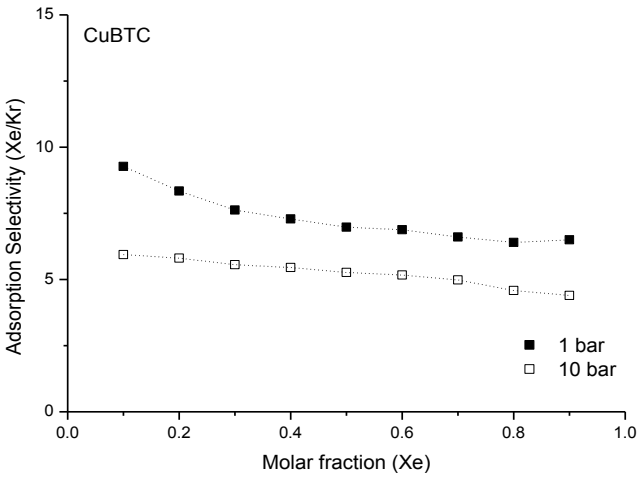
CuBTC
Adsorption Selectivity (Xe/Kr)
Molar fraction (Xe)
1 bar
10 bar
0
5
10
15
0.0
0.2
0.4
0.6
0.8
1.0

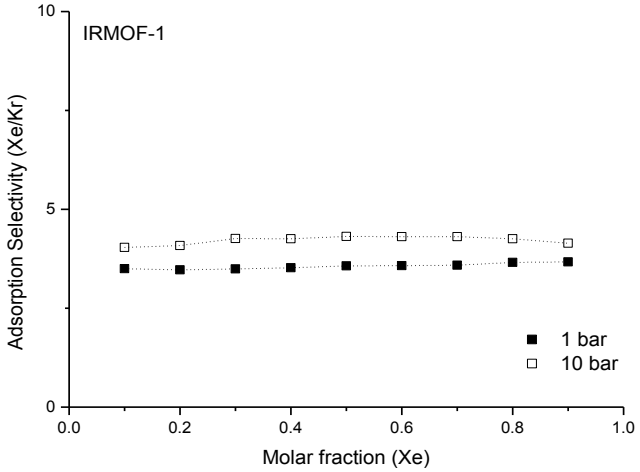
IRMOF-1
Adsorption Selectivity (Xe/Kr)
Molar fraction (Xe)
1 bar
10 bar
0
5
10
0.0
0.2
0.4
0.6
0.8
1.0

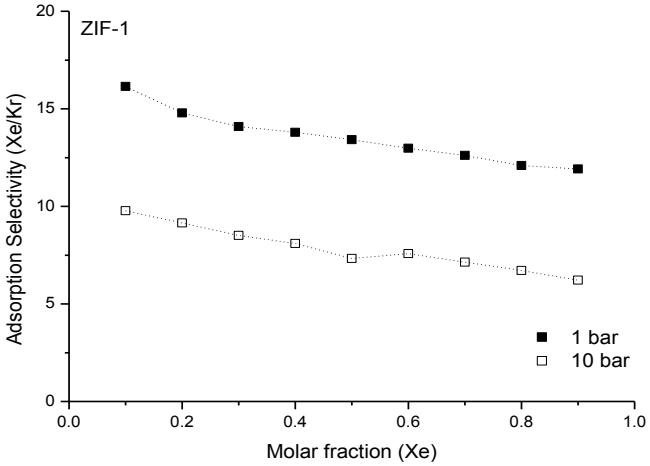
ZIF-1
Adsorption Selectivity (Xe/Kr)
Molar fraction (Xe)
1 bar
10 bar
0
5
10
15
20
0.0
0.2
0.4
0.6
0.8
1.0

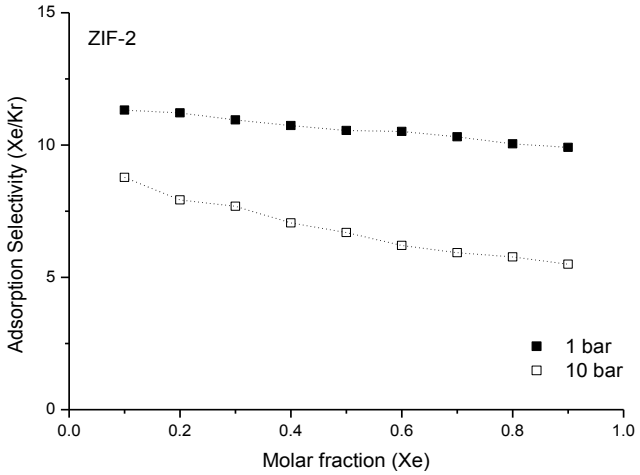
ZIF-2
Adsorption Selectivity (Xe/Kr)
Molar fraction (Xe)
1 bar
10 bar
0
5
10
15
0.0
0.2
0.4
0.6
0.8
1.0

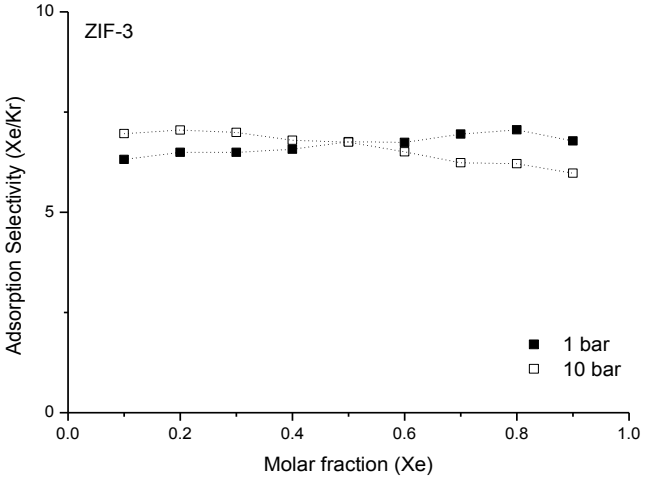
ZIF-3
Adsorption Selectivity (Xe/Kr)
Molar fraction (Xe)
1 bar
10 bar
0
5
10
0.0
0.2
0.4
0.6
0.8
1.0

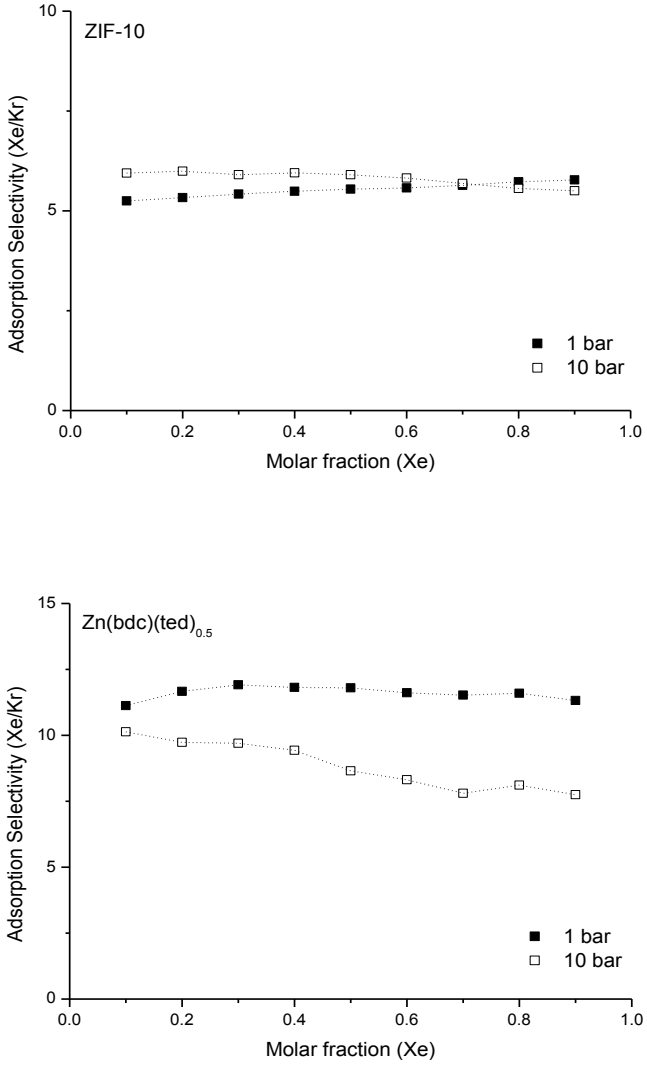

Figure A.3: Adsorption selectivity of MOFs for Xe from Xe/Kr mixtures at room temperature.

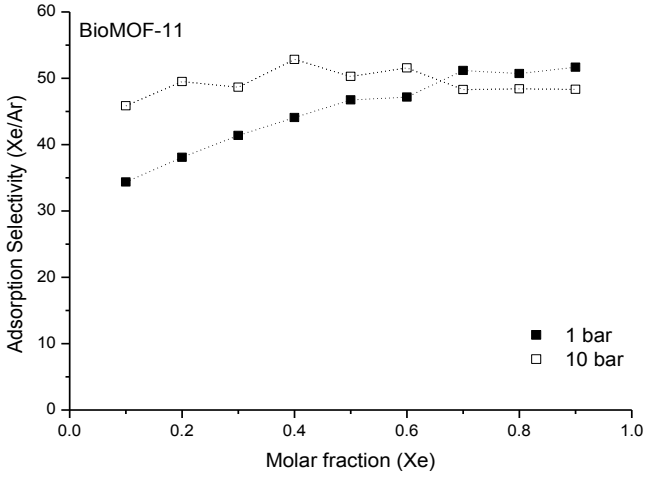
BioMOF-11
Adsorption Selectivity (Xe/Ar)
Molar fraction (Xe)
1 bar
10 bar
0
10
20
30
40
50
60
0.0
0.2
0.4
0.6
0.8
1.0

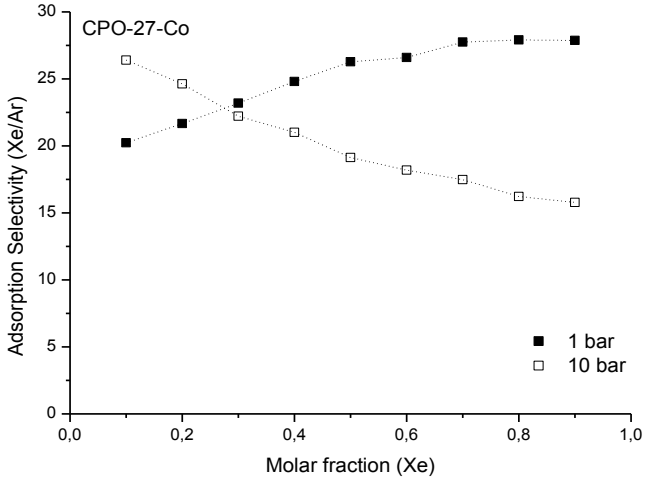
CPO-27-Co
Adsorption Selectivity (Xe/Ar)
Molar fraction (Xe)
1 bar
10 bar
0
5
10
15
20
25
30
0,0
0,2
0,4
0,6
0,8
1,0

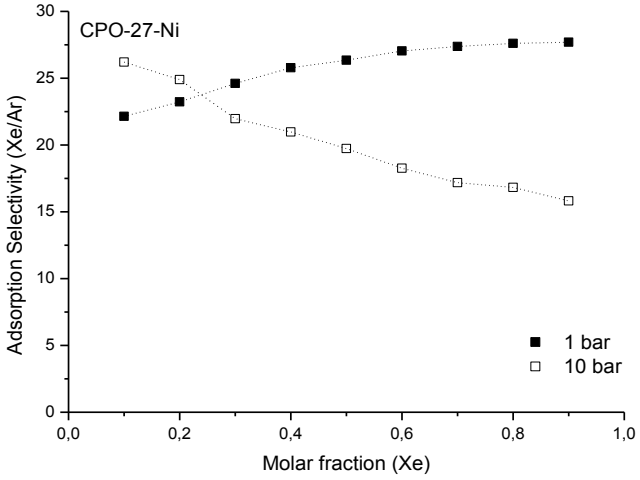
CPO-27-Ni
Adsorption Selectivity (Xe/Ar)
Molar fraction (Xe)
1 bar
10 bar
0
5
10
15
20
25
30
0,0
0,2
0,4
0,6
0,8
1,0

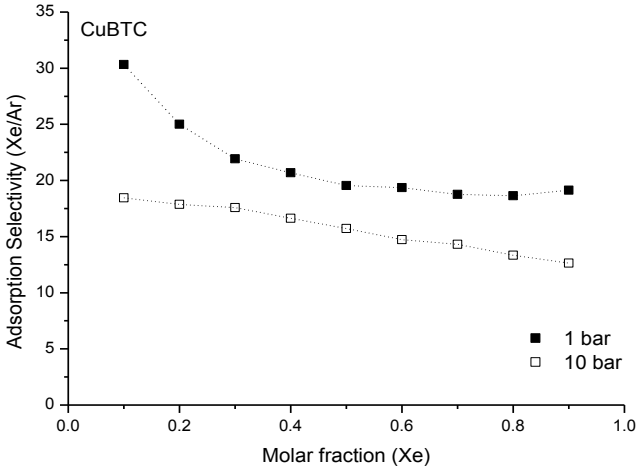
CuBTC
Adsorption Selectivity (Xe/Ar)
Molar fraction (Xe)
1 bar
10 bar
0
5
10
15
20
25
30
35
0.0
0.2
0.4
0.6
0.8
1.0

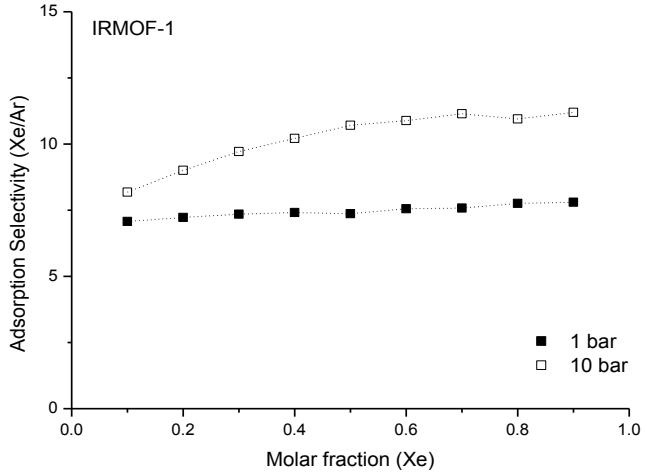
IRMOF-1
Adsorption Selectivity (Xe/Ar)
Molar fraction (Xe)
1 bar
10 bar
0
5
10
15
0.0
0.2
0.4
0.6
0.8
1.0

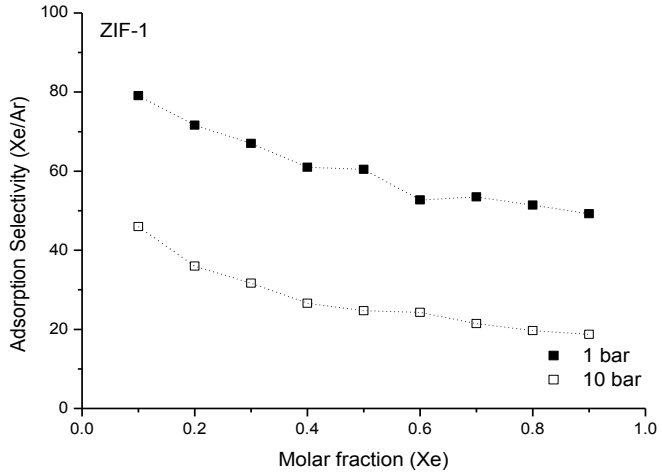
ZIF-1
Adsorption Selectivity (Xe/Ar)
Molar fraction (Xe)
1 bar
10 bar
0
20
40
60
80
100
0.0
0.2
0.4
0.6
0.8
1.0

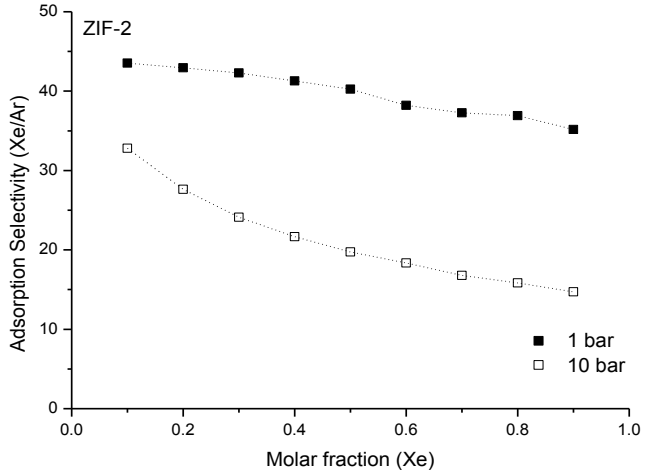
ZIF-2
Adsorption Selectivity (Xe/Ar)
Molar fraction (Xe)
1 bar
10 bar
0
10
20
30
40
50
0.0
0.2
0.4
0.6
0.8
1.0

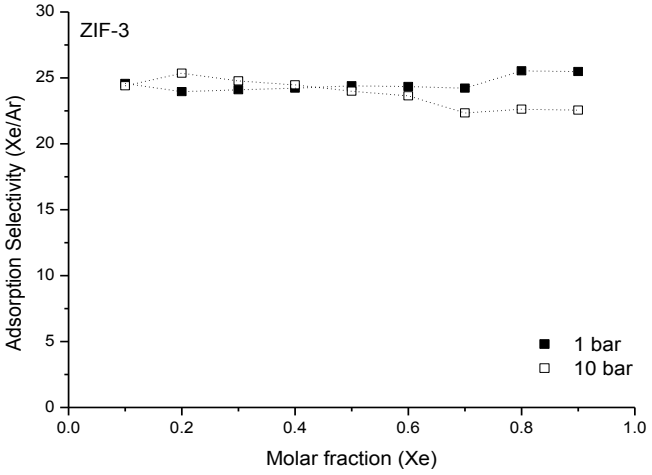
ZIF-3
Adsorption Selectivity (Xe/Ar)
Molar fraction (Xe)
1 bar
10 bar
0
5
10
15
20
25
30
0.0
0.2
0.4
0.6
0.8
1.0

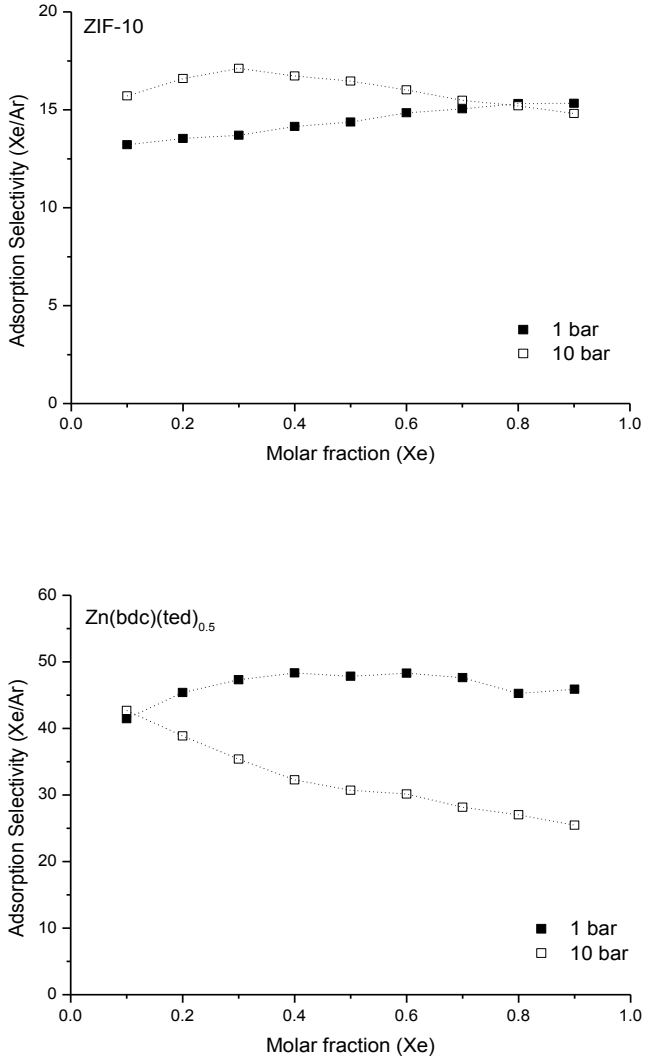

Figure A.4: Adsorption selectivity of MOFs for Xe from Xe/Ar mixtures at room temperature.

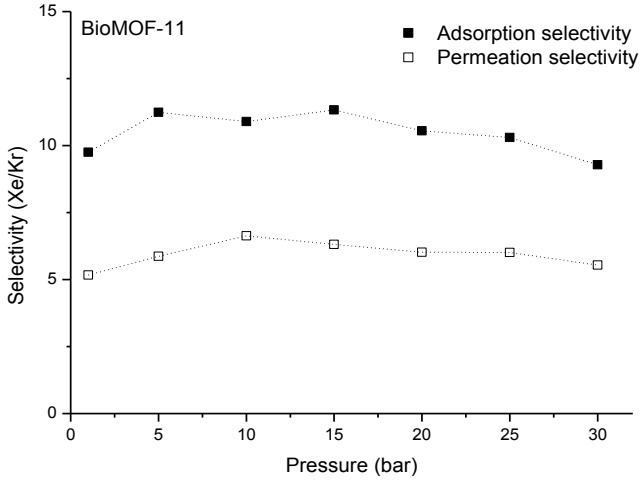
BioMOF-11
Adsorption selectivity
Permeation selectivity
Selectivity (Xe/Kr)
Pressure (bar)
0
5
10
15
20
25
30

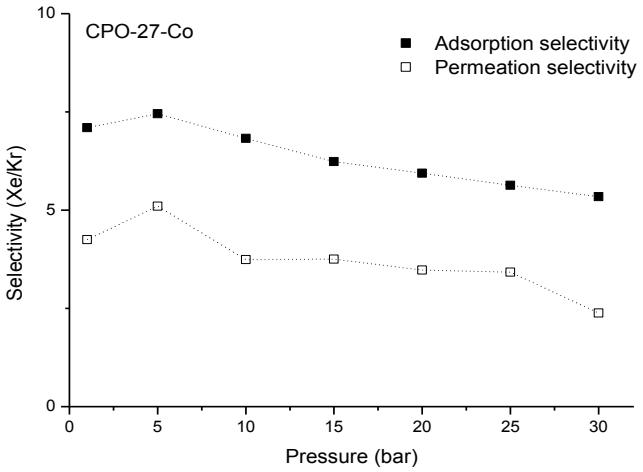
CPO-27-Co
Adsorption selectivity
Permeation selectivity
Selectivity (Xe/Kr)
Pressure (bar)
0
5
10
15
20
25
30

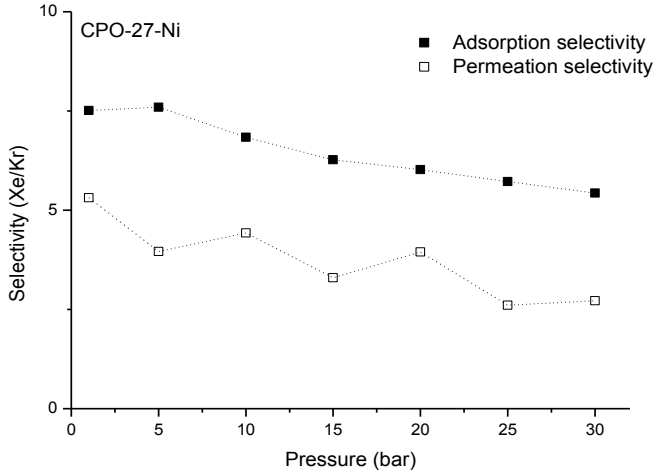
CPO-27-Ni
Adsorption selectivity
Permeation selectivity
Selectivity (Xe/Kr)
Pressure (bar)
0
5
10
15
20
25
30

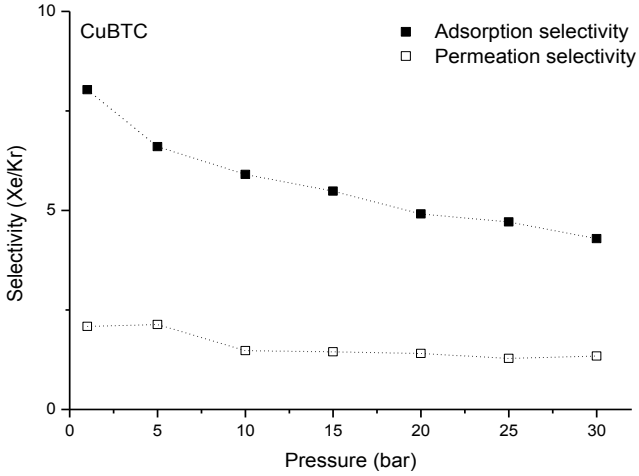
CuBTC
Adsorption selectivity
Permeation selectivity
Selectivity (Xe/Kr)
Pressure (bar)
0
5
10
15
20
25
30

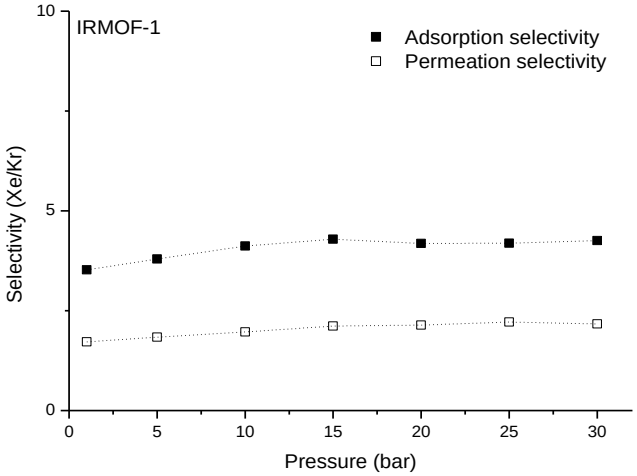
IRMOF-1
Adsorption selectivity
Permeation selectivity
Selectivity (Xe/Kr)
Pressure (bar)
0
5
10
15
20
25
30

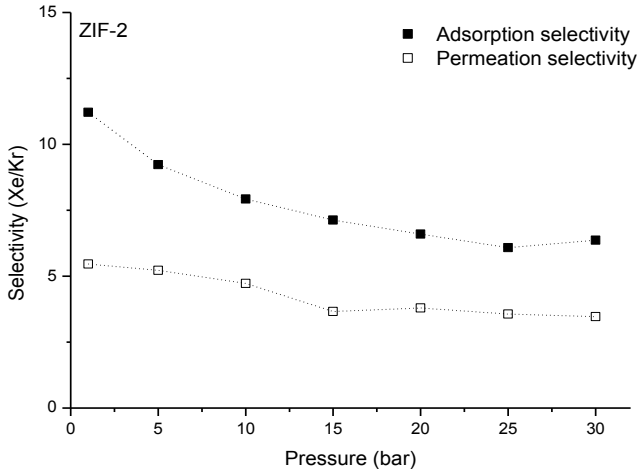
ZIF-2
Adsorption selectivity
Permeation selectivity
Selectivity (Xe/Kr)
Pressure (bar)
0
5
10
15
20
25
30

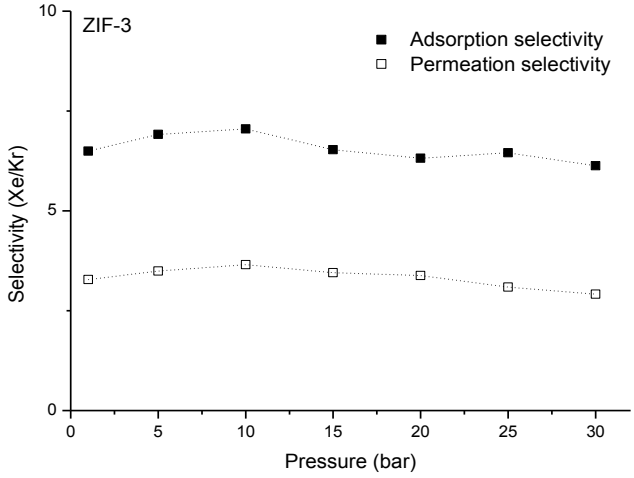
ZIF-3
Adsorption selectivity
Permeation selectivity
Selectivity (Xe/Kr)
Pressure (bar)
0
5
10
15
20
25
30

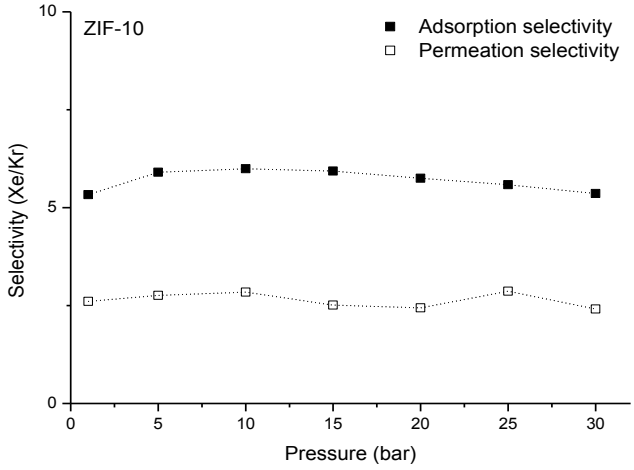
ZIF-10
Adsorption selectivity
Permeation selectivity
Selectivity (Xe/Kr)
Pressure (bar)
0
5
10
15
20
25
30

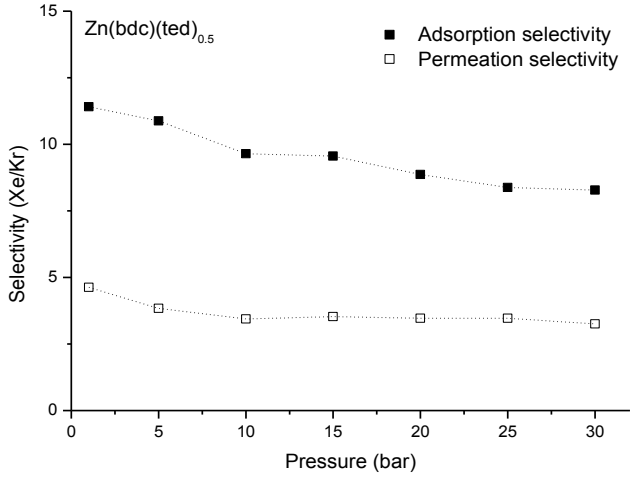

Figure A.5: Adsorption and permeation selectivity of MOFs for Xe/Kr mixtures at room temperature. The composition of the bulk gas mixture is 20/80.

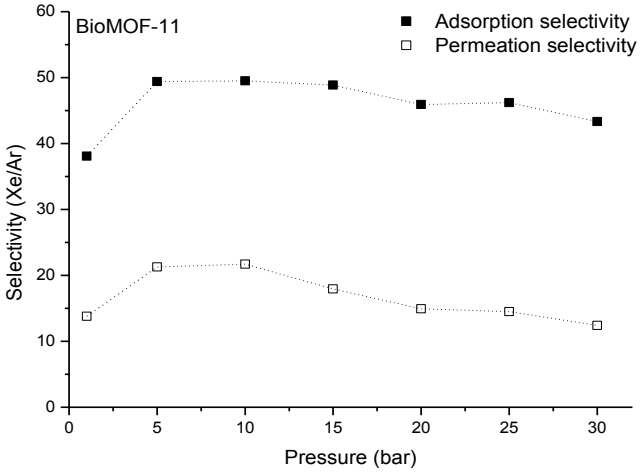

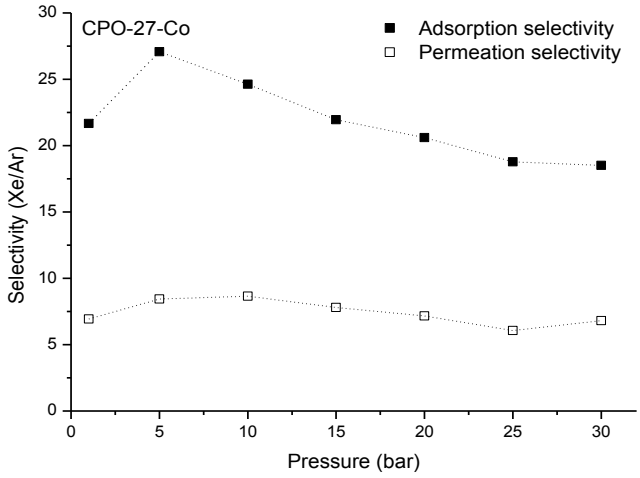
CPO-27-Co
Adsorption selectivity
Permeation selectivity
Selectivity (Xe/Ar)
Pressure (bar)
0
5
10
15
20
25
30

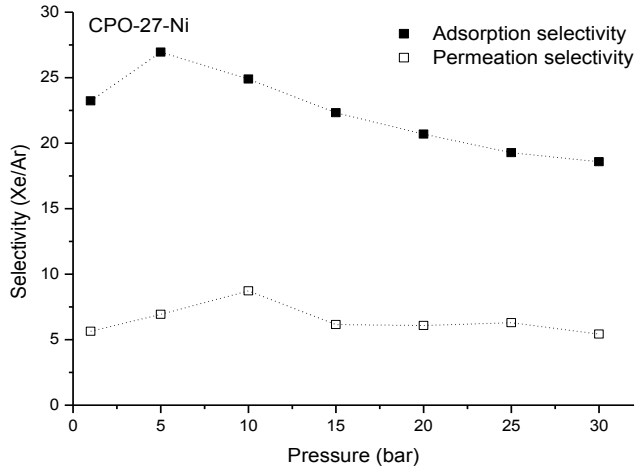
CPO-27-Ni
Adsorption selectivity
Permeation selectivity
Selectivity (Xe/Ar)
Pressure (bar)
0
5
10
15
20
25
30

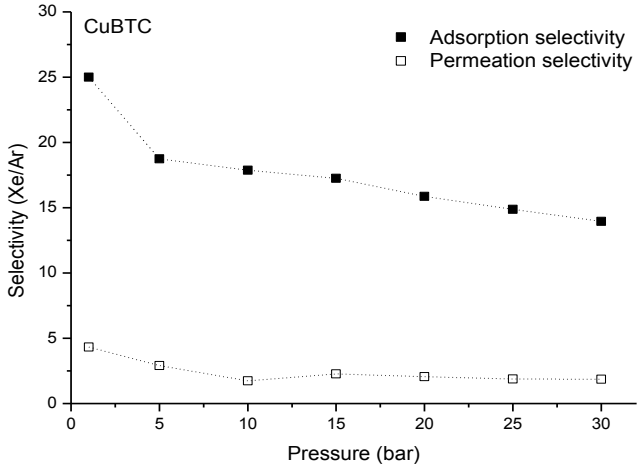
CuBTC
Adsorption selectivity
Permeation selectivity
Selectivity (Xe/Ar)
Pressure (bar)
0
5
10
15
20
25
30

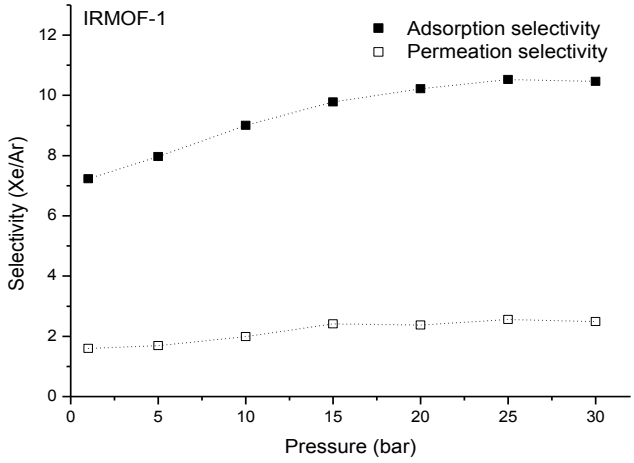
IRMOF-1
Adsorption selectivity
Permeation selectivity
Selectivity (Xe/Ar)
Pressure (bar)
0
2
4
6
8
10
12
0
5
10
15
20
25
30

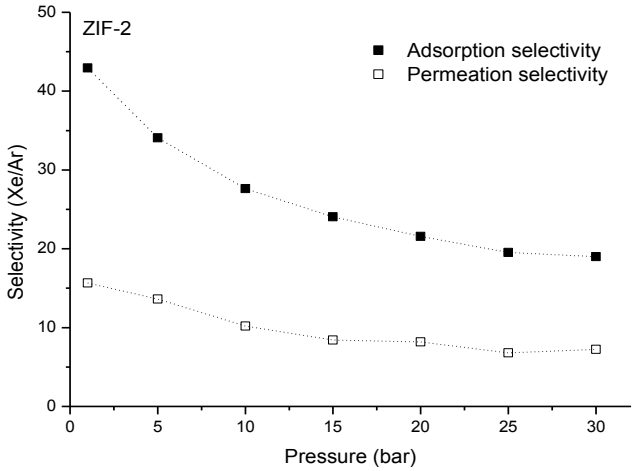
ZIF-2
Adsorption selectivity
Permeation selectivity
Selectivity (Xe/Ar)
Pressure (bar)
0
10
20
30
40
50
0
5
10
15
20
25
30

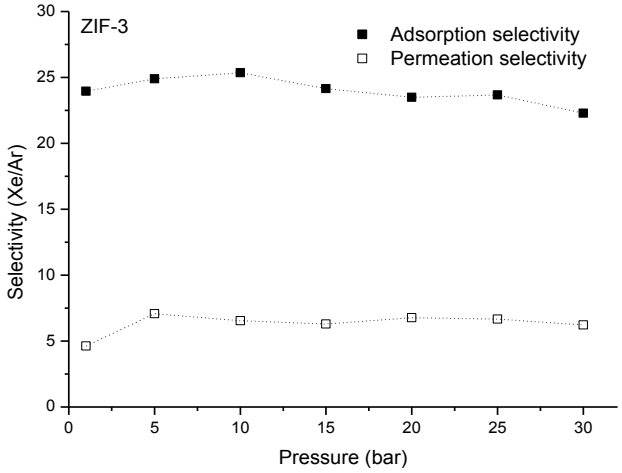
ZIF-3
Adsorption selectivity
Permeation selectivity
Selectivity (Xe/Ar)
Pressure (bar)
0
5
10
15
20
25
30
0
5
10
15
20
25
30

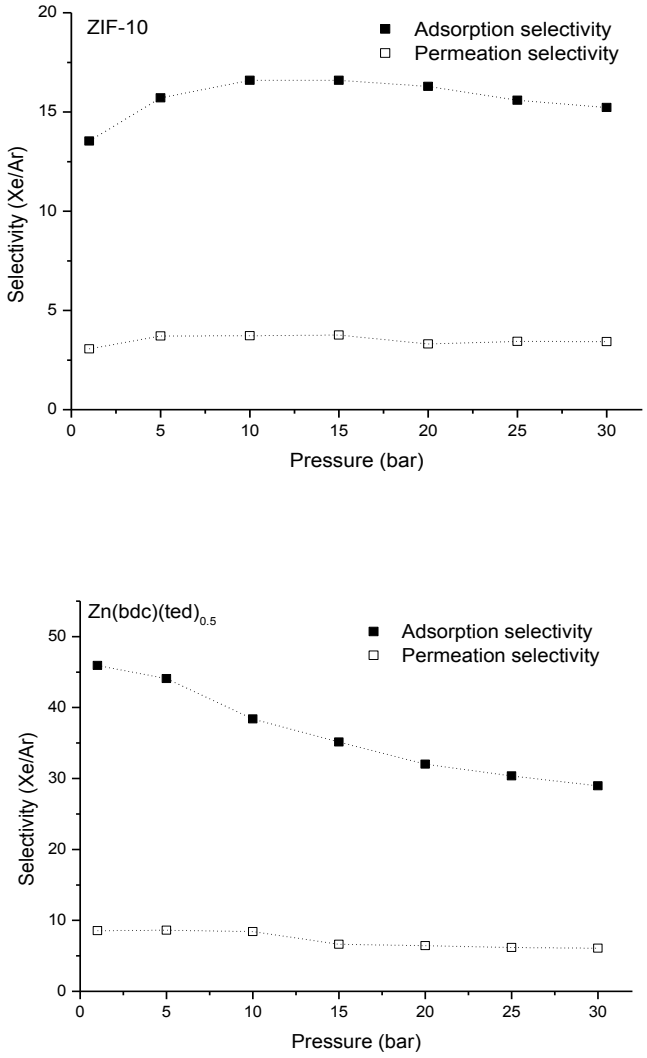

Figure A.6: Adsorption and permeation selectivity of MOFs for Xe/Ar mixtures at room temperature. The composition of the bulk gas mixture is 20/80.

B: Predicting Noble Gas Separation Performance of Metal Organic Frameworks Using Theoretical Correlations

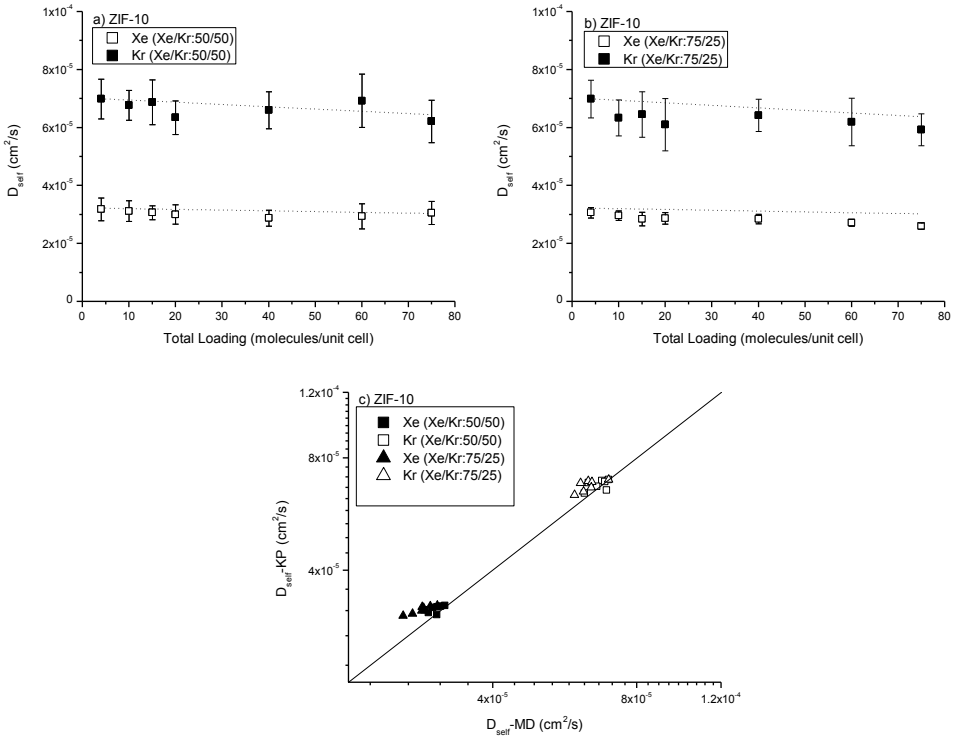

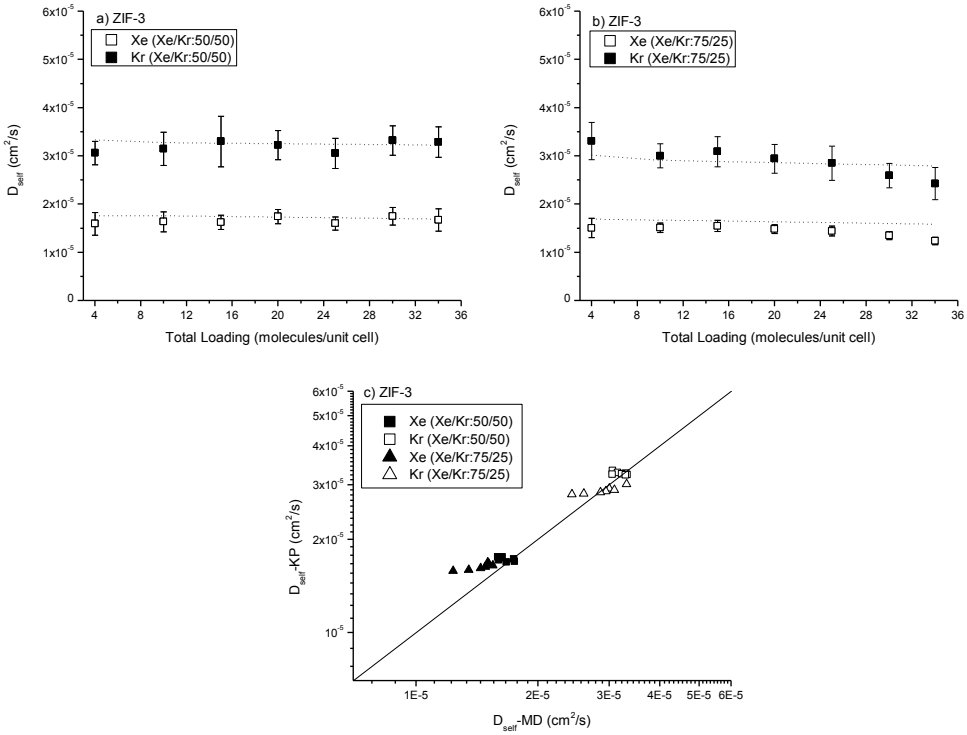
a) ZIF-3
Xe (Xe/Kr:50/50)
Kr (Xe/Kr:50/50)
D_self (cm^2/s)
Total Loading (molecules/unit cell)
b) ZIF-3
Xe (Xe/Kr:75/25)
Kr (Xe/Kr:75/25)
D_self (cm^2/s)
Total Loading (molecules/unit cell)
c) ZIF-3
Xe (Xe/Kr:50/50)
Kr (Xe/Kr:50/50)
Xe (Xe/Kr:75/25)
Kr (Xe/Kr:75/25)
D_self-KP (cm^2/s)
D_self-MD (cm^2/s)

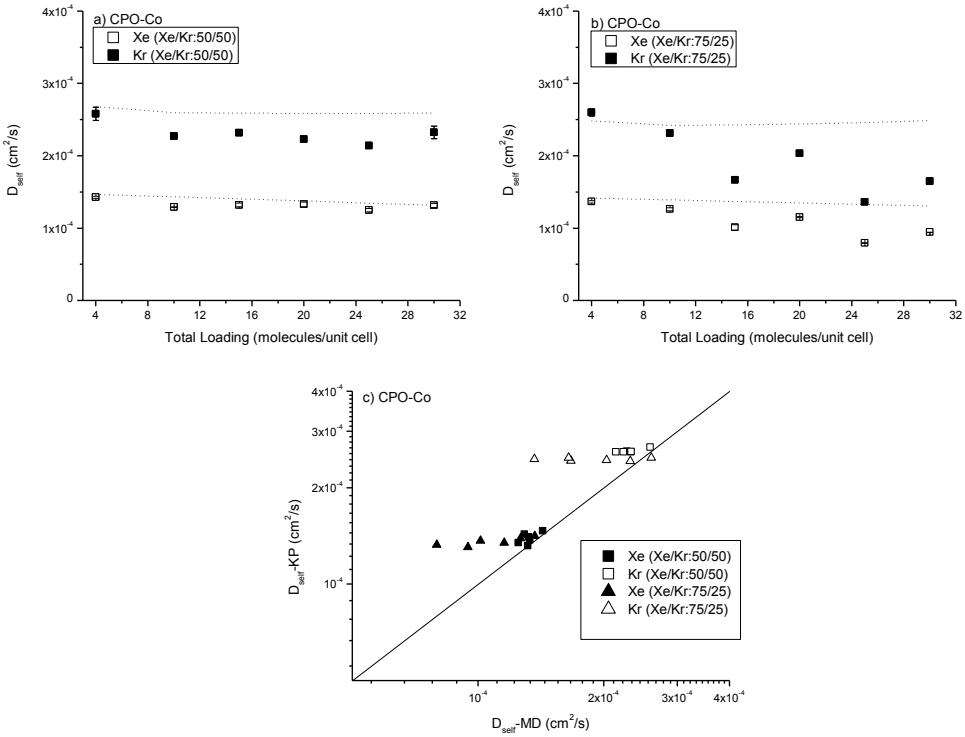
a) CPO-Co
Xe (Xe/Kr:50/50)
Kr (Xe/Kr:50/50)
D_{self} (cm^2/s)
Total Loading (molecules/unit cell)
b) CPO-Co
Xe (Xe/Kr:75/25)
Kr (Xe/Kr:75/25)
D_{self} (cm^2/s)
Total Loading (molecules/unit cell)
c) CPO-Co
D_{self}-KP (cm^2/s)
D_{self}-MD (cm^2/s)
Xe (Xe/Kr:50/50)
Kr (Xe/Kr:50/50)
Xe (Xe/Kr:75/25)
Kr (Xe/Kr:75/25)

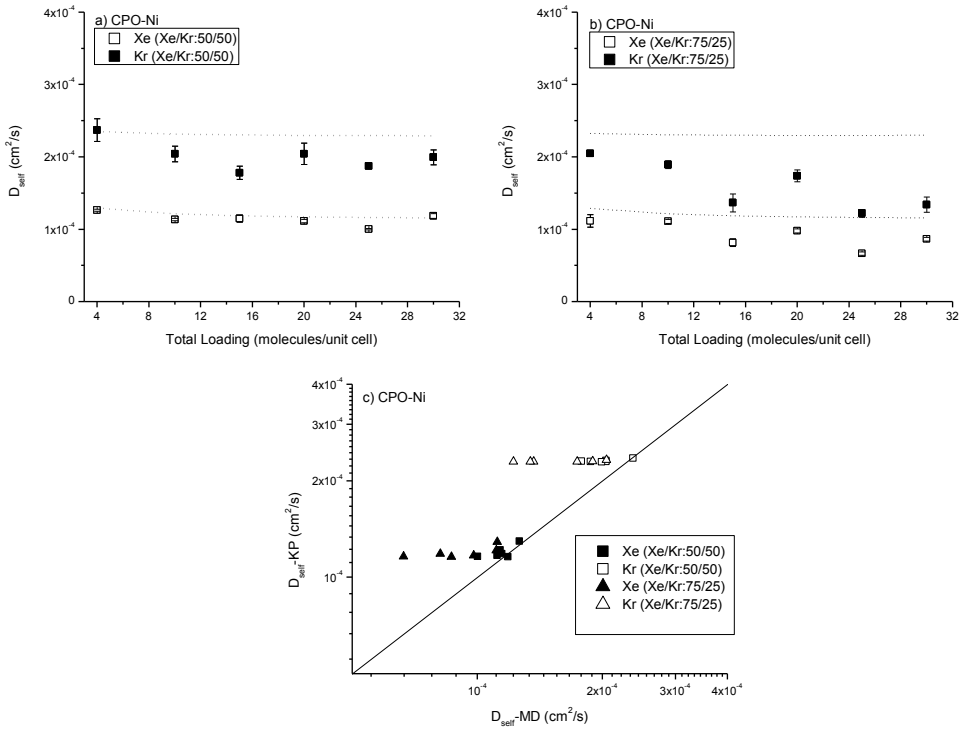
a) CPO-Ni
Xe (Xe/Kr:50/50)
Kr (Xe/Kr:50/50)
D_{self} (cm^2/s)
Total Loading (molecules/unit cell)
b) CPO-Ni
Xe (Xe/Kr:75/25)
Kr (Xe/Kr:75/25)
D_{self} (cm^2/s)
Total Loading (molecules/unit cell)
c) CPO-Ni
D_{self}-KP (cm^2/s)
D_{self}-MD (cm^2/s)
Xe (Xe/Kr:50/50)
Kr (Xe/Kr:50/50)
Xe (Xe/Kr:75/25)
Kr (Xe/Kr:75/25)

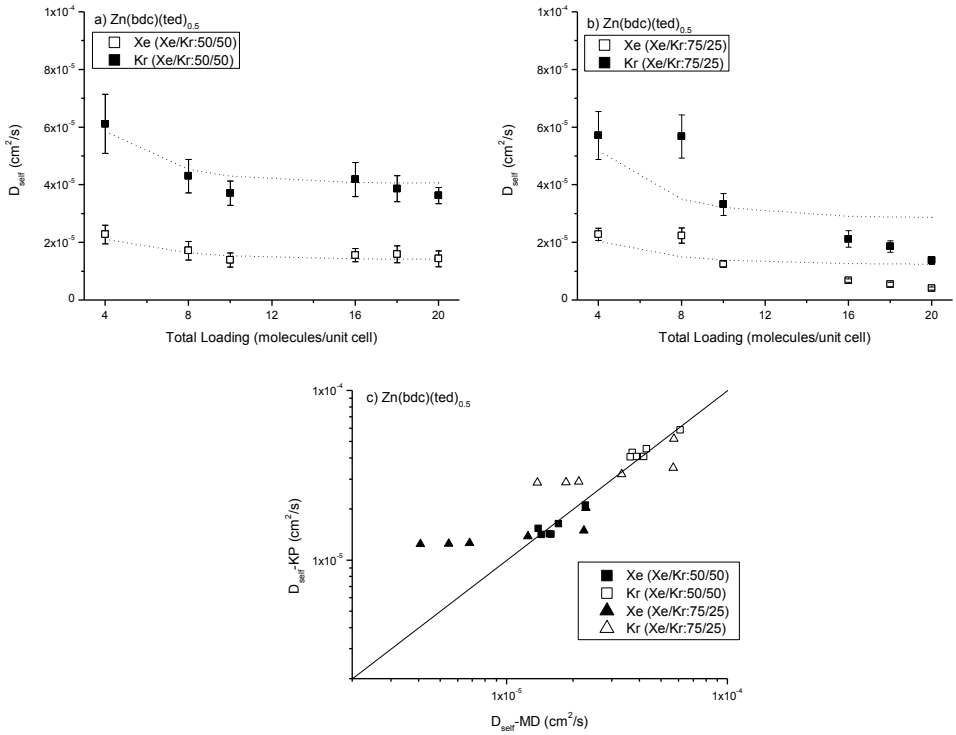

Figure B.1: The predictions of KP correlation (dotted lines) and the results of mixture MD simulations (symbols) for self-diffusion coefficients of a)Xe/Kr:50/50 b)Xe/Kr:75/25 mixtures. c)Comparison of theory and simulations for mixture self-diffusivities at all loadings and compositions.

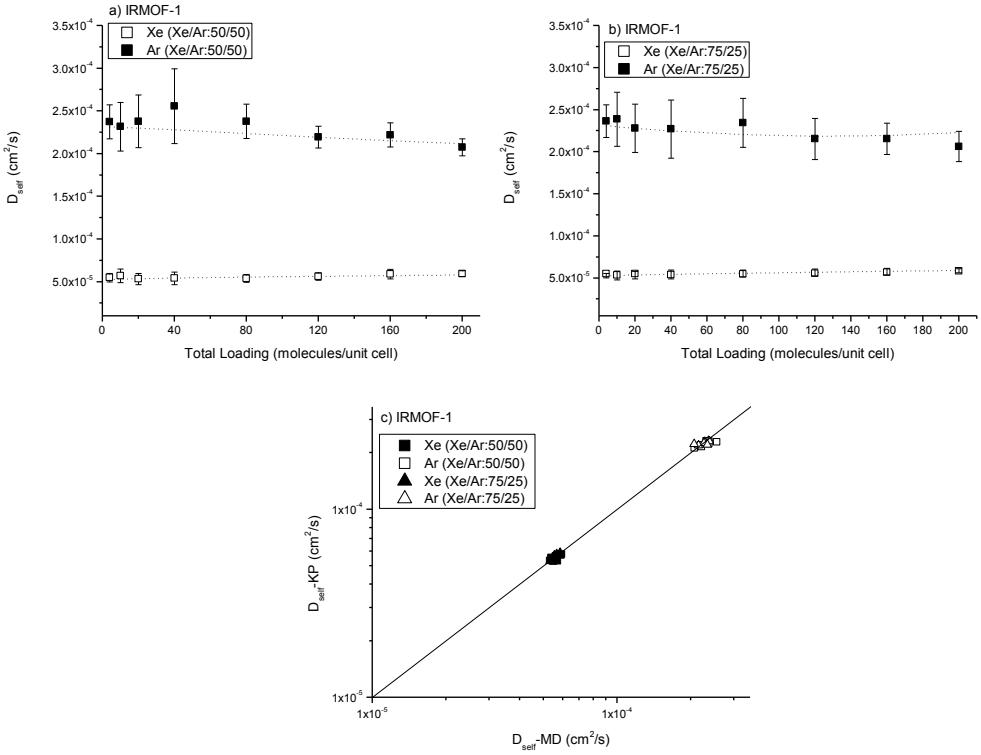
a) IRMOF-1
Xe (Xe/Ar:50/50)
Ar (Xe/Ar:50/50)
D_self (cm^2/s)
Total Loading (molecules/unit cell)
b) IRMOF-1
Xe (Xe/Ar:75/25)
Ar (Xe/Ar:75/25)
D_self (cm^2/s)
Total Loading (molecules/unit cell)
c) IRMOF-1
Xe (Xe/Ar:50/50)
Ar (Xe/Ar:50/50)
Xe (Xe/Ar:75/25)
Ar (Xe/Ar:75/25)
D_self-KP (cm^2/s)
D_self-MD (cm^2/s)

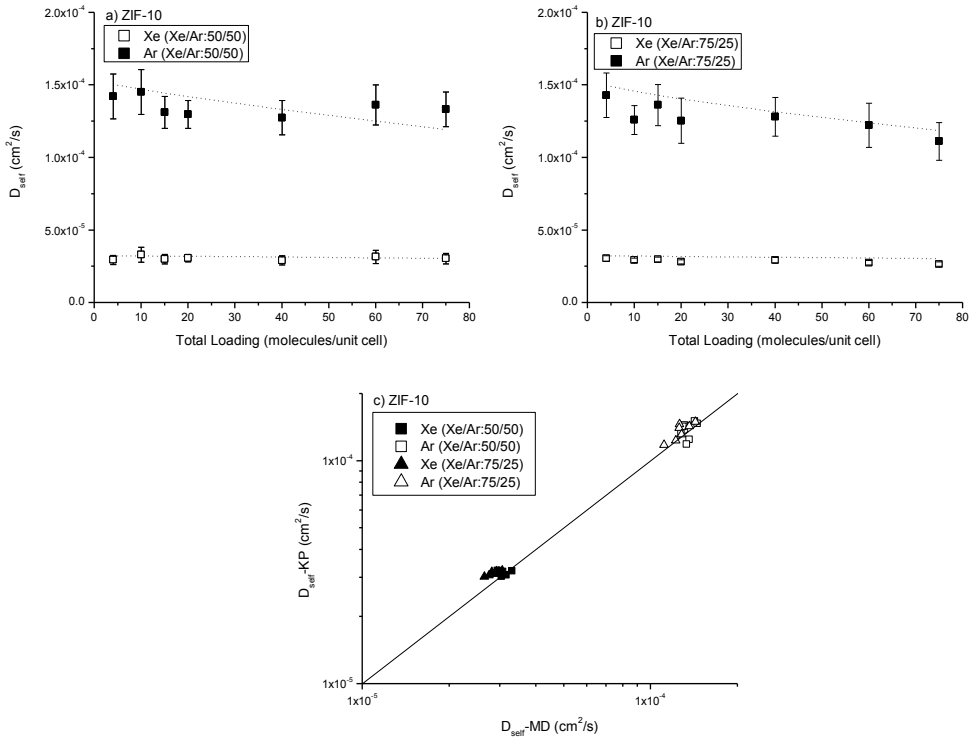
a) ZIF-10
Xe (Xe/Ar:50/50)
Ar (Xe/Ar:50/50)
D_{self} (cm^2/s)
Total Loading (molecules/unit cell)
b) ZIF-10
Xe (Xe/Ar:75/25)
Ar (Xe/Ar:75/25)
D_{self} (cm^2/s)
Total Loading (molecules/unit cell)
c) ZIF-10
Xe (Xe/Ar:50/50)
Ar (Xe/Ar:50/50)
Xe (Xe/Ar:75/25)
Ar (Xe/Ar:75/25)
D_{self}-KP (cm^2/s)
D_{self}-MD (cm^2/s)

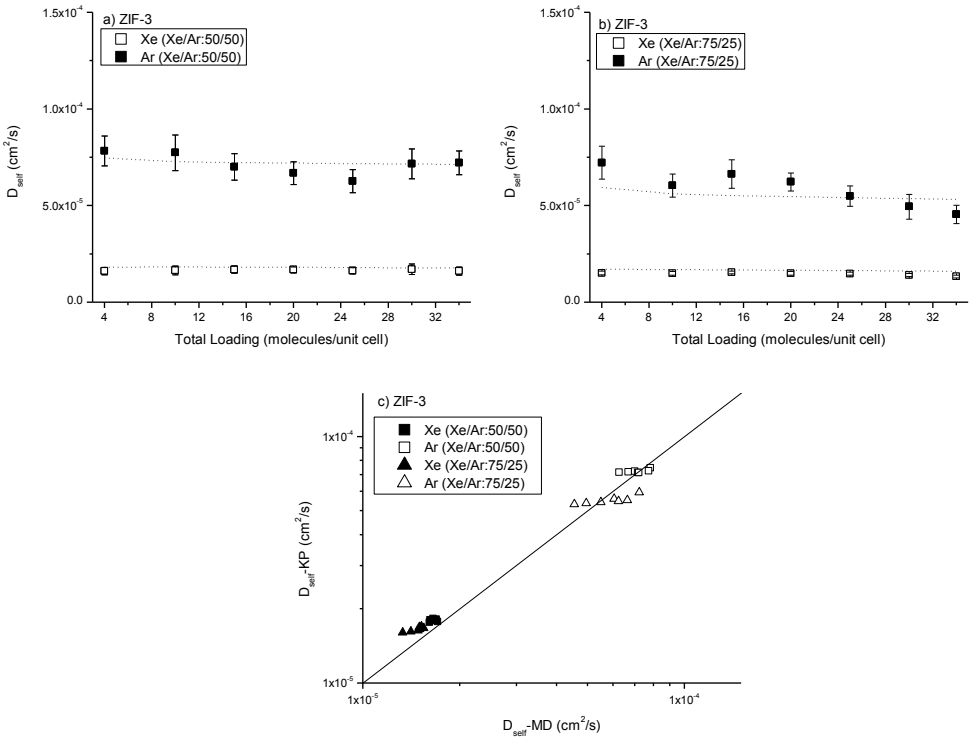
a) ZIF-3
Xe (Xe/Ar:50/50)
Ar (Xe/Ar:50/50)
D_self (cm^2/s)
Total Loading (molecules/unit cell)
b) ZIF-3
Xe (Xe/Ar:75/25)
Ar (Xe/Ar:75/25)
D_self (cm^2/s)
Total Loading (molecules/unit cell)
c) ZIF-3
Xe (Xe/Ar:50/50)
Ar (Xe/Ar:50/50)
Xe (Xe/Ar:75/25)
Ar (Xe/Ar:75/25)
D_self-KP (cm^2/s)
D_self-MD (cm^2/s)

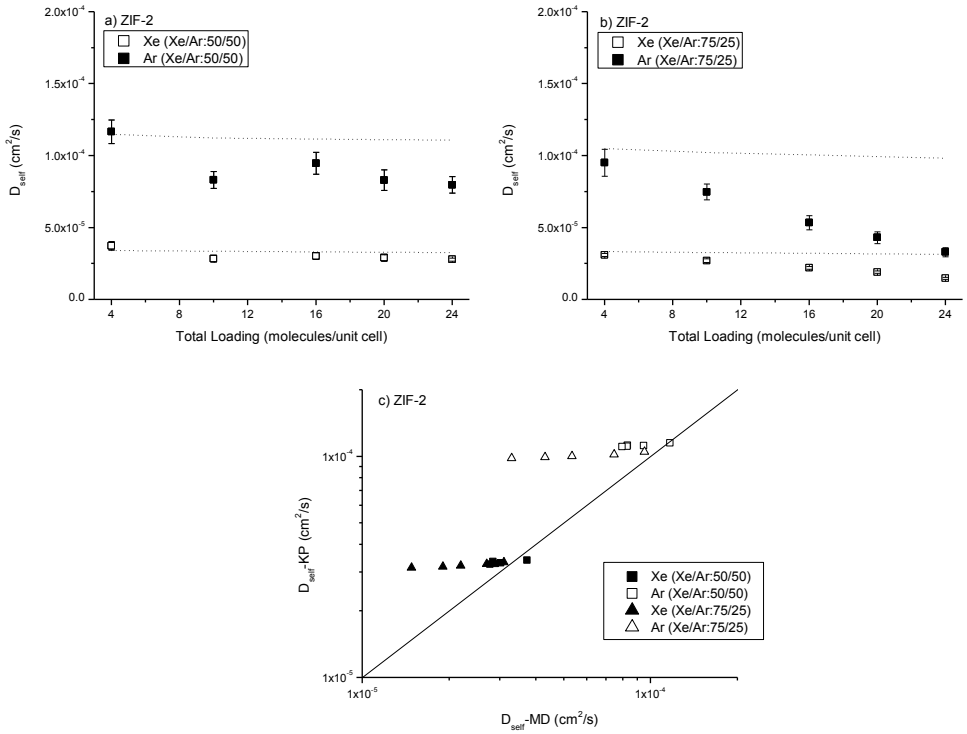
a) ZIF-2
Xe (Xe/Ar:50/50)
Ar (Xe/Ar:50/50)
D_{self} (cm^2/s)
Total Loading (molecules/unit cell)
b) ZIF-2
Xe (Xe/Ar:75/25)
Ar (Xe/Ar:75/25)
D_{self} (cm^2/s)
Total Loading (molecules/unit cell)
c) ZIF-2
Xe (Xe/Ar:50/50)
Ar (Xe/Ar:50/50)
Xe (Xe/Ar:75/25)
Ar (Xe/Ar:75/25)
D_{self}-KP (cm^2/s)
D_{self}-MD (cm^2/s)

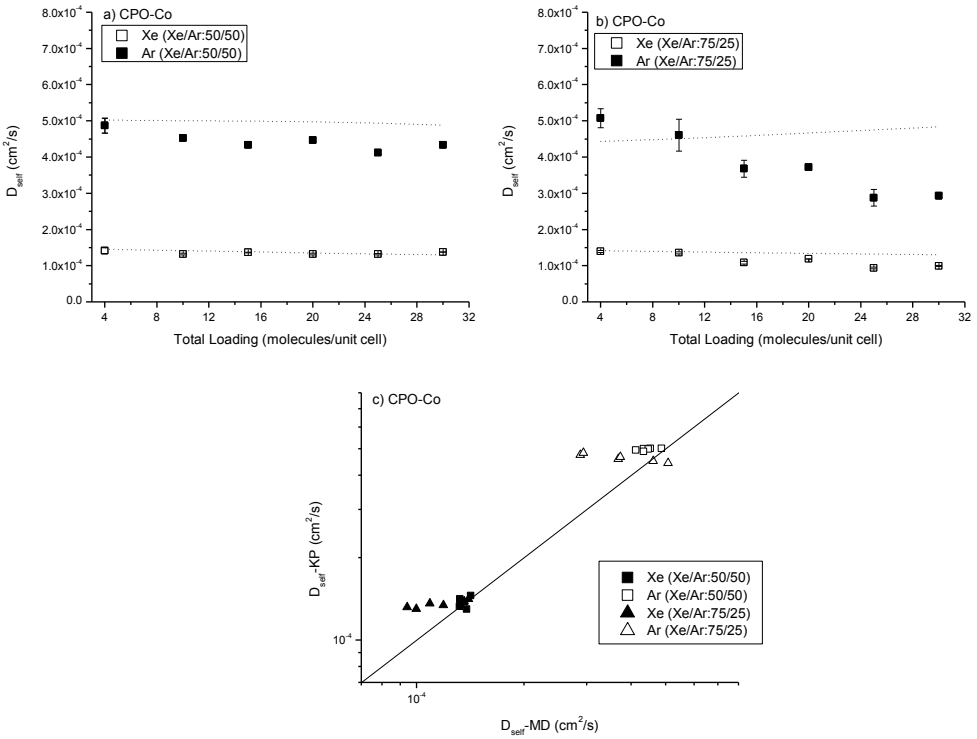
a) CPO-Co
Xe (Xe/Ar:50/50)
Ar (Xe/Ar:50/50)
D_self (cm^2/s)
Total Loading (molecules/unit cell)
b) CPO-Co
Xe (Xe/Ar:75/25)
Ar (Xe/Ar:75/25)
D_self (cm^2/s)
Total Loading (molecules/unit cell)
c) CPO-Co
Xe (Xe/Ar:50/50)
Ar (Xe/Ar:50/50)
Xe (Xe/Ar:75/25)
Ar (Xe/Ar:75/25)
D_self-KP (cm^2/s)
D_self-MD (cm^2/s)

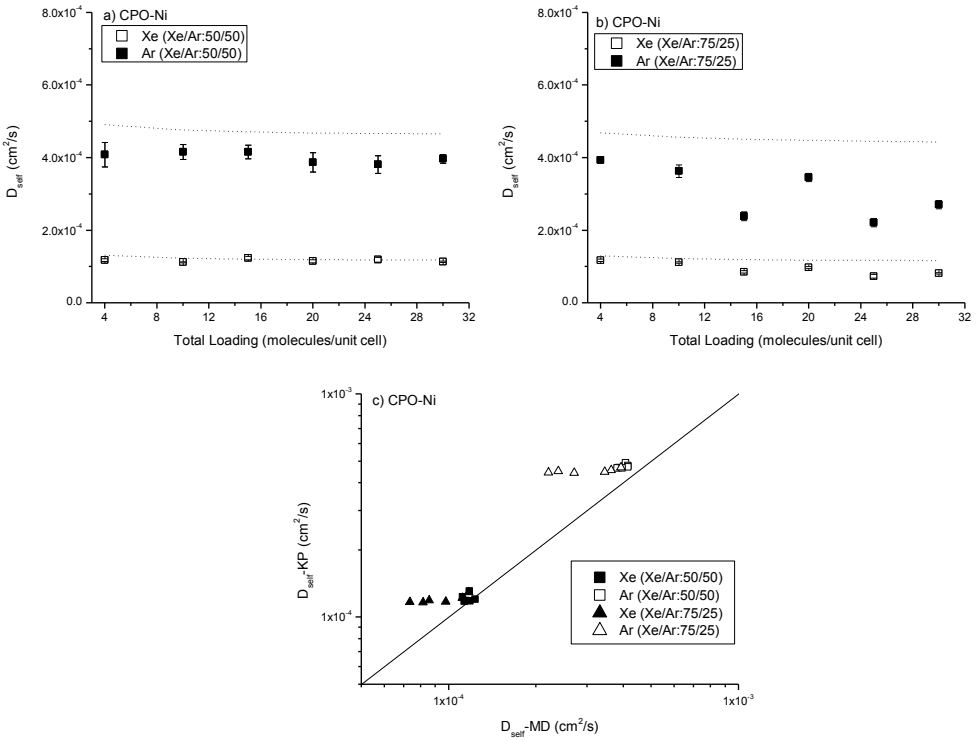
a) CPO-Ni
Xe (Xe/Ar:50/50)
Ar (Xe/Ar:50/50)
D_self (cm^2/s)
Total Loading (molecules/unit cell)
b) CPO-Ni
Xe (Xe/Ar:75/25)
Ar (Xe/Ar:75/25)
D_self (cm^2/s)
Total Loading (molecules/unit cell)
c) CPO-Ni
Xe (Xe/Ar:50/50)
Ar (Xe/Ar:50/50)
Xe (Xe/Ar:75/25)
Ar (Xe/Ar:75/25)
D_self-KP (cm^2/s)
D_self-MD (cm^2/s)

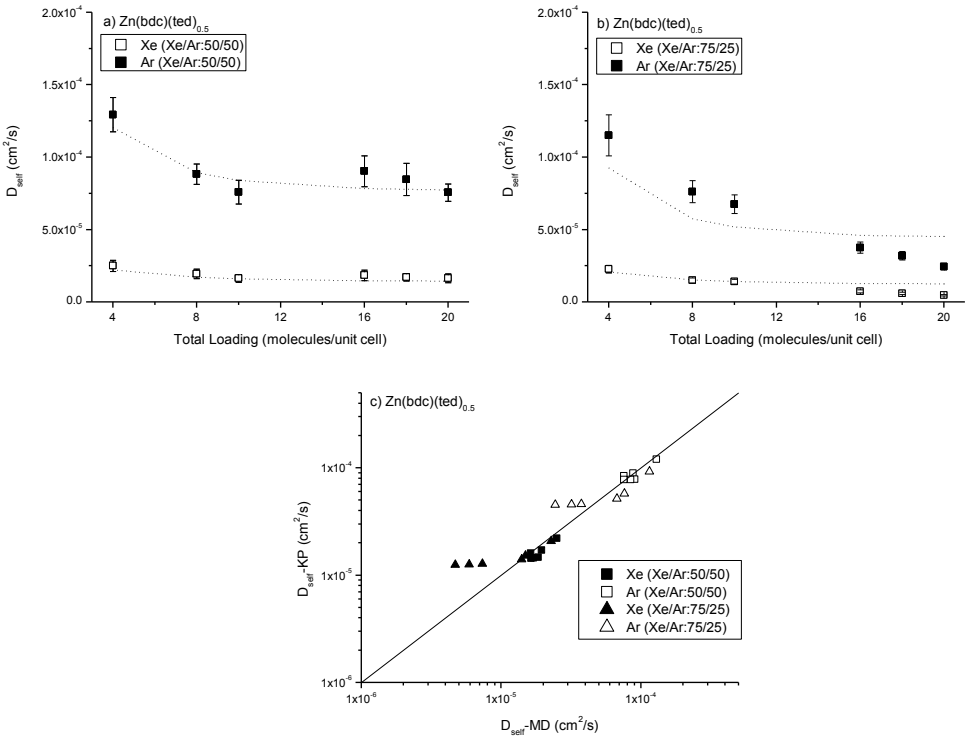
a) Zn(bdc)(ted)0.5
Xe (Xe/Ar:50/50)
Ar (Xe/Ar:50/50)
Dself (cm2/s)
Total Loading (molecules/unit cell)
b) Zn(bdc)(ted)0.5
Xe (Xe/Ar:75/25)
Ar (Xe/Ar:75/25)
Dself (cm2/s)
Total Loading (molecules/unit cell)
c) Zn(bdc)(ted)0.5
Dself-KP (cm2/s)
Dself-MD (cm2/s)
Xe (Xe/Ar:50/50)
Ar (Xe/Ar:50/50)
Xe (Xe/Ar:75/25)
Ar (Xe/Ar:75/25)

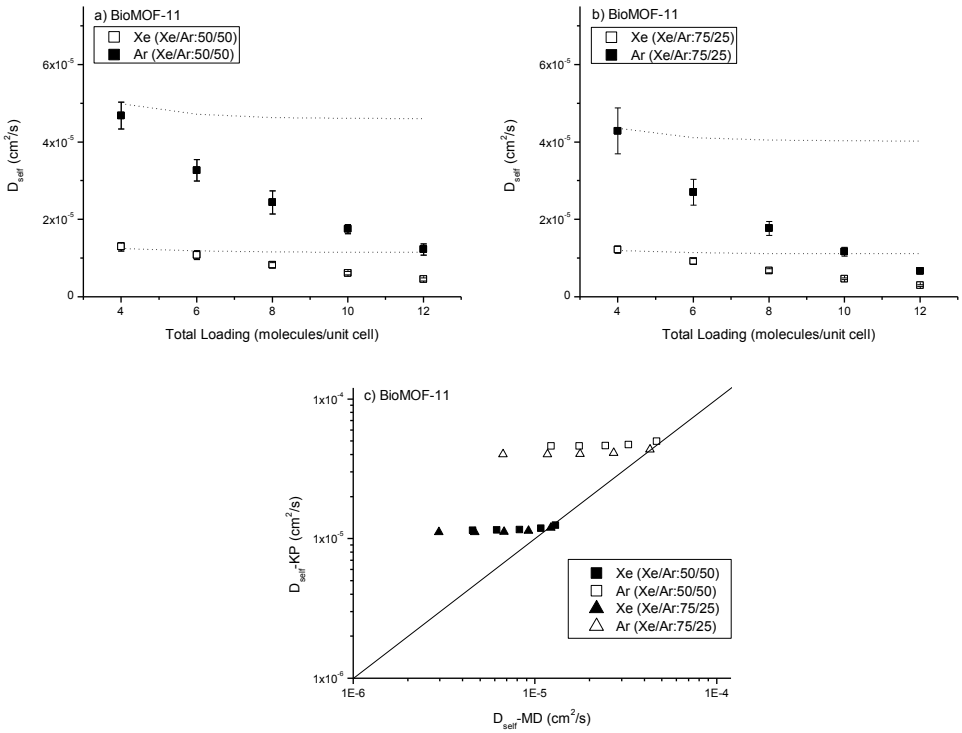
a) BioMOF-11
Xe (Xe/Ar:50/50)
Ar (Xe/Ar:50/50)
D_self (cm^2/s)
Total Loading (molecules/unit cell)
b) BioMOF-11
Xe (Xe/Ar:75/25)
Ar (Xe/Ar:75/25)
D_self (cm^2/s)
Total Loading (molecules/unit cell)
c) BioMOF-11
Xe (Xe/Ar:50/50)
Ar (Xe/Ar:50/50)
Xe (Xe/Ar:75/25)
Ar (Xe/Ar:75/25)
D_self-KP (cm^2/s)
D_self-MD (cm^2/s)

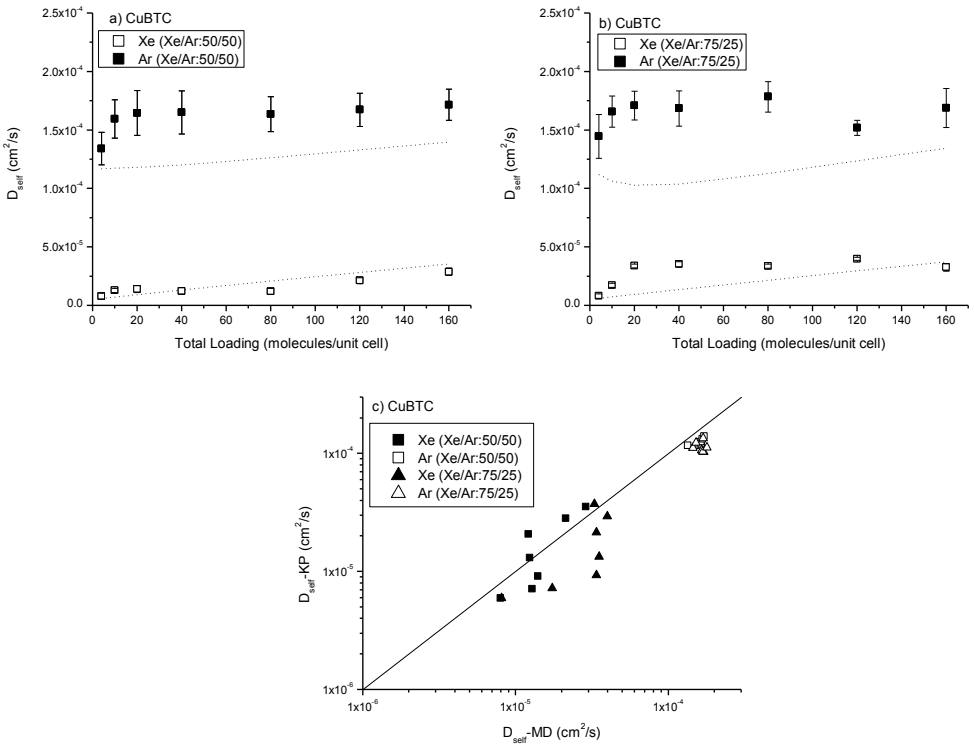

Figure B.2: The predictions of KP correlation (dotted lines) and the results of mixture MD simulations (symbols) for self-diffusion coefficients of a)Xe/Ar:50/50 b)Xe/Ar:75/25 mixtures. c)Comparison of theory and simulations for mixture self-diffusivities at all loadings and compositions.

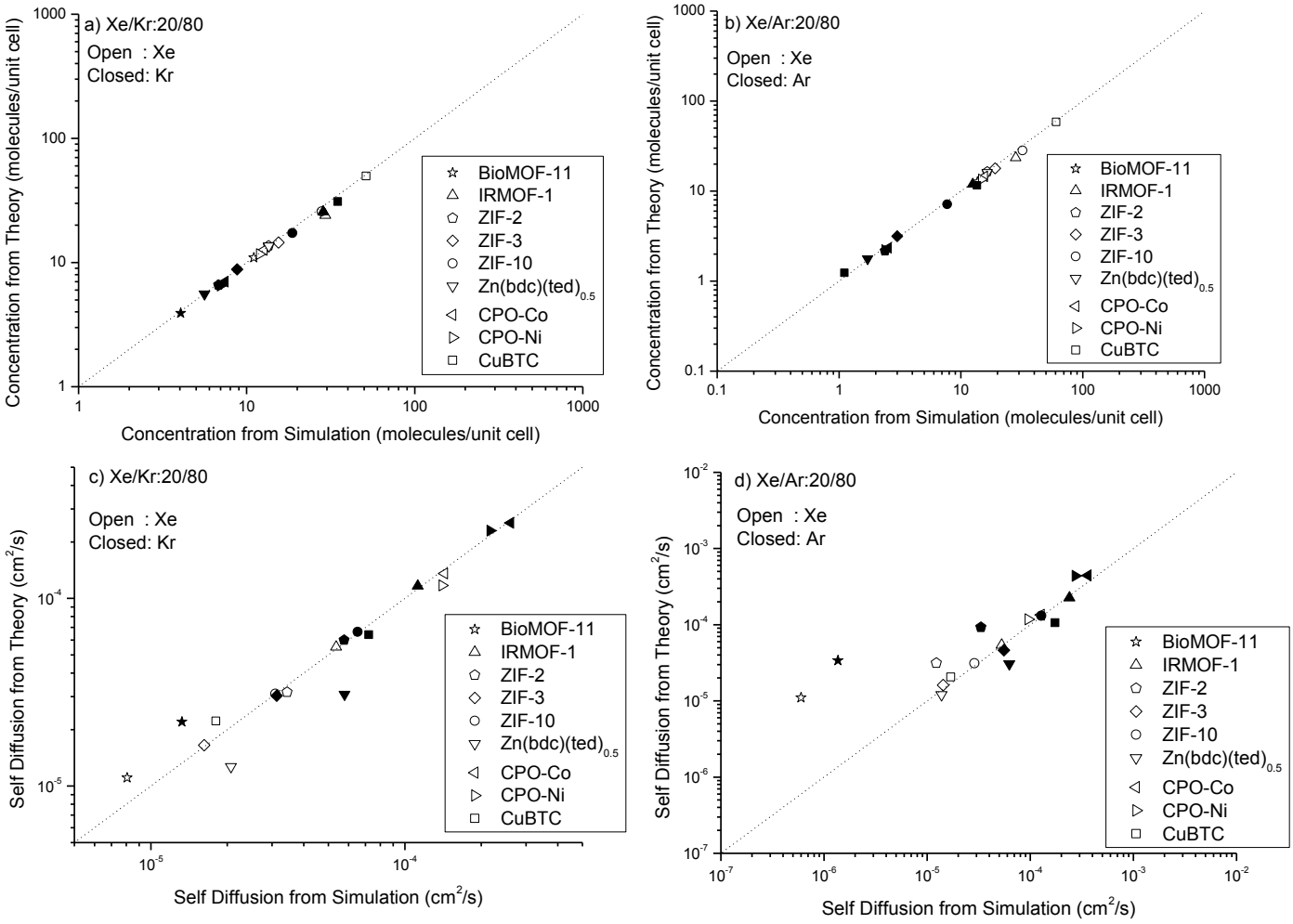

Figure B.3: Comparison of adsorbed compositions obtained from IAST and mixture GCMC simulations for a)Xe/Kr and b)Xe/Ar. Comparison of self-diffusivities obtained from KP and mixture MD simulations for c)Xe/Kr and d)Xe/Ar. All data is computed at 10 bar and 298 K.

Table B.1: Selectivities and permeabilities of MOFs calculated from theory and simulation for Xe/Kr mixture. The bulk composition of the mixture is 20/80 at 10 bar and 298 K.

Materials	Calculated property	Theory	Simulation	Saturation loading of pure Xe (molecules/unit cell)	Saturation loading of pure Kr (molecules/unit cell)	Total adsorbed loading (molecules/unit cell)	Xe in adsorbed phase (%)
BioMOF-11	Adsorption selectivity	11.167	10.898	15.86	19.20	15.09	73.15
	Diffusion selectivity	0.503	0.608				
	Permeation Selectivity	5.616	6.629				
	Permeability (/10^2 Barrer)	296.450	218.384				
IRMOF-1	Adsorption selectivity	3.749	4.117	140.50	165.64	58.00	50.72
	Diffusion selectivity	0.472	0.478				
	Permeation Selectivity	1.771	1.966				
	Permeability (/10^2 Barrer)	1553.305	1851.994				
ZIF-2	Adsorption selectivity	8.270	7.928	25.30	28.60	20.33	66.47
	Diffusion selectivity	0.526	0.596				
	Permeation Selectivity	4.354	4.726				
	Permeability (/10^2 Barrer)	1229.150	1326.213				
ZIF-3	Adsorption selectivity	6.591	7.050	31.45	37.10	24.25	63.80
	Diffusion selectivity	0.545	0.518				
	Permeation Selectivity	3.592	3.650				
	Permeability (/10^2 Barrer)	670.518	700.048				
ZIF-10	Adsorption selectivity	5.979	5.991	72.54	103.04	46.66	59.97
	Diffusion selectivity	0.467	0.474				
	Permeation Selectivity	2.793	2.841				
	Permeability (/10^2 Barrer)	1015.281	1098.163				
$Zn(bdc)(ted)_{0.5}$	Adsorption selectivity	9.731	9.648	23.30	25.65	19.19	70.69
	Diffusion selectivity	0.412	0.357				
	Permeation Selectivity	4.009	3.443				
	Permeability (/10^2 Barrer)	654.976	1067.905				
CPO-Co	Adsorption selectivity	7.194	6.825	36.38	29.91	20.14	63.05
	Diffusion selectivity	0.538	0.549				
	Permeation Selectivity	3.873	3.744				
	Permeability (/10^2 Barrer)	5206.006	5518.177				
CPO-Ni	Adsorption selectivity	7.180	6.840	30.53	31.10	18.90	63.10
	Diffusion selectivity	0.510	0.647				
	Permeation Selectivity	3.661	4.425				
	Permeability (/10^2 Barrer)	4271.031	5210.283				
CuBTC	Adsorption selectivity	6.418	5.907	168.74	223.61	86.29	59.62
	Diffusion selectivity	0.347	0.250				
	Permeation Selectivity	2.228	1.477				
	Permeability (/10^2 Barrer)	1079.407	905.477				

Table B.2: Selectivities and permeabilities of MOFs calculated from theory and simulation for Xe/Ar mixture. The bulk composition of the mixture is 20/80 at 10 bar and 298 K.

Materials	Calculated property	Theory	Simulation	Saturation loading of pure Ar (molecules/unit cell)	Total adsorbed loading (molecules/unit cell)	Xe in adsorbed phase (%)
BioMOF-11	Adsorption selectivity	41.266	49.518	22.35	14.81	95.54
	Diffusion selectivity	0.324	0.438			
	Permeation Selectivity	13.372	21.690			
	Permeability (/10^2 Barrer)	343.140	20.136			
IRMOF-1	Adsorption selectivity	7.878	9.005	288.19	40.78	69.24
	Diffusion selectivity	0.241	0.221			
	Permeation Selectivity	1.897	1.991			
	Permeability (/10^2 Barrer)	1498.010	1752.096			
ZIF-2	Adsorption selectivity	30.232	27.632	31.33	18.88	87.36
	Diffusion selectivity	0.341	0.369			
	Permeation Selectivity	10.310	10.194			
	Permeability (/10^2 Barrer)	1472.662	577.780			
ZIF-3	Adsorption selectivity	22.727	25.360	48.59	22.08	86.38
	Diffusion selectivity	0.348	0.258			
	Permeation Selectivity	7.913	6.543			
	Permeability (/10^2 Barrer)	805.743	763.061			
ZIF-10	Adsorption selectivity	15.875	16.594	124.14	39.79	80.58
	Diffusion selectivity	0.238	0.224			
	Permeation Selectivity	3.772	3.719			
	Permeability (/10^2 Barrer)	1117.967	1166.783			
$Zn(bdc)(ted)_{0.5}$	Adsorption selectivity	36.201	38.377	29.44	18.21	90.56
	Diffusion selectivity	0.394	0.220			
	Permeation Selectivity	14.262	8.425			
	Permeability (/10^2 Barrer)	733.186	864.926			
CPO-Co	Adsorption selectivity	24.807	24.634	32.47	18.19	86.03
	Diffusion selectivity	0.304	0.351			
	Permeation Selectivity	7.539	8.645			
	Permeability (/10^2 Barrer)	5934.461	6041.490			
CPO-Ni	Adsorption selectivity	24.468	24.898	34.04	17.16	86.16
	Diffusion selectivity	0.269	0.350			
	Permeation Selectivity	6.585	8.722			
	Permeability (/10^2 Barrer)	4963.519	4402.581			
CuBTC	Adsorption selectivity	20.220	17.880	235.31	74.23	81.72
	Diffusion selectivity	0.193	0.097			
	Permeation Selectivity	3.903	1.740			
	Permeability (/10^2 Barrer)	1175.434	1003.075			